1 2 90

UNIVERSIDADE D
COIMBRA

Inês Milheiro da Conceição

MODEL OF AN ULTRASOUND-BASED SYSTEM FOR CATARACT DETECTION AND CLASSIFICATION

Dissertation in the context of the Master in Biomedical Engineering, specialization in Biomedical Instrumentation, supervised by Prof. Dr. Mário João Simões Ferreira dos Santos and Prof. Dr. Lorena Itatí Petrella and presented to the University of Coimbra.

September 2022

Faculdade de Ciências e Tecnologia da Universidade de Coimbra

Model of an Ultrasound-Based System for Cataract Detection and Classification

Inês Milheiro da Conceição

Dissertation in the context of the Master in Biomedical Engineering, specialization in Biomedical Instrumentation, supervised by Prof. Dr. Mário João Simões Ferreira dos Santos and Prof. Dr. Lorena Itatí Petrella and presented to the University of Coimbra.

September 2022

Acknowledgments

Em primeiro lugar, quero agradecer aos meus orientadores, Professor Mário Santos e Professora Lorena Petrella que me receberam no seu grupo de trabalho e me acompanharam ao longo deste ano desafiante, mostrando-se sempre disponíveis para me esclarecer e orientar na direção certa. Obrigada por todo o apoio e ajuda no desenvolvimento deste projeto.

Agradeço ao Instituto de Telecomunicações, Pólo de Coimbra, pela oportunidade de integrar o projeto CATARACTUS e receber uma Bolsa de Iniciação à Investigação Científica.

Um agradecimento especial ao Professor Fernando Perdigão pelo tempo que disponibilizou para me ajudar a desenvolver uma parte importante do projeto, transmitindo-me conhecimentos importantes de processamento de sinal e facilitando o acesso aos recursos computacionais do IT, fundamentais para o cumprimento de todos os objetivos do projeto.

Por fim, agradeço à minha família e amigos, especialmente aos meus pais, irmão e avós, por toda a paciência e apoio incondicional. Obrigada por acreditarem nas minhas capacidades e me transmitirem a confiança e motivação necessária para superar esta etapa.

Abstract

Cataract is an eye lens opacity that affects its transparency, leading to vision deterioration. Currently, cataract surgery is the only treatment and phacoemulsification is the most used technique to extract the cataract. This surgical procedure uses energy to disintegrate the lens into small pieces that are afterward removed and replaced by an artificial intraocular lens. The hardness of the cataract determines the optimal energy for the phacoemulsification procedure, and excessive levels of energy may lead to surgical complications.

An experimental Eye Scan Ultrasound System (ESUS) is composed of an ophthalmologic probe, a module responsible for probe excitation and signal acquisition, and a computer, and it was developed for automatic cataract characterization, to provide information regarding cataracts type, severity, and hardness, and to estimate the optimal phacoemulsification energy. The objective of this work is to model an ultrasound-based system for cataract detection and classification, following the ESUS configuration. The model includes electric-to-acoustic signal conversion that occurs in the ultrasonic probe, propagation of the ultrasonic waves through the eye, and the acoustic-to-electric signal conversion again in the probe. For modeling the propagation of ultrasonic waves, the k-Wave MATLAB toolbox was used. To model the electric-to-acoustic and acoustic-to-electric conversions, several approaches for estimating the impulse response of the probe were considered: gamma-tone model, electric-to-acoustic transfer function modeling and an optimization technique.

The study of the acoustic propagation of ultrasonic waves inside the eye was carried out through simulations. Simulated signals obtained for 2D and 3D media were compared, revealing that 3D simulations are more appropriate for a good approximation to real signals. It was also depicted that using a spatial resolution of 8 μm represents a good compromise between computational resources and the resolution needed for representing the microstructures associated with the cataract. The presence of cataract-mimicking microstructures was well evidenced in the simulated signals. The impulse response that characterizes the probe was successfully estimated. Concluding, the result of simulations agrees well with real signals acquired with the ESUS.

Keywords: Cataract, Ultrasound, ESUS, Simulation, k-Wave

Resumo

A catarata é uma opacidade no cristalino do olho que afeta a sua transparência, provocando deterioração da visão. Atualmente, a cirurgia à catarata é o único tratamento e a facoemulsificação é a técnica mais usada para extração de catarata. Este procedimento cirúrgico utiliza energia para desintegrar a lente em pequenos pedaços que são removidos de seguida e substituídos por uma lente intraocular artificial. A dureza da catarata determina a energia ótima para o procedimento de facoemulsificação, e níveis de energia excessivos originam complicações cirúrgicas.

O sistema experimental Eye Scan Ultrasound System (ESUS) é composto por uma sonda oftalmológica, um módulo responsável pela excitação da sonda e aquisição de sinal e um computador, e foi desenvolvido para a caracterização automática da catarata, fornecendo informações relativas ao tipo, severidade e dureza da catarata, e para estimar a energia ótima de facoemulsificação. O objetivo deste trabalho é modelar um sistema baseado em ultrassons para deteção e classificação de catarata, seguindo a configuração do ESUS. O modelo inclui a conversão do sinal elétrico para acústico na sonda de ultrassons, a propagação das ondas ultrassonoras no olho e a conversão do sinal acústico para elétrico novamente na sonda. Para modelar a propagação de ondas ultrassonoras, a toolbox k-Wave do MATLAB foi utilizada. Para modelar as conversões elétrico/acústico e acústico/elétrico, foram consideradas várias abordagens para estimar a resposta impulsional da sonda: modelo gamma-tone, modelo da função transferência elétrico/acústico e uma técnica de otimização.

O estudo da propagação acústica de ondas ultrassonoras dentro do olho foi realizado por meio de simulações. Sinais simulados em meios 2D e 3D foram comparados, revelando que simulações 3D são mais apropriadas para uma boa aproximação aos sinais reais. Foi ainda descrito que o uso de uma resolução espacial de 8 µm representa um bom compromisso entre os recursos computacionais e a resolução necessária para representar as microestruturas associadas à catarata. A presença de microestruturas que imitam a catarata foi evidenciada nos sinais simulados. A resposta impulsional que caracteriza a sonda foi estimada com sucesso. Concluindo, o resultado das simulações está em boa concordância com os sinais reais adquiridos com o ESUS.

Palavras-chave: Catarata, Ultrassom, ESUS, Simulação, k-Wave

Contents

Acknowledgments iv
Abstract v
Resumo vi
Contents vii
List of Figures ix
List of Tables xiii
List of Acronyms xiv
List of Symbols xv
1. Introduction 1
  1.1. Motivation 1
  1.2. Objectives 2
  1.3. Thesis Organization 2
2. Background Concepts 4
  2.1. Crystalline Lens and Cataract 4
    2.1.1. Crystalline Lens 4
    2.1.2. Cataract 5
    2.1.3. LOCS III Cataract Classification System 6
    2.1.4. Phacoemulsification 7
  2.2. Ultrasounds 8
    2.2.1. Ultrasound Interaction with Matter 9
  2.3. Ultrasound Transducers 12
    2.3.1. Ultrasound Transducers Concepts 12
    2.3.2. Ultrasound for Diagnosis 14
3. State of the Art 15
  3.1. Cataract Evaluation Using Ultrasounds 15
  3.2. ESUS Acquisition System 17
  3.3. Simulation of Ultrasound Propagation Using k-Wave 19
  3.4. Ultrasonic Probe Modeling 21
    3.4.1. Model of an Experimental System as a LTI System 21
    3.4.2. Equivalent Circuit of a Piezoelectric Transducer 23
    3.4.3. Gamma-Tone Model 24
4. Ultrasonic Signals Simulation 26
  4.1. Simulation with the k-Wave Toolbox 26
  4.2. Preliminary Tests 28
    4.2.1. Minimum Height of the Eye Matrix 30

- 4.3. Resolution Analysis 34
- 4.4. 3D Eye Matrix 35
  - 4.4.1. Influence of the Curvature of the Probe and Interfaces 37
- 4.5. Simulation Step by Step 43
- 4.6. Improved Resolution 46
  - 4.6.1. Structures Inside the Lens 48
  - 4.6.2. Comparison with Real Signals 52
- 4.7. Simulation Results 53

5. Model of the Probe 55

- 5.1. Materials and Methods 55
  - 5.1.1. Experimental Setup 55
  - 5.1.2. Transfer Function Modeling 57
  - 5.1.3. Impulse Response by Optimization 58
- 5.2. Probe Focal Length and Central Frequency 59
- 5.3. Measurements 60
  - 5.3.1. Arbitrary Function Generator 60
  - 5.3.2. Pulser/Receiver 61
  - 5.3.3. ESUS 62
- 5.4. Modeling of the Probe 63
  - 5.4.1. Gamma-Tone Model 63
  - 5.4.2. Partial Transfer Function (*H*) Modeling 65
  - 5.4.3. Impulse Response Modeling with Pulser/Receiver Measurements 69
  - 5.4.4. Impulse Response Modeling with ESUS Measurements 71
- 5.5. Modeling of the Complete System 73
  - 5.5.1. Model with Pulser/Receiver Data 73
  - 5.5.2. Model with ESUS Data 74
- 5.6. Comparison Between Simulated and Real Signals 76

6. Conclusions and Future Work 79

Bibliography 80

Appendix A – Datasheet of the 20 MHz A-scan Probe 84

List of Figures

Figure 2.1: Anatomy of the eye………………………………………………………………….. 4

Figure 2.2: Anatomy of the crystalline lens…………………………………………………..… 5

Figure 2.3: Diagram representing the three types of cataracts………………………………….... 6

Figure 2.4: LOCS III Grading Standard……………………………………………………..... 7

Figure 2.5: Particle displacement in a longitudinal wave……………………………………… 9

Figure 2.6: Non-perpendicular incidence at a large and smooth interface……………………... 10

Figure 2.7: Representation of scattering……………………………………………………….. 11

Figure 2.8: Schematic representation of an ultrasound transducer…………………....……... 13

Figure 2.9: Representation of a planar transducer acoustic field and focused transducer acoustic field…………………………………………………………………………………... 13

Figure 2.10: A-scan of a normal eye………………………………………………………… 14

Figure 2.11: B-scan of a normal eye……………………………………………………........ 14

Figure 3.1: B-scan images for lenses without cataract, and with incipient, moderate, and severe cataract…………………………………………………………………………….… 16

Figure 3.2: A-scan signal obtained from a rat eye with induced nuclear cataract……………... 17

Figure 3.3: Components of the ESUS acquisition system…………………………………….. 17

Figure 3.4: 2D eye matrix used in the simulations……………………………………………... 19

Figure 3.5: Simulated signals of a healthy lens and cataractous lens………………………….. 20

Figure 3.6: 1D eye model used for the simulations……………………………………….…... 21

Figure 3.7: Representation of a LTI system with impulse response $h(t)$……………………… 22

Figure 3.8: Equivalent electric circuits of a spherical-shell transducer……………………….. 23

Figure 4.1: Excitation pulse used in the simulations…………………………………………..... 28

Figure 4.2: Simulated A-scan considering a healthy lens……………………………………..... 30

Figure 4.3: Eye grid with the minimum height based on the source/sensor profile delimited by two red lines…………………………………………………………………………….. 31

Figure 4.4: Calculation of the pulse duration…………………………………………………... 32

Figure 4.5: 2D eye matrix with a resolution of 12 µm………………………………………… 33

Figure 4.6: Simulated signal with constrained grid size……………………………………….. 34

Figure 4.7: Simulation signal obtained with the 2D eye matrix with a resolution of 24 µm…... 36

Figure 4.8: Simulated signal obtained with the 3D eye matrix with a resolution of 24 µm…… 36

Figure 4.9: Plane matrix with the probe profile, and plane anterior and posterior lens interfaces... ……………………………………………………………………..…................... 38

Figure 4.10: Simulation signal obtained with the 2D matrix with plane interfaces and source/ sensor……………………………………………………………………………............... 38
Figure 4.11: Simulation signal obtained with the 3D matrix with plane interfaces and source/ sensor……………………………………………………………………………............... 39
Figure 4.12: Matrix with the curve profile of the probe and plane anterior and posterior interfaces.. ………………………………………………………………………………………... 40
Figure 4.13: Simulation signal obtained with the 2D matrix with plane interfaces and curved source/sensor………………………………………………………………………. 40
Figure 4.14: Simulation signal obtained with the 3D matrix with plane interfaces and curved source/sensor………………………………………………………………………. 40
Figure 4.15: Matrix with anterior and posterior lens interfaces and the probe profile…………. 41
Figure 4.16: Simulation signal obtained with the 2D matrix with curved interfaces and source/ sensor…………………………………………………………………………………. 42
Figure 4.17: Simulation signal obtained with the 3D matrix with curved interfaces and source/ sensor…………………………………………………………………………………. 42
Figure 4.18: Matrix with source and sensor positioned on the probe and the anterior lens interface.. ………………………………………………………………………………………... 44
Figure 4.19: Reconstruction of the simulated signal resulting from the three phases of simulation…………………………………………………………………………….. 44
Figure 4.20: Matrix with source and sensor placed on the probe and the aqueous humor…….. 45
Figure 4.21: Reconstruction of the simulated signal resulting from the three stages of simulation where the simulation was interrupted in the aqueous humor.…………………………... 45
Figure 4.22: Central slide of the 3D eye matrix with a pixel size of 8 µm……………………... 47
Figure 4.23: Simulation signal obtained with the 3D eye matrix with a resolution of 8 µm…… 48
Figure 4.24: Eye matrix with a structure with an edge of 16 µm placed in the midpoint of the lens…………………………………………………………………………………… 48
Figure 4.25: 3D simulated signal using an eye matrix resolution of 8 µm, with a structure in the middle of the lens, with 2 voxels side……...…………………………………………….. 49
Figure 4.26: Eye matrix with a structure with a side of 80 µm placed in the middle of the lens… ……………………………………………………………………………………………50
Figure 4.27: 3D simulated signal with matrix a resolution of 8 µm, with a structure in the middle of the lens, with 10 voxels side…………………………………………………………. 50
Figure 4.28: Eye matrix with multiple structures with 16 µm side in the anterior region of the lens……………………………………………………………………………………51
Figure 4.29: 3D simulated signal with a matrix resolution of 8 µm, with several structures in the anterior part of the lens, each with 2 voxels side…….………………………………….. 52

Figure 4.30: Example of a real signal from a healthy eye acquired with ESUS……………….... 53
Figure 5.1: A-scan 20 MHz ophthalmologic probe………………………………………….. 56
Figure 5.2: Experimental setup……………………………………………………………… 56
Figure 5.3: Maximum peak-to-peak amplitude as a function of the distance between the probe and the reflector………………………………………………………………………. 59
Figure 5.4: Peak-to-peak amplitude as a function of frequency, considering an excitation burst with 10 V of amplitude and 1 and 2 cycles………………………………………………. 60
Figure 5.5: Excitation signal, and corresponding frequency spectrum………………………… 60
Figure 5.6: Echo signal received by the probe, and corresponding frequency spectrum……….. 61
Figure 5.7: Electric excitation signal from pulser/receiver output and the respective frequency spectrum……………………………………………………………………………… 61
Figure 5.8: Echo signal obtained with the pulser/receiver after propagation in the medium and the corresponding frequency spectrum…………………………………………………… 62
Figure 5.9: Excitation signal obtained with the ESUS acquisition system and the respective frequency spectrum…………………………………………………………………… 62
Figure 5.10: Echo signal acquired with the ESUS and the corresponding frequency spectrum… ……………………………………………………………………………………... 63
Figure 5.11: Representation of the measured echo signal, the corresponding gamma-tone signal, and the envelope of the gamma signal…………………………………………………… 64
Figure 5.12: Impulse response of the probe obtained with the acquired signal using an arbitrary function generator……………………………………………………………………….. 65
Figure 5.13: Magnitude of the global frequency response of the probe……………………….... 65
Figure 5.14: Global impulse response and convolution of the impulse response with itself…… 66
Figure 5.15: Module of the electric-to-acoustic and acoustic-to-electric frequency response of the probe, corresponding to the electric-to-acoustic transfer function……………………… 66
Figure 5.16: Comparison between the modules of the transfer function determined by the model and the partial frequency response of the probe………………………………………… 67
Figure 5.17: Impulse response that characterizes the electric-to-acoustic signal conversion of the probe as a result of the estimated model………………………………………………… 68
Figure 5.18: Comparison between the echo signal measured with the pulser/receiver and the modeled echo signal using the estimated impulse response……………………….……… 68
Figure 5.19: Impulse response returned by `fsolve`…………………………………………… 69
Figure 5.20: Comparison between the modules of the electric-to-acoustic transfer function given by the solution of the optimization problem and the partial frequency response of the probe determined with the measured signals…………………………………………………… 70

Figure 5.21: Comparison between the echo signal measured with the pulser/receiver and the modeled echo signal using the optimization technique…………………………………….. 70
Figure 5.22: Module of the global frequency response of the probe…………………………… 71
Figure 5.23: Impulse response resulting from the optimization problem using signals acquired with ESUS………………………………………………………………………………. 71
Figure 5.24: Comparison between the modules of the electric-to-acoustic transfer function given by the solution of the optimization problem and the partial frequency response of the probe determined with the measured signals…………………………………………………… 72
Figure 5.25: Comparison between the echo signal measured with the ESUS and the modeled echo signal using the optimization technique…………………………………………….…... 72
Figure 5.26: Pressure signal send by the probe to the medium………………………………… 73
Figure 5.27: Electric simulated signal obtained with the determined acoustic input signal and after the propagation in the eye matrix……………………………………………………..... 74
Figure 5.28: Pressure signal send by the probe to the medium………………………………… 75
Figure 5.29: Electric simulated signal obtained with the determined acoustic input signal and after the propagation in an eye matrix………………………………………………………… 75
Figure 5.30: Spectrum of the part of the electric simulated signal corresponding to the echo from the anterior and posterior lens interfaces obtained with the model using the pulser/receiver.. …………………………………………………………………………........................... 76
Figure 5.31: Spectrum of the part of the electric simulated signal corresponding to the echo from the anterior and posterior lens interfaces obtained with the model using ESUS………… 76
Figure 5.32: Real signal from a healthy eye acquired using ESUS…………………………….. 77
Figure 5.33: Spectrum of the part of the real signal corresponding to the echo from the anterior and posterior lens interfaces…………………………………………………………... 77
Figure 5.34: Spectrum of the part of the acoustic simulated signal corresponding to the echo from the anterior and posterior lens interfaces……………………….................................... 78

List of Tables

Table 3.1: Characteristics of the single element 20 MHz probe of the ESUS prototype.………. 18

Table 3.2: Maximum values of the acoustic indices (MI, $I_{spta,\alpha}$ and TIS), provided by the FDA, and the calibration results.…………………………………………………………. 18

Table 4.1: Radius of curvature and thickness of the interfaces represented in the eye matrix.… 29

Table 4.2: Acoustic properties of the eye structures that compose the eye matrix.…………….. 29

Table 4.3: Maximum pressure of the echoes of the anterior and posterior lens interfaces, for matrices with different grid heights at a resolution of 12 µm; the ratio between the pressure for each `Nx` with the pressure of the full matrix; and the corresponding execution times.……………………………………………………………………………. 32

Table 4.4: Pulse duration of the echo from the anterior lens interfaces, for different values of `Nx` and the corresponding execution times…………………………………………………….. 33

Table 4.5: Computational time of the 2D simulations using matrices with different pixel sizes…………………………………………………………………………………... 35

Table 4.6: Results for the simulation with a 2D matrix with a resolution of 24 µm…………… 37

Table 4.7: Results for the simulation with a 3D matrix with a resolution of 24 µm…………… 37

Table 4.8: Results for the simulation with a 2D matrix with plane interfaces and source/sensor.. ……………………………………………………………………………………... 39

Table 4.9: Results for the simulation with a 3D matrix with plane interfaces and source/sensor.. ……………………………………………………………………………………... 39

Table 4.10: Results for the simulation with a 2D matrix with plane interfaces and curved source/ sensor………………………………………………………………………………. 41

Table 4.11: Results for the simulation with a 3D matrix with plane interfaces and curved source/ sensor………………………………………………………………………………. 41

Table 4.12: Results for the simulation with a 2D matrix with curved interfaces and source/sensor.. ……………………………………………………………………………………... 42

Table 4.13: Results for the simulation with a 3D matrix with curved interfaces and source/sensor.. ……………………………………………………………………………………... 42

Table 4.14: Computational time of the simulation of homogeneous 3D matrices, using GPU… 46

Table 4.15: Dimensions of the microstructures that compose the cortical cataract…………….. 47

Table 4.16: Excursions of the echoes of the lens interfaces from seven real signals, acquired with ESUS…………………………………………………………….......................... 53

List of Acronyms

ADC	Analog-to-Digital Converter
API	Application Programming Interface
CFL	Courant-Friedrichs-Lewy
CPU	Central Processing Unit
CRT	Classification and Regression Tree
EU	European Union
ESUS	Eye Scan Ultrasound System
FDA	Food and Drug Administration
FCT	Fundação para a Ciência e Tecnologia
FFT	Fast Fourier Transform
FLD	Fisher Linear Discriminant
FT	Fourier Transform
GPU	Graphics Processing Unit
IOL	Intraocular Lens
KNN	K Nearest-Neighbour
LTI	Linear Time Invariant
LOCS III	Lens Opacity Classification System version III
MI	Mechanical Index
NC	Nuclear Colour
NO	Nuclear Opalescence
PML	Perfectly Matched Layer
SVM	Support Vector Machine
TIS	Thermal Index for Soft Tissues
UVB	Ultraviolet type B
WHO	World Health Organization

List of Symbols

a_k	Roots of the numerator polynomial of a rational function
A	Amplitude
b_k	Roots of the denominator polynomial of a rational function
C	Proportionality constant of the gamma-tone signal
C_1, C_2	Transfer functions of cables and connectors
C_m	Elastic stiffness
C_o	Clamped capacitance
D	Distance
dx, dy, dz	Grid spacing in the x, y and z directions
D	Transfer function of ADC
E	Young’s modulus
f	Frequency
F	Objective function of `fsolve` MATLAB function
G	Gain factor
h	Impulse response
h^*	Optimal impulse response
H	Electric-to-acoustic and acoustic-to-electric transfer function of the transducer
H_1, H_2	Electric-to-acoustic and acoustic-to-electric transfer function of the transducer, respectively
h_{model}	Impulse response obtained with the estimated model
H_{model}	Electric-to-acoustic and acoustic-to-electric transfer function of the transducer obtained with the estimated model
h_{tot}	Total impulse response
H_{tot}	Electric-to-electric transfer function of the transducer
$I_{spta,\alpha}$	Attenuated spatial-peak temporal average intensity
L	Transfer function of the amplifier
m	Mass
m_r	Radiation mass
n	Shape parameter

N	Mechanical-electric conversion coefficient
Nx, Ny, Nz	Number of grid points in the x, y and z directions
O	Transfer function of the oscilloscope
p	Sound pressure
p_0	Sound pressure at the surface of the source
p_i, p_r, p_t	Sound pressure amplitudes of the incident, reflected and transmitted waves, respectively
P	Order of the numerator polynomial of a rational function
Q	Order of the denominator polynomial of a rational function
r	Envelop of the gamma-tone signal
R	Reflection coefficient
R^2	Coefficient of determination
R_i	Input resistance
R_m	Fraction force resistance of the transducer
R_o	Output resistance
R_r	Radiation resistance
S	Transfer function of the sample
t	Time
t_d	Delay
t_m	Mode of the gamma distribution
T	Transmission coefficient
u	Step function
U_1	Voltage source
U_3	Electric signal at the receiver
v	Ultrasound velocity
v_r	Vibration velocity at the transducer surface
V	Voltage signal at the source
W_1, W_2	Transfer functions of the coupling medium
x	Input signal
X	Transfer function of the input signal
y	Output signal
y_g	Gamma-tone signal
Y	Transfer function of the output signal

Y_g	Transfer function of the gamma-tone signal
z	Acoustic impedance
z_1, z_2	Acoustic impedance of the first and second mediums
α	Attenuation coefficient
α_0	Power law prefactor
β	Decay temporal coefficient
$\mathit{\Gamma}$	Gamma function
$\mathit{\Delta} t$	Time interval
η	Power law absorption exponent
θ_i, θ_r	Incident and reflected angles
λ	Wavelength
μ	Mean of the gamma distribution
ρ	Density
ϕ	Phase
ω	Angular frequency
ω_0	Center angular frequency

1. Introduction

1.1. Motivation

Cataract is an opacity of the crystalline lens that affects its transparency and sensitivity to light, leading to visual function deterioration and, ultimately, loss of sight if left untreated. Although there are genetic and environmental factors that influence cataract formation, age is the risk factor that most contributes to the development of cataract (Michael and Bron, 2011). According to the World Health Organization (WHO), cataract is the main cause of addressable vision impairment and blindness on a global scale. Out of all the 2.2 billion people affected by a visual impairment globally, 1 billion have a visual impairment that is either able to be prevented or is yet to be addressed, such as cataract, a condition that affects 65.2 million people around the world (WHO, 2019).

Surgical removal of the lens is the only effective treatment since there is no other therapy for cataract. Currently, cataract surgery is a cost-effective procedure that provides rapid visual rehabilitation with minimum complications for the patient (Queirós et al, 2021). In 2016 Portugal was the country in the European Union (EU) with the highest rate of cataract operations, with 14 procedures per thousand inhabitants (Eurostat, 2019). As a result of the aging population and the greater life expectancies, it is estimated the cataract cases to increase and, therefore, the demand for cataract surgery (Wang et al, 2016).

Phacoemulsification is the most widely used surgical technique for lens extraction, which can be performed at any stage of cataract development. This technique uses ultrasound or laser energy to emulsify the lens into fragments that are afterward removed by aspiration. After this, an artificial lens is implanted, supported by the posterior lens capsule that remains in the eye. Although this method for lens extraction has a high success rate, there can be some postoperative complications. The most common phacoemulsification complications are corneal edema and posterior capsule rupture (Queirós et al, 2021; Martínez et al, 2021). This tissue damage may be caused by excessive ultrasonic power. To determine the correct ultrasound energy to be applied, it is important to predict the cataract hardness. There are qualitative ways to determine the severity of the cataract, such as LOCS III, which is currently the most used system for cataract classification. The LOCS III is based on the comparison of acquired slit-lamp images of the lens with a set of standard images (Zaki et al, 2022).

Some pre-clinical studies have demonstrated that high-frequency ultrasound can be used to detect cataract and quantify its hardness (Caixinha et al, 2016b; Huang et al, 2007b).

The present work is part of the CATARACTUS project (POCI-01-0145-FEDER-028758), financed by Fundação para a Ciência e Tecnologia (FCT). This project proposes the development of a medical device based on ultrasounds intended to support cataract surgeries, by detecting and classifying cataract types and severities and by accessing its hardness in real-time, therefore, providing the optimal phacoemulsification energy level to be applied in the surgery.

1.2. Objectives

The objective of the present work was to establish a complete computational model of the Eye Scan Ultrasonic System (ESUS) used for the detection and classification of cataracts and the propagating medium (the eye). The model includes electric-to-acoustic signal conversion on the ultrasound probe, ultrasonic waves propagation through the eye, and acoustic-to-electric signal conversion again on the probe, considering that the probe operates in the pulse-echo mode.

The objectives of the present work can be reduced to the following:

1. To evaluate the feasibility of 3D simulation at micrometric resolution.
2. To model the electric-to-acoustic and acoustic-to-electric conversion in the ultrasonic probe in terms of its impulse response.
3. To use the obtained model to perform a simulation and compare the outcome with real acquired signals.

1.3. Thesis Organization

This thesis is divided into six chapters. The first one corresponds to the introduction, presenting the motivation behind the present work (1.1), the objectives (1.2), and a subchapter describing the thesis organization (1.3).

The second chapter aims to present some background concepts regarding the crystalline lens, the cataract, phacoemulsification (2.1), ultrasounds (2.2), and ultrasonic transducers (2.3), that constitute the theory to the understanding of the context of this project.

The bibliography revision that supports the development of the project is contained in chapter 3. In this third chapter, studies related to the use of ultrasounds for the detection and classification of the cataract are mentioned (3.1), as well as the development of the clinical prototype for automatic classification of the cataract (3.2). Also, a study regarding the simulation of ultrasonic waves propagation is present (3.3). Finally, some studies regarding the model of ultrasonic transducers were referred to (3.4).

Chapter 4 describes the work performed in the scope of the simulation of ultrasound inside the eye using the k-Wave MATLAB toolbox. The description of this method for acoustic simulation is presented at the beginning of this chapter (4.1). The results of some experiments with 2D simulations (4.2 and 4.3) and the transition to 3D simulation and the comparison between 2D and 3D simulation (4.4) are described. The test of a simulation in stages is described (4.5), as well as a definition of an improved resolution for 3D simulations (4.6). A summary of the important results of this chapter (4.7) is also included.

The fifth chapter includes the methods and materials used to estimate the model of the ophthalmologic probe (5.1). The results are then presented in sections 5.2, 5.3, 5.4, and 5.5, including the comparison with the real signals obtained with the ESUS system (5.6).

Finally, in the last chapter (6) the conclusions arising from the developed work are discussed, along with future work.

2. Background Concepts

2.1. Crystalline Lens and Cataract

2.1.1. Crystalline Lens

The crystalline lens is an intraocular transparent eye structure that continues to grow as the individual ages. This avascular element presents a variable biconvex shape and has the capacity to focus light on the retina, a process that makes vision possible (Ecroyd and Craver, 2009). The lens can change its shape and refractive power, depending on the distance from the object, to sharpen the image on the retina, where the light is detected. This is possible due to the attachment of the lens to the ciliary muscle. The contractions of this muscle enable the lens to change its curvature and thickness and, therefore increase its refractive power (Irsch and Guyton, 2009). This function is called accommodation and it tends to decrease with age (Michael and Bron, 2011).

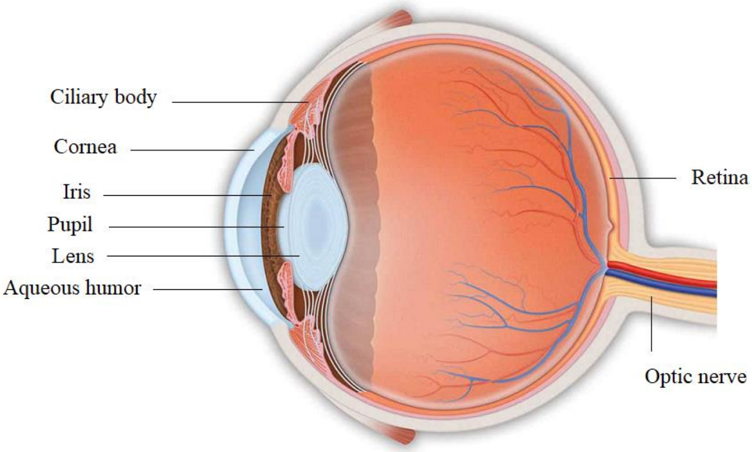

Figure 2.1. Anatomy of the eye. Adapted from Glaucoma Research Foundation[1].

The crystalline lens is positioned posterior to the iris and is supported by zonular fibers arising from the ciliary body (figure 2.1). The lens is surrounded by a capsule and divided in two main regions: the nucleus, corresponding to the central part of the lens, and the cortex, which is the outer part of the lens, as it is represented in figure 2.2 (Riordan-Eva and Cunningham, 2011).

---

[1] https://glaucoma.org/eye-anatomy/

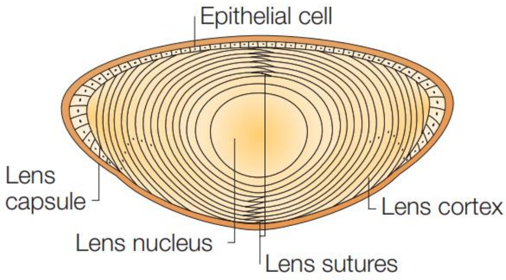

Figure 2.2. Anatomy of the crystalline lens. Adapted from (Graw, 2003).

The transparency of the lens depends on the arrangement of the crystalline proteins in its composition. When protein aggregation and precipitation occur, the arrangement of the proteins is compromised, leading to lens opacification and coloration, increased hardness, and light-scattering. These factors are involved in cataract formation (Ecroyd and Craver, 2009).

2.1.2. Cataract

A cataract is a cloudiness in the eye lens, resulting from transparency loss and increased light-scattering caused by modifications in the arrangement of the crystalline proteins (Michael and Bron, 2011).

Individuals diagnosed with cataract experience blurry vision, increased sensitivity to light, and difficulty seeing at night. Since the cataract causes a reduction in the contrast and resolution of the image, other symptoms include distortion, seeing ghosted images out of the eye with cataract, and decreased ability to distinguish colors, seeing them faded (Gross et al, 2008; American Academy of Ophthalmology, 2021).

A significant part of cataract cases is age-related, once aging is the main risk factor for cataract development (Michael and Bron, 2011). However, cataract is a multifactorial condition and there are environmental factors that might influence cataract development, such as cigarette smoking and UVB exposure. Also, some diseases are associated with an increased prevalence of cataract, such as diabetes (WHO, 2019).

There are three types of cataracts, illustrated in figure 2.3, depending on where the lens opacity is located. The cataract is called a nuclear cataract if the opacity occurs in the nucleus. Cortical cataract corresponds to opacities that emerge in fiber cells in the cortex, and posterior subcapsular cataract appears in the posterior pole, near the posterior capsule (Beebe et al, 2010).

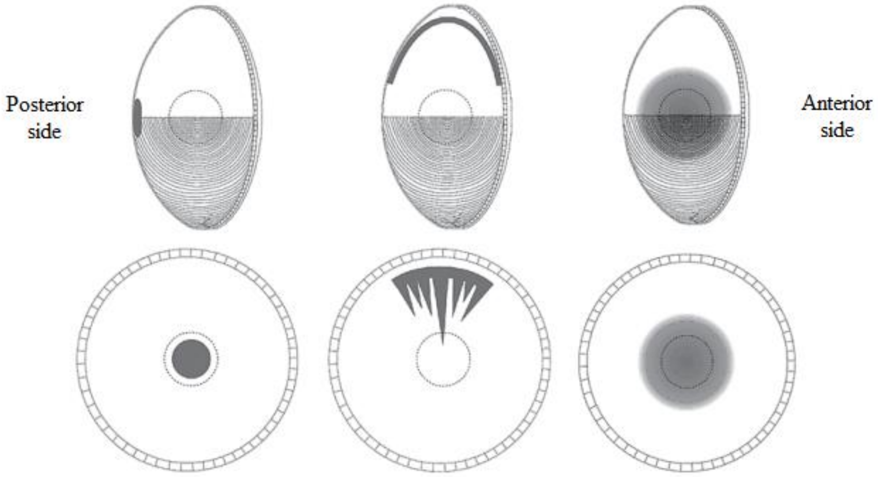

Figure 2.3. Diagram representing the three types of cataracts: posterior subcapsular cataract (left), cortical cataract (center) and nuclear cataract (right). A cross-sectional view is illustrated on the top, as the front view is represented at the bottom. Adapted from (Beebe et al, 2010).

Cataract is a leading cause of visual impairment and blindness worldwide. In developed countries, cortical cataract is the most prevalent age-related cataract, about four times more frequent than nuclear opacifications (Michael and Bron, 2011; Michael et al, 2008).

There is no solution to prevent age-related cataract and currently the only treatment is surgical intervention. Cataract surgery restores vision through lens removal followed by insertion of a new artificial lens with a fixed refractive power inside the eye (Gross et al, 2008).

2.1.3. LOCS III Cataract Classification System

Lens Opacities Classification System III (LOCS III) is a qualitative system of age-related cataract classification, and currently, it is one of the most used by ophthalmologists (Chylack et al, 1993; Zaki et al, 2022).

The presence and severity of the cataract are graded by comparing its appearance in slit-lamp and retroillumination images in opposition to a set of standard reference photographs. This version of LOCS uses slit-lamp images for grading nuclear color (NC) and nuclear opalescence (NO), and retroillumination images for evaluating cortical cataract (C) and posterior subcapsular cataract (P) (Figure 2.4) (Zaki et al, 2022).

The severity level range used in the reference standard for the opalescence of the nuclear cataract (NO) and its color (NC) is from 1 to 6 (NO1 to NO6 and NC1 to NC6, respectively). A severity level ranging from 1 to 5 is used for the cortical cataract (C) (C1 to C5) and posterior subcapsular cataract (P) (P1 to P5) (Chylack et al, 1993).

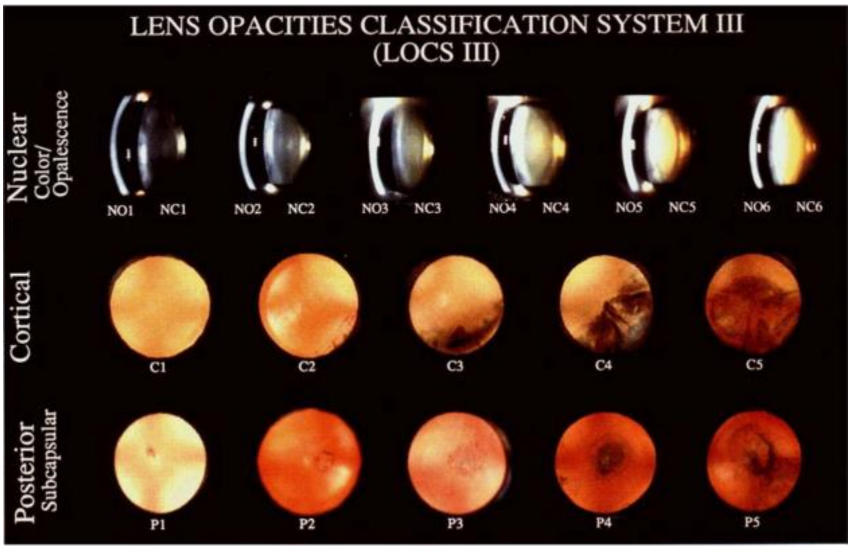

Figure 2.4. LOCS III Grading Standard. N01 to N06 and NC1 to NC6 are the standards for nuclear opalescence and nuclear color, respectively (upper line). C1 to C5 are the standards for cortical cataract (middle line), and P1 to P5 are the standards for posterior subcapsular cataract (bottom line). Adapted from (Chylack et al. 1993).

Although this is a subjective system depending on the physician's experience, the LOCS III classification contributes to more effective cataract surgery by helping estimate the energy to be used, since higher grading scores assessed using LOCS III indicate greater severities, therefore requiring higher energy levels for the cataract removal (Chylack et al, 1993; Davinson and Chylack, 2003).

2.1.4. Phacoemulsification

Cataract surgery is the only therapy for cataract treatment since there is no pharmacological solution to overcome this problem. Phacoemulsification is the most common procedure to extract a lens affected by cataract, using ultrasound or laser energy (Fine et al, 2002). This intervention can be adopted at any stage of cataract development and presents great visual outcomes, as patients experience fast recovery and minimal complications (Queirós et al, 2021; Martínez et al, 2021).

The ultrasonic phacoemulsification procedure consists of a small corneal incision, through which passes a hand-held probe with a tip that vibrates to disintegrate and emulsify the lens material (Fine et al, 2002; Martínez et al, 2021). Ultrasound energy is generated in this process, as the vibration frequency is in the ultrasound range (Packer et al, 2005). The resulting fragments are aspired through the same probe. Once the cataractous lens is removed, an intraocular lens (IOL) is implanted. The posterior lens capsule should remain intact to support the IOL (Martínez et al, 2021).

Phacoemulsification is a highly effective and safe technique. However, some intraoperative and postoperative complications may arise, causing recovery retardment (Martínez et al, 2021). These surgical complications are a result of different factors related to the patient, such as age and cataract density, or to the intervention itself, including phacoemulsification time, phacoemulsification energy, and surgeon experience. Common postoperative complications are corneal edema and endothelial cell loss. These problems may be minimized if the ultrasonic power and phacoemulsification time are reduced (Abell et al, 2014). Posterior capsule rupture is an intraoperative complication related to excessive levels of phacoemulsification energy that deserves attention since the integrity of the posterior capsule is crucial to the success of the surgery and its disruption may induce additional unwanted events, such as IOL displacement and retinal detachment (Martínez et al, 2021).

2.2. Ultrasounds

Sound is a mechanical form of energy, produced by a vibrating source (Tole, 2005). The mechanical vibration propagates throughout a medium by elastic deformation of the particles of the medium (Schirru, 2017). The number of vibrations per unit time is called the frequency (f), commonly measured in hertz (Hz). Audible sounds are those which can be perceived by the human ear. The audible frequency range is approximately 20 Hz – 20 kHz. Sound waves with frequencies higher than that of human perception are referred to as ultrasound (Tole, 2005).

Of all the different types of waves, longitudinal waves are the most used in the study of biological tissues. In this case, the particles of the medium oscillate backward and forwards along the direction of propagation of the wave. This particle displacement creates regions of compression, when particles move towards each other, resulting in higher pressure zones, and regions of rarefaction when particles move apart, giving rise to low pressures. The particle movement pattern over time can be described by a sine wave (figure 2.5) (Tole, 2005; Hoskins et al, 2010). The amplitude (A) of the wave is described as the pressure difference between the maximum pressure and the mean pressure in the medium, measured in pascals (Pa) (Krautkramer and Krautkramer, 2002; Hoskins et al, 2010).

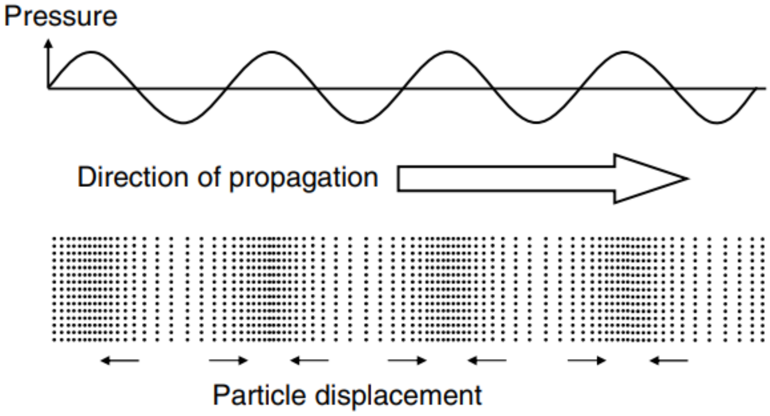

Figure 2.5. Particle displacement in a longitudinal wave, creating rarefaction (low pressure) and compression (high pressure) regions. Reproduced from (Hoskins, 2010).

The wavelength (λ) is the distance between two consecutive equivalent positions on the wave. It is inversely proportional to the frequency and represents the traveled distance during one complete wave cycle. The speed at which sound waves travel is the velocity of propagation (v) and it is a constant characteristic of a given material (at constant temperatures) for any frequency and any wavelength, as represented in equation 2.1 (Tole, 2005; Krautkramer and Krautkramer, 2002).

$$v = \lambda f \tag{2.1}$$

The sound speed differs from one medium to another, depending on the properties of the medium itself. If the medium particles are close to each other, as in solid materials, then the sound speed should be higher than in a medium where the particles are far from one another, such as gases like air (Tole, 2005).

2.2.1. Ultrasound Interaction with Matter

As an ultrasound beam propagates through a medium, the interaction with the medium particles is influenced not only by the characteristics of the ultrasound wave but also by the physical properties of the material where the wave propagates (Tole, 2005). One important acoustic property of materials is the acoustic impedance (z) defined as the resistance of the particles of the medium to mechanical vibrations, given by the product of density (ρ) and v (equation 2.2), and is measured in Rayl (Pa.s.m^{-1}) (Tole, 2005; Krautkramer and Krautkramer, 2002).

$$z = \rho v \qquad (2.2)$$

When there is a change in the acoustic impedance, the ultrasound wave reflects on the interface (also called an acoustic boundary) separating the two mediums with different acoustic impedance. As a result, part of the ultrasound wave is redirected back into the first medium and some is transmitted into the second medium. If the boundary is smooth and larger than the ultrasound wavelength, specular reflection takes place, which is an interaction ruled by the law of reflection (illustrated in figure 2.6). This law considers that the angle between the incident beam and the perpendicular direction to the reflecting surface (incident angle, θ_i) and the angle between the same perpendicular and the reflected beam (reflected angle, θ_r) are equivalent ($\theta_i = \theta_r$) (Tole, 2005; Hoskins et al, 2010).

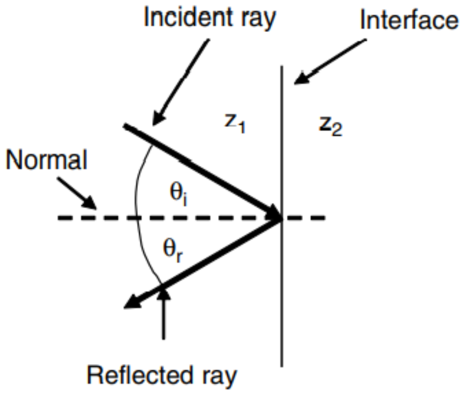

Figure 2.6. Non-perpendicular incidence at a large and smooth interface. The angle of reflection is equal to the angle of incidence. Reproduced from (Hoskins, 2010).

The fraction of pressure reflected on the interface is represented by the reflection coefficient (*R*), while the proportion of the incident pressure that is transmitted across the interface is given by the transmission coefficient (*T*). Considering the case where perpendicular incidence takes place, these coefficients can be determined by equations 2.3 and 2.4, where p_i, p_r and p_t are the pressure amplitudes of the incident, reflected and transmitted waves, respectively, and z_1 and z_2 are the acoustic impedances of the first and second medium (Tole, 2005; Hoskins et al, 2010).

$$R = \frac{p_r}{p_i} = \frac{z_2 - z_1}{z_2 + z_1} \qquad (2.3)$$

$$T = \frac{p_t}{p_i} = \frac{2z_2}{z_2 + z_1} \qquad (2.4)$$

Scattering occurs when a material presents an inhomogeneity. When an ultrasound wave encounters an irregular interface with dimensions smaller or near the ultrasound wavelength, the wave is scattered over a large range of directions, as it is illustrated in figure 2.7 (Tole, 2005; Hoskins et al, 2010; Schirru, 2017; Krautkramer and Krautkramer, 2002).

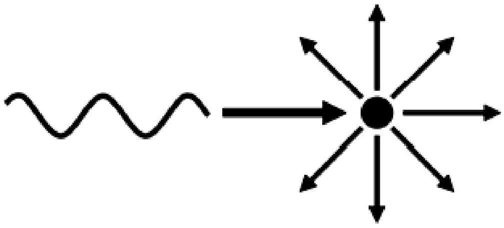

Figure 2.7. Representation of scattering. The incidence in a small target causes reflection over a wide range of directions. Reproduced from (Hoskins, 2010).

As the ultrasound beam travels through a medium, there is a reduction of sound pressure along its path, resulting from attenuation. Attenuation is defined as the gradual loss of ultrasound energy as the wave travels through the medium. Absorption is the dominant form of attenuation, which is a direct conversion of ultrasound energy into heat in the medium (Tole, 2005; Hoskins et al, 2010; Krautkramer and Krautkramer, 2002). Scattering is also a mechanism that contributes to attenuation (Tole, 2005).

The attenuation coefficient (α) reflects the rate at which the intensity of the ultrasound wave is attenuated, in units of dB.cm^{-1}. The attenuation coefficient of most tissues is frequency-dependent and given by equation 2.5, where f is the frequency and α_0 and η are the parameters that characterize the attenuation of the tissue. For soft tissues, it is assumed that the value of η is close to unity, and therefore the attenuation coefficient increases almost linearly with frequency (Narayana and Ophir, 1983; Hoskins et al, 2010).

$$\alpha = \alpha_0 f^{\eta} \tag{2.5}$$

The sound pressure of a wave is given by the equation 2.6, where d is the distance from the source, and p_0 represents the sound pressure at d = 0 (Schirru, 2017; Krautkramer and Krautkramer, 2002).

$$p = p_0 e^{-\alpha d} \tag{2.6}$$

2.3. Ultrasound Transducers

2.3.1. Ultrasound Transducers Concepts

The generation and reception of ultrasounds are based on the piezoelectric effect, which involves the conversion of electrical energy to mechanical energy and vice-versa. This is a characteristic of some crystalline materials, the piezoelectric materials (Schirru, 2017). These materials have the property to expand or contract when an electric voltage is applied across them. On the other hand, when compressed or stretched by an external force, an electrical charge will appear on their surfaces (Hoskins et al, 2010; Tole, 2005).

The piezoelectric materials are the main components of ultrasound transducers (figure 2.8). Since the piezoelectric effect is a reversible phenomenon, the same element can be used to produce ultrasound and to detect echoes returning to the element from a reflector at some distance away (Tole, 2005).

Besides the piezoelectric elements, other components of the transducer include electrical connections, external housing, insulating material, a matching layer, and backing material. The backing is a material with a high acoustic impedance that is placed behind the active element and is responsible for damping oscillations of the active element and absorbing the ultrasound wave transmitted back into the transducer (Hoskins et al, 2010; Krautkramer and Krautkramer, 2002; Tole, 2005). The insulating material eliminates the influence of external electrical sources on the active element and prevents the vibrations of the piezoelectric material from passing to the external housing that covers all the components of the transducer (Tole, 2005). The transducers are also composed of at least one matching layer bonded to the front face of the active element to improve the performance of the transducer by increasing the energy transmitted across the front face of the active element (Zhou et al, 2014; Hoskins et al, 2010).

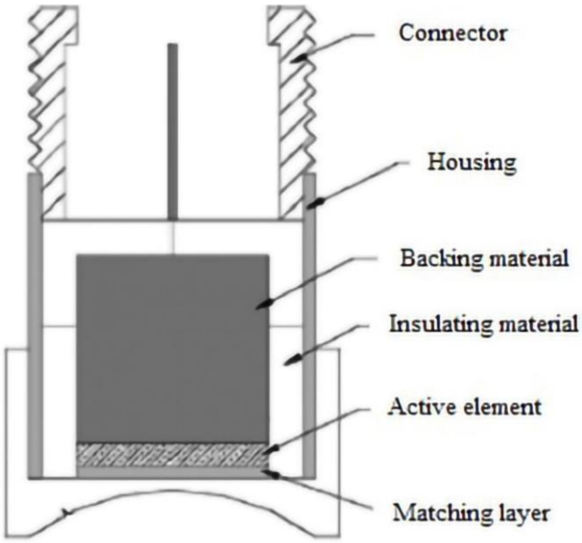

Figure 2.8. Schematic representation of an ultrasound transducer. Adapted from (Zhou et al, 2014).

Ultrasound transducers can be composed of a single active element or an array of elements. Single-element transducers are the most common configuration used in ophthalmologic applications. They contain only one active element and have a fixed focal length. These transducers can be classified as planar or focused transducers. Focused transducers can be fabricated either by shaping the piezoelectric element or using a lensing material (Silverman, 2016; Zhou et al, 2014). In a focused field, the ultrasonic energy is focused on a point in space called the focal point, while the non-focused field is characterized by a first zone called the near field and by an area where the ultrasonic beam spreads out called the far field, as it is presented in figure 2.9 (Hoskins et al, 2010; Schirru, 2017).

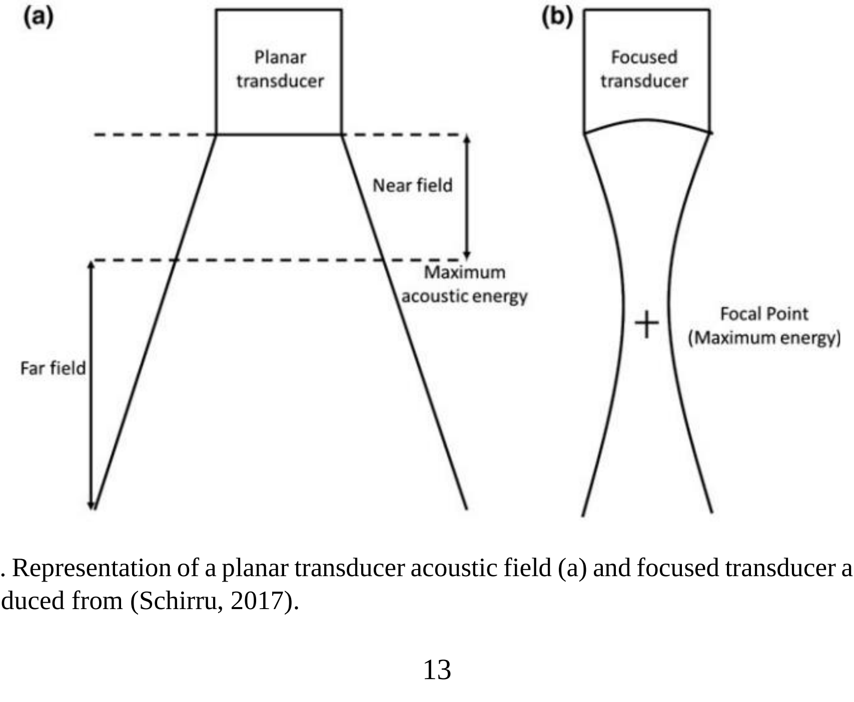

Figure 2.9. Representation of a planar transducer acoustic field (a) and focused transducer acoustic field (b). Reproduced from (Schirru, 2017).

2.3.2. Ultrasound for Diagnosis

There are two main methods to generate and detect ultrasounds: pulse-echo and transmission method. In the pulse-echo method, the same transducer is used to produce ultrasound and detect the echoes after the wave propagates through the medium (Tole, 2005). The transmission method requires a transducer to emit the ultrasound wave and another transducer, which is located on the opposite side of the medium, to receive the ultrasound signal after the propagation of the wave. The most used method in medicine is the pulse-echo method (Schirru, 2017).

In the case where the pulse-echo method is used, the ultrasound wave travels from the transducer, working as an emitter, propagates through the medium where experiences reflections and scatters in acoustic boundaries, and returns to the same transducer which is then working as a receiver (Hoskins et al, 2010; Tole, 2005).

There are two major display modes employed in ophthalmology: A-scans and B-scans. With A-scan mode (amplitude scan) the amplitude of the signals from returning echoes is displayed as a function of time (figure 2.10). A B-scan (brightness scan) generates a cross-sectional 2D image constructed from successive A-scans, where the horizontal axis represents the probe position, the vertical axis the image depth and the brightness at each point is proportional to echo amplitude (figure 2.11) (Hoskins et al, 2010; Silverman, 2016; Tole, 2005).

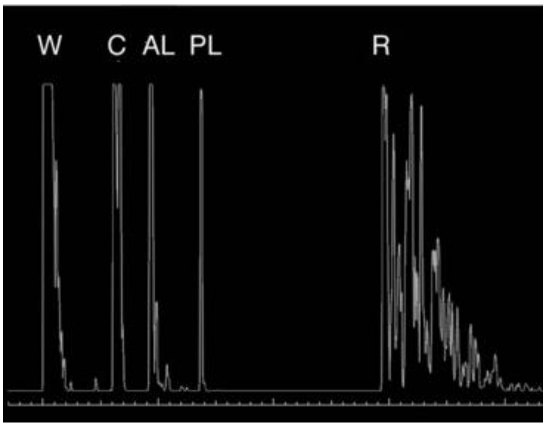

Figure 2.10. A-scan of a normal eye. The spikes correspond to water (W), anterior and posterior cornea (C), anterior (AL) and posterior lens (PL), and retina (R). Reproduced from (Rocha and Krueger, 2008).

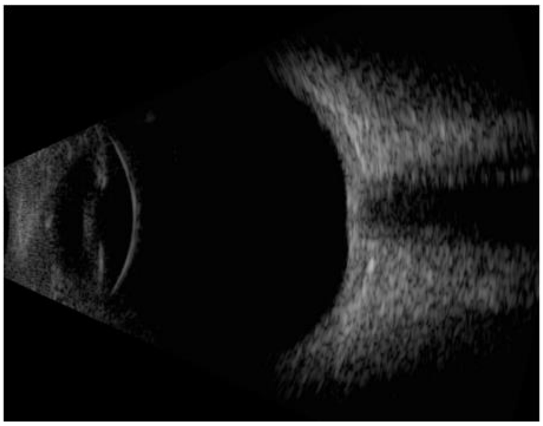

Figure 2.11. B-scan of a normal eye. Reproduced from (Silverman, 2016).

3. State of the Art

3.1. Cataract Evaluation Using Ultrasounds

Over the years, high-frequency ultrasounds have been used in ophthalmology for the study of diverse eye diseases, and some preclinical studies have demonstrated that A-scan ultrasound can be used to noninvasively assess cataract hardness and automatically classify the cataract through machine learning techniques.

Huang et al. (2007a) evaluated the hardness of *in-vitro* porcine lenses with artificially induced cataracts at different severity levels by measuring the acoustic parameters (velocity and attenuation) and the elastic properties, such as the Young's modulus (*E*). The authors observed an increase of the Young's modulus with cataract formation, demonstrating that the lens hardness increases with severity. This study found a linear relation between the phacoemulsification energy and ultrasonic parameters, as it was observed that when the sound velocity or attenuation increases it is required higher phacoemulsification energy to emulsify the lens. Therefore, these parameters can be used to noninvasively estimate the cataract hardness.

The work developed by Caixinha et al. (2014) and Caixinha et al. (2016a) studied different cataract degrees induced in *ex-vivo* porcine lenses. The levels of severity of the cataracts were induced by increasing the immersion time of the lens in a solution containing ethanol:2-propanol:formalin. The acoustic parameters sound velocity and frequency dependent attenuation were determined using a 25 MHz ultrasonic probe, and it was observed that both parameters increased significantly with immersion time. This is in good agreement with previous studies carried out by Huang et al. (2007a) and Huang et al. (2007b).

In these studies were also constructed B-scan and parametric Nakagami images. The Nakagami images provide information regarding the concentrations and distributions of scatterers in tissue by reflecting the statistical distribution of the backscattered signals. The B-scan images showed a rise in backscattering amplitude as the cataract becomes more severe, since the mean brightness intensity increased with cataract formation, as it is represented in figure 3.1. The authors used the extracted acoustic parameters and the B-scan and Nakagami images to perform machine learning techniques to verify whether the different parameters can predict the presence of cataract and, in the case of cataractous lenses, classify the cataract as incipient or severe. In the first study, Caixinha et al. (2014) observed that 87.1% of the lenses were correctly classified by a classification and regression tree (CRT). Caixinha et al (2016a) used different classifiers: Bayes, K Nearest-Neighbor (KNN), Fisher Linear Discriminant (FLD), and Support Vector Machine (SVM). All four classifiers showed good performance (above 92.68%) when classifying healthy and cataractous lenses. However, for the classification into incipient and severe cataractous lenses, only the SVM classifier presented a good performance (90.62%).

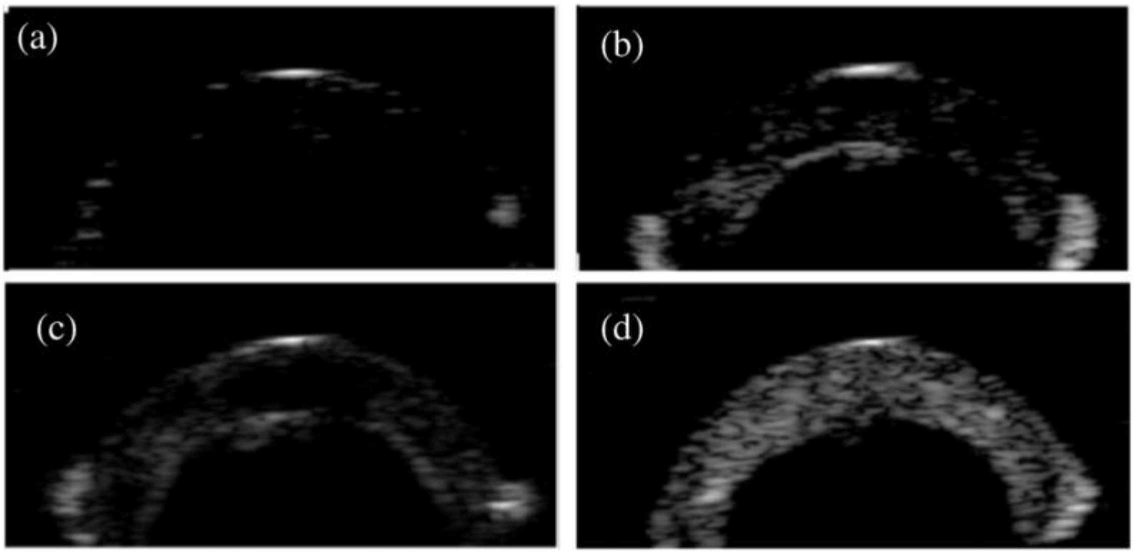

Figure 3.1. B-scan images for lenses without cataract (a), and with incipient (b), moderate, (c) and severe (d) cataract. Cataracts in (b), (c) and (d) were induced by increasing immersion time (60, 120 and 180 minutes, respectively) in ethanol:2-propanol:formalin solution. Reproduced from (Caixinha et al, 2014).

Caixinha et al. (2016b) used an *in-vivo* animal model with rats to obtain different severity degrees of nuclear cataract. Diverse features were extracted from the A-scan signals acquired with a 20 MHz ultrasonic probe to perform cataract classification and distinguish between healthy, incipient, moderate, and severe cataract. An A-scan signal is illustrated in figure 3.2. The observed echoes occur when the ultrasonic wave is reflected in the interface between two eye structures. The nuclear cataract, delimited by the dotted circle in the figure, originates backscattering between the reflections in the anterior and posterior lens interfaces. As a result of attenuation, the amplitude of the reflections decreases as a function of the distance to the probe, and the echoes generated from the posterior lens and the structures in the back of the eye (retina, choroid, and periorbital fat) present low amplitude.

Besides the *in-vivo* approach, *post-mortem* and *ex-vivo* signals were also acquired to prove that the eye movements *in-vivo* and the probe misalignment in relation to the ocular surface do not interfere with the results of the classification. Different machine learning techniques were used in this study to classify cataract severity. The SVM turned out to be the most powerful classifier as it was the one that showed the highest performance and lowest classification error, with sensitivity and specificity both of 99.7% (Caixinha et al. 2016b).

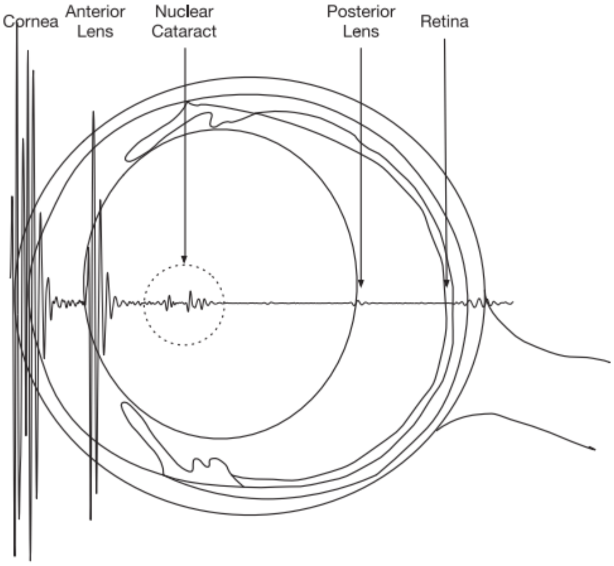

Figure 3.2. A-scan signal obtained from a rat eye with induced nuclear cataract. Reproduced from (Caixinha et al, 2016b).

3.2. ESUS Acquisition System

As a result of the positive outcomes from the previous studies integrated in the CATARATA project (PTDC/DTP-PIC/0419/2012) (Caixinha et al. 2014, Caixinha et al. 2016a, Caixinha et al. 2016b), a clinical prototype of the Eye Scan Ultrasound System (ESUS) for automatic cataract characterization was developed (Petrella et al, 2020). The development of this device is included in the CATARACTUS project.

The ESUS consists of three main components: the A-scan ophthalmic probe, the xSCAN, and the computer, as it is represented in figure 3.3.

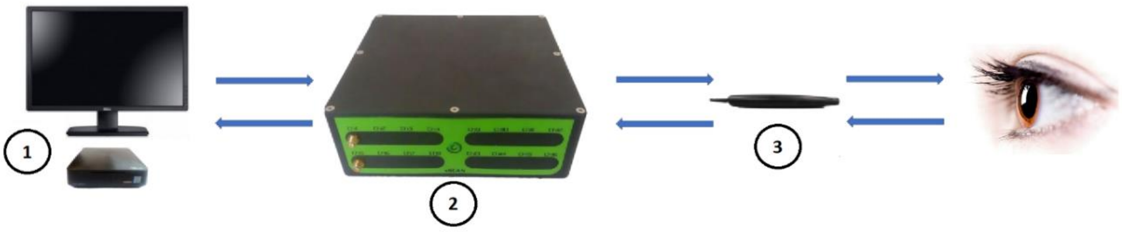

Figure 3.3. Components of the ESUS acquisition system. 1) Computer, 2) xSCAN, 3) A-scan ophthalmic probe. Adapted from (Pinto, 2019).

The ophthalmic transducer (Imasonic SAS, Bourgogne-Franche-Conté, France) consists of a mono-element probe working in pulse-echo mode, with a radius of curvature of 9 mm, a diameter of 3.2 mm, a focal distance of approximately 8 mm and a nominal frequency of 20 MHz.

These characteristics are represented in table 3.1. The xSCAN system (Tribosonics Ltd., Sheffield, UK) generates electrical signals that enable the probe excitation and acquires the backscattered signals received by the probe. This element also works as an analog-to-digital converter (ADC) of the received signals at a 100 MHz sampling rate and performs signal conditioning. The xSCAN is controlled by a computer that is also responsible for receiving and processing the signals acquired by the xSCAN. To communicate with the xSCAN through the computer, it was developed an application programming interface (API) in C++ together with a graphical user interface in MATLAB. These tools enable the user to visualize the acquired A-scan signals in real-time and save them to a computer hard disk (Petrella et al, 2020; Pinto, 2019).

Table 3.1. Characteristics of the single element 20 MHz probe of the ESUS prototype.

Nominal frequency	20 MHz
Active element diameter	3.2 mm
Acoustical focal distance	8 mm
Nominal radius of curvature	9 mm
Bandwidth (-6dB)	≥ 55%

Once the goal is to use the described prototype for a clinical trial, the safety assessment was required to evaluate potential risks. The risk management was based on three acoustic indices: the mechanical index (MI), the thermal index for soft tissues (TIS), and the attenuated spatial-peak temporal-average intensity ($I_{spta,\alpha}$) (Petrella et al., 2020). Calibration results were compared with the maximum values of the acoustic indices for ophthalmic applications, provided by the US Food and Drug Administration (FDA), and the results are presented in table 3.2. It was observed that all the evaluated indices are within the safety range, and therefore, the device is adequate for clinical application.

Table 3.2. Maximum values of the acoustic indices (MI, $I_{spta,\alpha}$ and TIS), provided by the FDA, and the calibration results. Retrieved from (Petrella et al, 2020).

Parameter	Maximum value	Calibration Result
MI	0.23	0.08 ± 0.05
$I_{spta,\alpha}$ (mW/cm^2)	17	0.56 ± 0.59
TIS	1	0.08 ± 0.08

3.3. Simulation of Ultrasound Propagation Using k-Wave

To simulate the acoustic propagation through the eye, the k-Wave[2] MATLAB toolbox is a helpful tool, since it enables time-domain simulations of acoustic fields in 1D, 2D, and 3D (Treeby et al, 2016). Previous studies integrated in the CATARACTUS project implemented 1D and 2D simulations of ultrasound propagation through the eye (Lopes, 2020; Petrella et al, 2021). Petrella et al. (2021) developed a computational tool for the 2D simulation of A-scan ultrasound propagation through the different eye structures, considering healthy and cataractous lenses. An eye grid was constructed using MATLAB, consisting of a matrix with a pixel size of 12 µm, 2048 pixels high and 2187 pixels wide (24.6 mm high and 26.2 mm wide), and it is represented in figure 3.4.

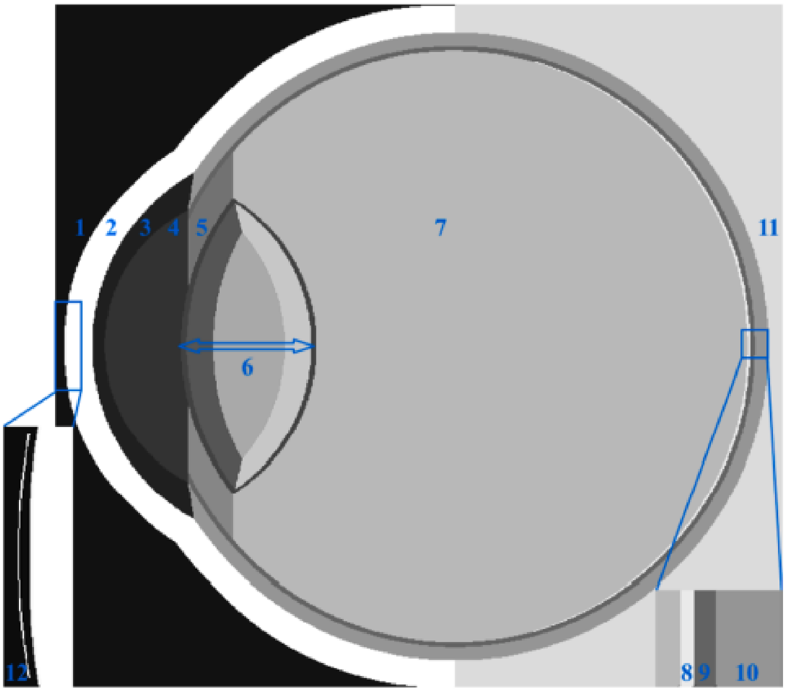

Figure 3.4. 2D eye matrix used in the simulations by Petrella et al (2021). 1) water, 2) eyelid, 3) cornea, 4) aqueous humour, 5) iris, 6) lens including four sub-regions: anterior, central, and posterior layers (for simulation of cortical, nuclear, and posterior subcapsular cataract, respectively) and an exterior capsule, 7) vitreous humour, 8) retina, 9) choroid, 10) sclera, 11) periorbital fat, 12) source/sensor profile.

The dimensions of the different eye structures in the matrix were based on the thicknesses and radius of curvature present in the literature. The cataract was simulated by changing the

---

[2] http://www.k-wave.org/

acoustic properties of the affected regions of the lens, and the different severity levels were based on the LOCS III.

The simulation using k-Wave requires the following input structures: medium, source, sensor, and excitation pulse. To define the medium, the tissue properties must be specified before performing the simulation (Treeby et al, 2016). Therefore, the sound speed, density, and attenuation coefficient for each region of the eye grid were obtained from the literature. The source and sensor were based on the experimental ophthalmic probe described before, working in pulse-echo mode, and its characteristics were specified in table 3.1. The simulation tool includes a user-friendly interface, also developed in MATLAB, so that the user can define the characteristics of the propagation medium and the configuration of the excitation pulse before running the simulation. An example of a simulated signal from a healthy and a cataractous lens is represented in figure 3.5.

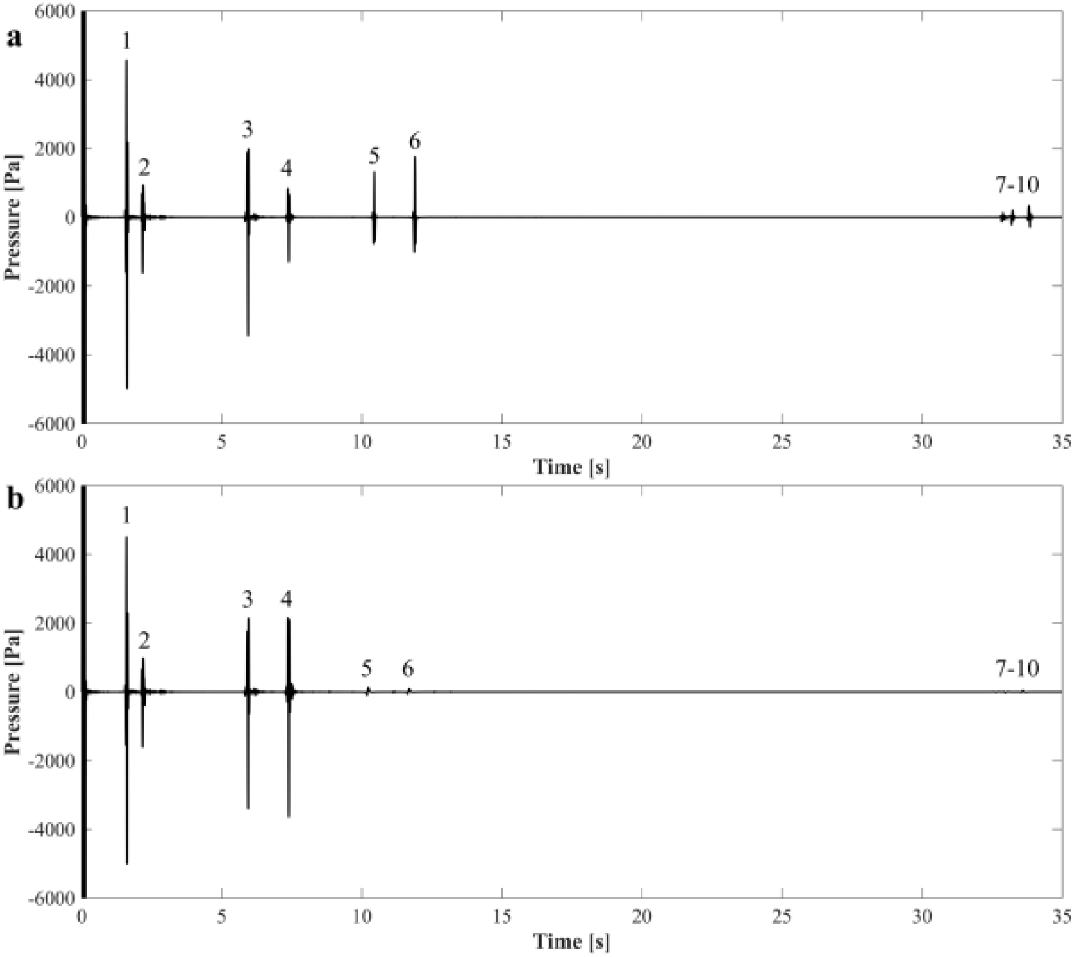

Figure 3.5. Simulated signals of a a) healthy lens, b) cataractous lens, using water coupling, a burst of 20 MHz, 3 cycles and 180 kPa, with attenuation. The echoes reflected in the interfaces of the eye are numbered: 1) water/ cornea, 2) cornea/ aqueous humor, 3) aqueous humor/ lens, 4) lens cortex/ nucleus, 5) lens nucleus/ cortex, 6) lens/ vitreous humor, 7) vitreous humor/ retina, 8) retina/ choroid, 9) choroid/ sclera, 10) sclera/ periorbital fat. Reproduced from (Petrella et al, 2021).

Petrella et al. (2021) observed that when simulating a cataractous lens, the amplitude of the echoes changes, and in cases of severe cataract, signals behind the lens are strongly attenuated, as the echo from the lens/vitreous humor interface (figure 3.5b). Lopes (2020) compared 1D and 2D simulated signals and concluded that the amplitudes of the echoes in 2D simulations are lower than the respective ones in 1D simulations. This occurs since in 2D the sensor and the eye profile are curved, being so, the echoes from the eye structures do not arrive at the same time to the sensor and the average of all points of the sensor is lower in the 2D model. On the other hand, in 1D the sensor is only a dot, and the eye is represented as a line (figure 3.6).

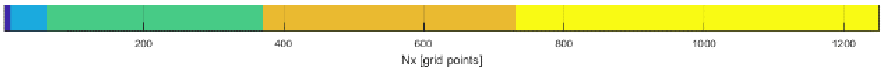

Figure 3.6. 1D eye model used for the simulations. The structures are coloured: damping medium (dark blue), cornea (light blue), aqueous humor (green), lens (orange) and vitreous humor (yellow).

Petrella et al. (2021) concluded that the simulation tool is a useful method for analyzing many aspects of A-scan ultrasound and can be used to support the development of systems for cataract characterization.

3.4. Ultrasonic Probe Modeling

3.4.1. Model of an Experimental System as a LTI System

A system is an entity that responds to an input signal and generates an output signal from the interactions of the input signal with the system response (Haykin and Veen, 2002). A linear time-invariant (LTI) system is a class of systems that obeys the superposition principle, which means that when an input signal given by a linear combination of basic signals is applied to the system, the output is the combination of the individual responses of each input signal, considered separately. Also, they are called time-invariant since the output signal is independent of the instant the input signal is applied (Oppenheim and Willsky, 1996). The behavior of a LTI system is characterized by its impulse response ($h(t)$), which is defined as the output of an LTI system when a unit impulse is applied at the input, at time t = 0 (Haykin and Veen, 2002).

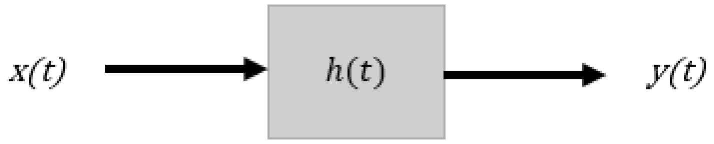

Figure 3.7. Representation of a LTI system with impulse response $h(t)$.

The output of an LTI system with impulse response $h(t)$ in response to an input $x(t)$ is given by the convolution integral of the two continuous-time signals, as represented in equation 3.1 (Haykin and Veen, 2002; Oppenheim and Willsky, 1996).

$$\begin{aligned} y(t) &= \int_{-\infty}^{+\infty} x(\tau)h(t-\tau)d\tau \\ &= h(t) * x(t) \end{aligned} \tag{3.1}$$

However, it is easier to work in the frequency domain, where the process of deconvolution is simpler, since the convolution in the time domain corresponds to multiplication of the Fourier Transform (FT) in the frequency domain. The convolution theorem is then given by equation 3.2, where $X(\omega)$, $\mathrm{H}(\omega)$ and $Y(\omega)$ are the Fourier transforms of $x(t)$, $h(t)$ and $y(t)$, respectively (Oppenheim and Willsky, 1996).

$$y(t) = h(t) * x(t) \leftrightarrow Y(\omega) = H(\omega) \cdot X(\omega) \tag{3.2}$$

Therefore, the transfer function $H(\omega)$ also characterizes the LTI system and is determined by the next expression:

$$H(\omega) = \frac{Y(\omega)}{X(\omega)} \tag{3.3}$$

To represent the ultrasonic probe like a LTI system, diverse system components like the signal generator, a transducer operating in pulse-echo mode, a coupling medium (water), the propagating medium, and an oscilloscope should be considered. For a probe working in pulse-echo mode, it is first excited by an electrical signal produced by the generator; the probe transforms it into an ultrasonic wave that propagates through the medium and returns to the transducer surface; the transducer transforms the ultrasonic wave again into an electrical signal. The resulting electric signal is displayed in the oscilloscope. It was proposed that this system can be modeled as a LTI system (Santos, 1994), where each component can be modeled as an individual LTI system connected in series. The linearity property of a LTI system and the convolution theorem enable the calculation of the total response of the system by superposition of the individual responses through multiple products in the frequency domain. The total frequency response is presented in equation 3.4, where Y is the output signal, X is the excitation pulse from the generator (input signal), and all the elements of the system are represented by their transfer functions: C_1 and C_2 represent the electric cables and connectors, H_1 and H_2 correspond to the transducer, W_1 and W_2 represent the coupling medium (water), S is the transfer function of the sample, L corresponds to the amplifier and D represents the ADC.

$$Y(w) = X(w)C_1(w)H_1(w)W_1(w)S(w)W_2(w)H_2(w)C_2(w)L(w)D(w) \tag{3.4}$$

3.4.2. Equivalent Circuit of a Piezoelectric Transducer

Fa et al. (2018) proposed a model for piezoelectric transducers based on the Fourier transform and the principle of linear superposition. The model consists of a parallel-connected equivalent-circuit network. A piezoelectric spherical thin-shell transducer was used to develop the model and some experimental measurements were made to verify the validity of the model.

In figure 3.8 are represented the electric-acoustic equivalent circuit, corresponding to the spherical shell transducer working as the source (a) and the acoustic-electric equivalent circuit representing the transducer defined as the receiver (b).

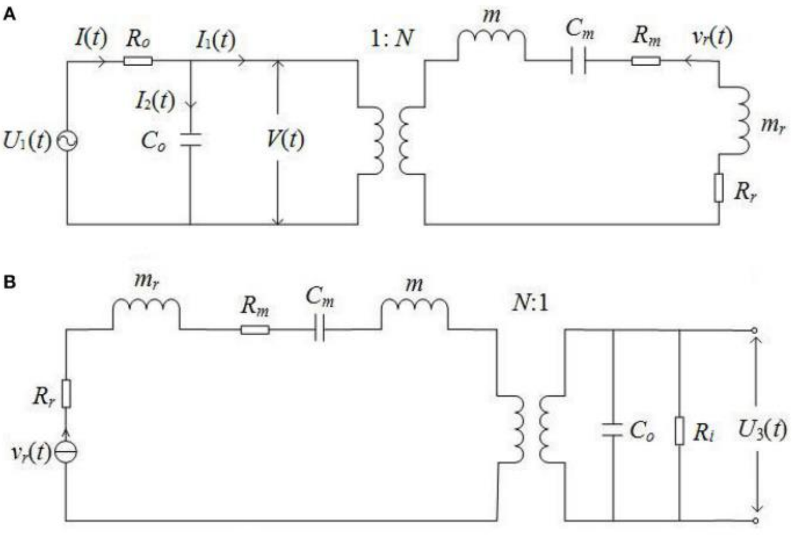

Figure 3.8. Equivalent electric circuits of a spherical-shell transducer. A) source, B) receiver. $U_1(t)$ is the voltage source, R_o is its output resistance, R_i is the input resistance of the measurement circuit; $V(t)$ is the voltage signal at electric terminals of the source; $U_3(t)$ is the electric signal at the electric terminals of the receiver; m_r is the radiation mass, R_r is the radiation resistance, C_m is the elastic stiffness, m is the mass, C_o is the clamped capacitance, N is the mechanical–electric conversion coefficient, and R_m is the fraction force resistance of transducer; and $v_r(t)$ is the vibration velocity at the transducer surface. Reproduced from (Fa et al, 2018).

There are two functions to determine: the first one ($H_1(s)$) is the electric-to-acoustic conversion function, given by the ratio of the vibration velocity at the surface of the shell transducer ($v_r(s)$) and the driving voltage ($U_1(s)$) (equation 3.5, figure 3.8A), while the second ($H_2(s)$) is the acoustic-to-electric conversion function, determined as the ratio of the electric-voltage signal at the electric terminals of the transducer ($U_3(s)$) and the vibration velocity at its mechanical terminals caused by an acoustic pressure at the surface of the transducer ($p(s)$) (equation 3.6, figure 3.8B).

$$H_1(s) = \frac{v_r(s)}{U_1(s)} \tag{3.5}$$

$$H_2(s) = \frac{U_3(s)}{p(s)} \tag{3.6}$$

Fa et al. (2018) concluded that the two transfer functions are similar since they have the same poles and only differ in a constant factor. Therefore, the electric-to-acoustic conversion property of the transducer is reciprocal to its acoustic-to-electric conversion property. The authors demonstrated that the results for the suggested model are in good agreement with experimental observation.

The experimental tests performed included two spherical shin-shell transducers, one used as an emitter and the other as a receiver, both immersed in water. It was also considered that the water only introduced attenuation (Fa et al., 2018).

3.4.3. Gamma-Tone Model

Due to its similarity to the received echo signal, the gamma-tone function can be used for received echo signal modeling. A gamma-tone is the product of a gamma distribution with a sinusoidal tone, and it can be modeled by the expression presented in equation 3.7.

$$y_g(t) = c\, t^{n-1} e^{-\beta t} cos(\omega_0 t + \phi) \tag{3.7}$$

This is a five-parameter model, where c is the proportionality constant (gain), n is the system order and controls the shape of the envelope, β is the decay temporal coefficient, ω_0 defines the dominant frequency and ϕ represents the phase (Darling, 1991).

The echo signal amplitude is modulated with an envelope that is proportional to $t^{n-1}e^{-\beta t}$, which is the same functional form as the gamma distribution (Darling, 1991). The frequency response of the gamma-tone is derived to see what the corresponding effects of the gamma-tone function parameters are in the frequency domain. Therefore, it is convenient to rewrite:

$$y_g(t) \ = \ c\, t^{n-1} e^{-\beta t} cos(\omega_0 t + \phi) u(t) \tag{3.8}$$

where $u(t)$ is the step function (Darling, 1991).

The envelope of the gamma-tone signal is then given by:

$$r(t) \ = \ c\, t^{n-1} e^{-\beta t}\, u(t) \tag{3.9}$$

Equation 3.9 also corresponds to a gamma distribution[3], as it was referred to before. The mode (t_m) of the distribution is defined as the most frequent value, and it is also given by $t_m = \frac{n-1}{\beta}$. The mean value (μ) of the distribution is given by the expression $\mu = \frac{n}{\beta}$. Once the mode and mean values are determined from the envelope of the gamma-tone signal, these expressions enable the calculation of parameters n and β.

The value of c can be obtained from the maximum of $r(t_m) \ = \ c\, {t_m}^{n-1} e^{-\beta t_m}$, while ω_0 and ϕ values are determined from the FT of the gamma-tone signal, which is given by equation 3.10 (Abramowitz and Stegun, 1964; Darling, 1991).

$$Y_g(j\omega) \ = c\, \frac{\Gamma(n)}{2} \left[\frac{e^{j\phi}}{(\beta + j(\omega \ - \ \omega_0))^n} + \frac{e^{-j\phi}}{(\beta + j(\omega + \omega_0))^n} \right] \tag{3.10}$$

Where $\Gamma(n)$ represents the Gamma function[4]. The magnitude of this function exhibits a peak near ω_0 and ϕ is the corresponding phase at frequency ω_0.

---

[3] https://en.wikipedia.org/wiki/Gamma_distribution

[4] https://en.wikipedia.org/wiki/Gamma_function

4. Ultrasonic Signals Simulation

This chapter describes the simulation of ultrasound waves propagating through healthy eyes. Firstly, the k-Wave toolbox is described, which was the method adopted to perform 2D and 3D simulations. Then the results regarding 2D preliminary tests and the transition to 3D simulation are obtained and discussed.

4.1. Simulation with the k-Wave Toolbox

The k-Wave MATLAB toolbox is a tool developed for the time-domain simulation of propagating acoustic waves in 1D, 2D, or 3D. The simulation functions in k-Wave solve a system of coupled first-order partial differential equations that describe the changes that take place on a compressible medium when an acoustic wave travels through it, using a numerical method called the k-space pseudospectral method. When the waves reach the edge of the domain, they disappear and are not reflected into the medium. This is possible due to a thin absorbing layer that encompasses the computational domain and provides absorption, called the perfectly matched layer (PML). By default, the k-Wave toolbox defines the size of the PML as 20 grid points for 1D and 2D simulations and 10 grid points for 3D simulations, where a grid point corresponds to a discrete position in space.

There are three simulation functions in k-Wave: `kspaceFirstOrder1D`, `kspaceFirstOrder2D`, and `kspaceFirstOrder3D`, for one, two, and three dimensions, respectively. These functions are called with four input structures: `kgrid`, `medium`, `source,` and `sensor`.

The first structure, `kgrid`, defines the properties of the computational grid and it is created using the function `makeGrid`, which takes the number of grid points (`Nx`, `Ny`, and `Nz`) and the grid point spacing (`dx`, `dy`, and `dz`), grouped in pairs for each Cartesian direction, as inputs, as it is represented below for 2D and 3D, respectively. This function returns a `kWaveGrid` object containing the properties of the computational grid used by the k-Wave functions during the simulation.

2D: `kgrid = makeGrid(Nx, dx, Ny, dy)`

3D: `kgrid = makeGrid(Nx, dx, Ny, dy, Nz, dz)`

To choose the appropriate number of grid points there should be considered that the execution time (i.e. the time that the computer takes to run the simulation routine) can be minimized if the grid points in each direction, including the PML, are a power of two or have a small prime factor.

The function `makeTime` enables the calculation of the `kgrid.t_array` parameter that defines the time values over which the simulation is run. To do that, given a certain time for the total simulated time (`t_end`), this function defines the appropriate time step (`kgrid.dt`) based on the Courant-Friedrichs-Lewy (CFL) number and the maximum sound speed in the medium (`medium.sound_speed`), as it is demonstrated below. The CFL number is defined as the ratio of the distance a wave can travel in one time step and the grid spacing and is equal to 0.3 by default.

```
kgrid.t_array = makeTime(kgrid, medium.sound_speed, CFL, t_end)
```

The second argument of the simulation function is `medium`, which contains the properties of the medium at each grid point. These properties include the sound speed (`medium.sound_speed`), the mass density (`medium.density`), the power law absorption coefficient (`medium.alpha_coeff`), and the power law absorption exponent (`medium.alpha_power`). In the context of this project, the medium is heterogeneous and therefore these parameters are defined as matrices of the same size as the computational grid.

The third input of the simulation function is `source` and it defines which grid points within the computational grid work as the source of the ultrasonic waves (i.e. the source profile). The type of source that is considered in this work is a time-varying pressure source. To define the source, it is required a source mask (`source.p_mask`) which is a binary matrix with the same size as the computational grid. Then a time-varying pressure input signal (`source.p`) is applied to each of the points in the mask.

All the signals in this chapter were simulated using an excitation pulse of 180 kPa (`strength`), 3 sinusoidal cycles (`cycles`), and a central frequency of 20 MHz (`f`). The `toneBurst` function was used for the generation of this signal, as demonstrated below, where the sampling frequency (`fs`) corresponds to the inverse of the time step (`kgrid.dt`). The excitation pulse is represented in figure 4.1.

```
source.p = strength.*toneBurst(fs,f,cycles)
```

Finally, the argument `sensor` defines the location of the sensor points that should record the acoustic pressure at each time step during the simulation. In the case of a probe working in pulse-echo mode, the sensor points are the same as the source points and therefore the mask that defines the sensor points (`sensor_mask`) constitutes the same binary matrix as `source.p_mask`. When running simulations, the values of the acoustic pressure measured at each point of the sensor mask are ordered in a column-wise mode and returned after the simulation is complete.

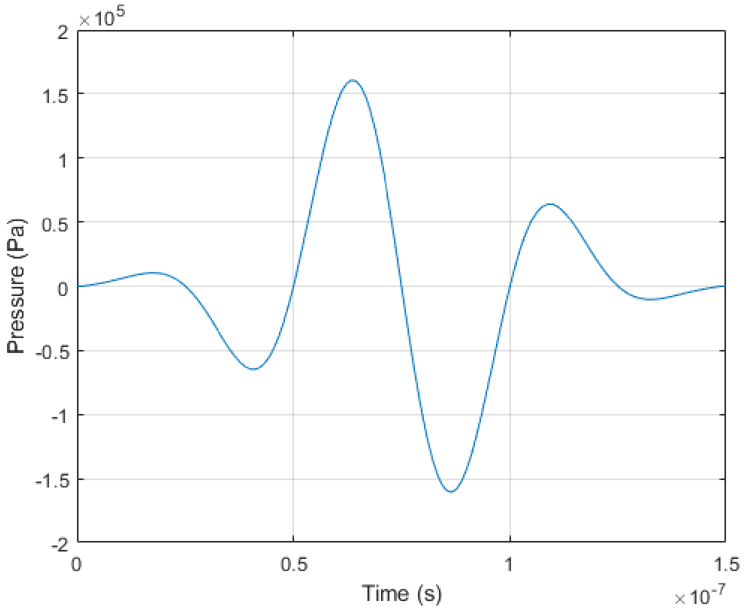

Figure 4.1. Excitation pulse used in the simulations, consisting of a burst of 180 kPa, 3 cycles and central frequency 20 MHz.

Simulations using large grid sizes may result in execution (computational) times that reach tens of hours. To reduce the execution times, k-Wave includes two optimized versions of `kspaceFirstOrder3D` to run optimized code for Central Processing Unit (CPU) and Graphics Processing Unit (GPU): `kspaceFirstOrder3D-OMP` and `kspaceFirstOrder3D-CUDA`. The latter is written using CUDA for NVIDIA GPUs and will be used in the scope of this project. The corresponding 2D functions are also available. Therefore, it is possible to run optimized CPU and GPU code from MATLAB for 2D and 3D simulation by calling functions `kspaceFirstOrder3DC` (CPU code) or `kspaceFirstOrder3DG` (GPU code), respectively (Treeby et al, 2016).

4.2. Preliminary Tests

The starting point of this project was based on the simulations described in Petrella et al. (2021). Here, it was used the eye matrix represented in figure 3.4, where the probe profile is also included. The simulation is performed with the probe coupled to the cornea (contact biometry) since the eyelid is excluded. Since the radius of curvature of the probe and the cornea are slightly different, the space between them is filled with water. The contact between the probe and the eye generates pressure in the cornea, causing its flattening. However, this phenomenon was not included in the simulations.

The dimensions and acoustic properties of the eye matrix are represented in tables 4.1 and 4.2, respectively. The value for the power law absorption exponent corresponding to soft tissues (`medium.alpha_power` = 1.2) was adopted.

Table 4.1. Radius of curvature and thickness of the interfaces represented in the eye matrix. Retrieved from (Petrella et al., 2021).

Interface	Radius (mm)	Thickness (mm)
Cornea	7.259	0.449
Aqueous humor	5.585	2.794
Lens	8.672	4.979
Vitreous humor	6.328	1.000
Retina	10.800	0.100
Choroid	10.800	0.175
Sclera	10.975	0.500
Back of the eye	11.475	0.100

Table 4.2. Acoustic properties of the eye structures that compose the eye matrix, retrieved from (Petrella et al, 2021), [a] Adapted from (Huang et al, 2007b).

Eye structure	Sound speed (m s^{-1})	Density (kg m^{-3})	Attenuation Coefficient (dB cm^{-1} MHz^{-1})
Water	1494	997	0.0022
Cornea	1553	1024	0.78
Aqueous humor	1495	1007	0.003
Lens	1649[a]	1090	0.42
Vitreous humor	1506	1003	0.0022
Iris	1575	1055	0.60
Retina	1538	1008	1.15
Choroid	1527	1002	0.95
Sclera	1583	1049	0.97
Periorbital Fat	1465	985	0.40
Eyelid	1615	1090	2.30

The result of the simulation using the matrix of figure 3.4 and the input signal in figure 4.1 is the A-scan in figure 4.2.

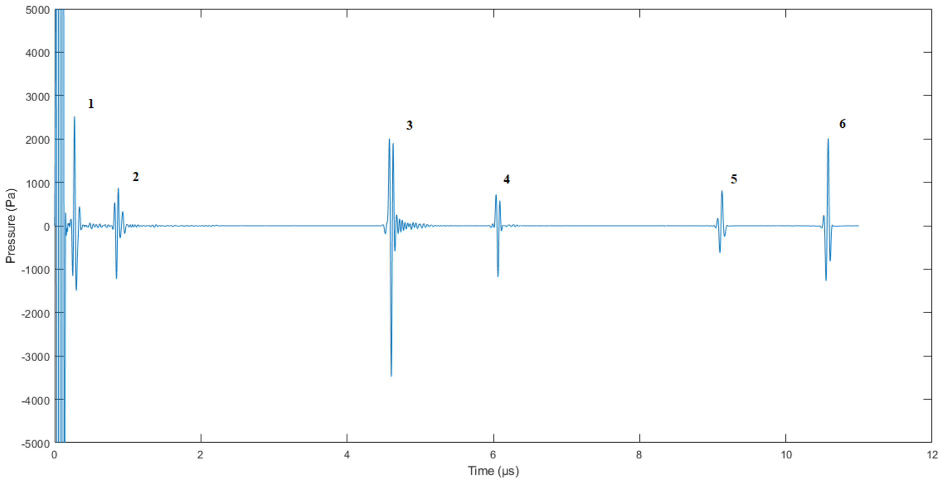

Figure 4.2. Simulated A-scan considering a healthy lens. The echoes reflected in the interfaces of the eye are: 1) water/ cornea, 2) cornea/ aqueous humor, 3) aqueous humor/ lens, 4) lens cortex/ nucleus, 5) lens nucleus/ cortex, 6) lens/ vitreous humor. The total simulated time is 11 μs to include the wave propagation through the cornea, aqueous humor, and lens.

4.2.1. Minimum Height of the Eye Matrix

Since it is simulated a focalized ultrasonic probe with 3.2 mm height, while the eye matrix from figure 3.4 has 25.0 mm height (2048 grid points) and 26.7 mm wide (2187 grid points), it is expectable no substantial contribution to the simulated signals from the eye structures localized at top and bottom of the matrix. Therefore, the possibility to reduce the number of grid points `Nx` (the grid height) of the matrix to save memory and computational time was analyzed. Firstly, different signals from matrices with different `Nx` were simulated, starting with the minimal size, which corresponds to the probe height, as it is illustrated in figure 4.3, until the full grid size.

Using the same matrix resolution as Petrella et al. (2021) of 12 μm, the probe profile corresponds to 263 grid points high. However, this number cannot be the minimal grid height since the PML should be considered, which is, by default, 20 pixels all around the matrix. This means that the minimum `Nx` should be 263 + 40 = 303. Then, to find the number of pixels with a small prime factor (for reducing computational time), the minimum `Nx` became 320 pixels. Then, successive simulations were performed increasing the `Nx` until its maximum (`Nx`=2048).

For this assessment, the selected simulated time (i.e. the time over which the simulation is run) was 1.5×10^{-5} seconds (15 µs) to include the wave propagation from the probe until some grid points behind the lens.

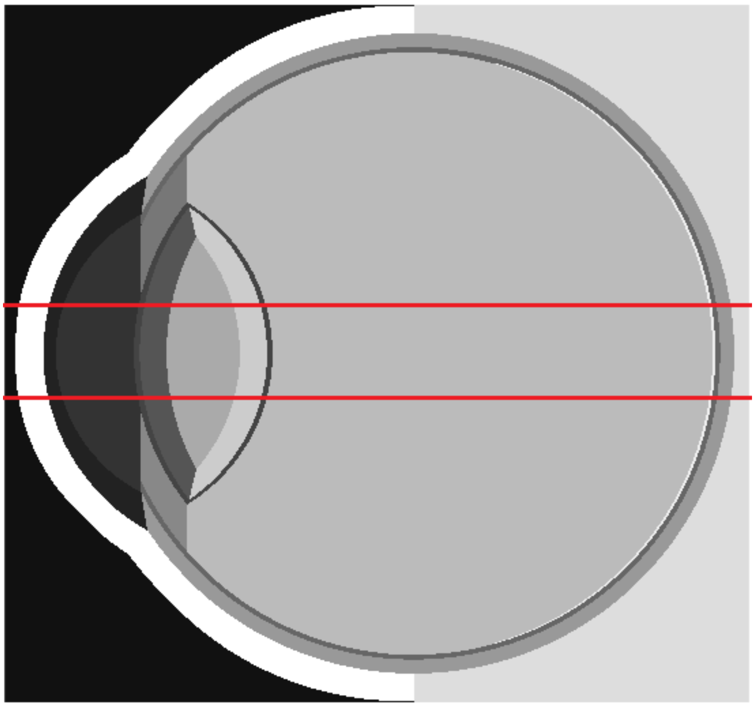

Figure 4.3. Eye grid with the minimum height based on the source/sensor profile delimited by two red lines. Adapted from (Petrella et al, 2021).

These simulations were performed with an optimized GPU code which considerably reduces the execution time (approximately 50 times), and using a GeForce GTX 1080 Ti board, which has a memory size of 11 GB.

For the minimum `Nx` (`Nx`=320 and `Ny`=2187) the execution time was 8.77 s, while for the full eye profile (`Nx`=2048 and `Ny`=2187) it was around 48.13 s. For evaluating the effect of the grid height in the simulated signals, the echoes resulting from the reflections in the interfaces aqueous humor/lens and lens/vitreous humor were isolated, and the maximum peak amplitude was measured and compared to the ones from the full matrix. The results are presented in table 4.3.

The pulse duration of the echo from the anterior lens interface was also considered. To determine this parameter, the Hilbert transform was implemented to obtain the signal envelope, and then the pulse width was determined as the excursion time above a threshold of 10% of its peak ($\Delta t = t_2 - t_1$) (figure 4.4). The results are presented in table 4.4 as a percentage of the pulse duration using the full grid.

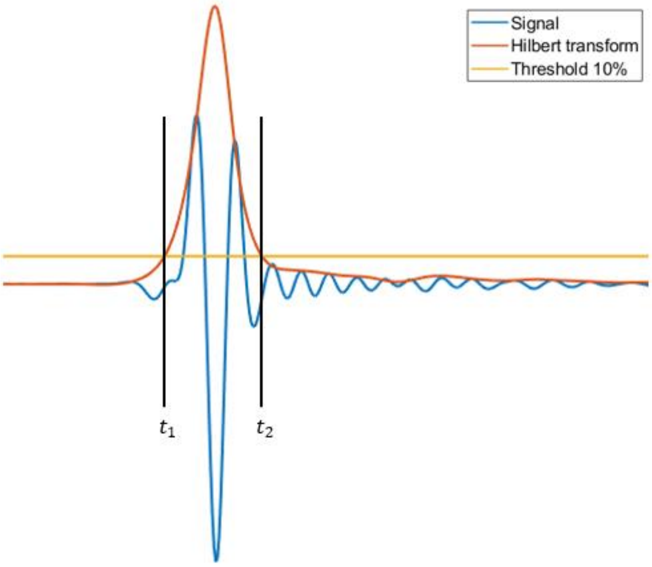

Figure 4.4. Calculation of the pulse duration (Δt).

Table 4.3. Maximum pressure of the echoes of the anterior and posterior lens interfaces, for matrices with different grid heights at a resolution of 12 µm; the ratio between the pressure for each `Nx` with the pressure of the full matrix (`Nx`=2048); and the corresponding execution times.

`Nx`	Height (mm)	Maximum pressure anterior lens (Mp1) (Pa)	Maximum pressure posterior lens (Mp2) (Pa)	$\frac{\text{Mp1}}{\text{Mp1}_{Nx=2048}} \times 100$	$\frac{\text{Mp2}}{\text{Mp2}_{Nx=2048}} \times 100$	Execution time (s)
320	3.80	3.479×10^3	2.014×10^3	100.05%	99,94%	8.77
324	3.90	3.479×10^3	2.014×10^3	100.05%	99,94%	9.21
420	5.00	3.479×10^3	2.015×10^3	100.04%	99,97%	11.63
512	6.10	3.479×10^3	2.016×10^3	100.04%	100,01%	12.90
864	10.44	3.479×10^3	2.016×10^3	100.04%	100,02%	21.96
1024	12.30	3.479×10^3	2.016×10^3	100.04%	100,02%	24.89
2000	24.00	3.479×10^3	2.016×10^3	100.04%	100,02%	48.69
2048	24.60	3.478×10^3	2.015×10^3	100.00%	100,00%	48.13

Table 4.4. Pulse duration of the echo from the anterior lens interfaces, for different values of `Nx` and the corresponding execution times.

`Nx`	Height (mm)	t_1 (µs)	t_2 (µs)	Pulse duration (Δt) (µs)	$\frac{\Delta t}{\Delta t_{Nx=2048}} \times 100$	Execution time (s)
320	3.80	4.536	4.665	0.129	100.78%	8.77
324	3.90	4.536	4.665	0.129	100.78%	9.21
420	5.00	4.536	4.665	0.129	100.78%	11.63
512	6.10	4.536	4.665	0.129	100.78%	12.90
864	10.44	4.536	4.665	0.129	100.78%	21.96
1024	12.30	4.536	4.665	0.129	100.78%	24.89
2000	24.00	4.536	4.665	0.129	100.78%	48.69
2048	24.60	4.536	4.664	0.128	100.00%	48.13

Considering these results, it was concluded that the difference in amplitude and pulse duration are not significative when there is a variation in the grid height (within the considered range). Therefore, the following steps consider a matrix with the minimum `Nx`, as the execution time decreases almost 6 times compared to the simulation with the full eye profile.

Moreover, since the region of interest is the crystalline lens, it was reduced the matrix width (`Ny`) to 9.20 mm (768 grid points with a pixel size of 12 µm), which includes a few pixels after the posterior interface of the lens. This new eye matrix is illustrated in figure 4.5.

Figure 4.5. 2D eye matrix with a resolution of 12 µm. Components: water (black), cornea (blue), aqueous humor (green), lens (orange), and vitreous humor (red).

This matrix was constructed using the k-Wave function `makeArc` which enables the design of an arc given the computational grid size (`[Nx, Ny]`), the position of its midpoint (`[ax, ay]`) the radius of curvature (`radius`), the aperture diameter (`diameter`), and the focal point (`[fx, fy]`), as it is showed below:

```
Arc = makeArc([Nx, Ny], [ax, ay], radius, diameter, [fx,fy])
```

In real crystalline lenses, the nuclear and cortical regions are not well-delimited as indicated in the eye grid from the previous work. Therefore, a homogeneous lens was implemented from this point forward. The result of a simulation with this matrix and the same input signal previously described is the A-scan represented in figure 4.6, using a total simulated time of 11 μs.

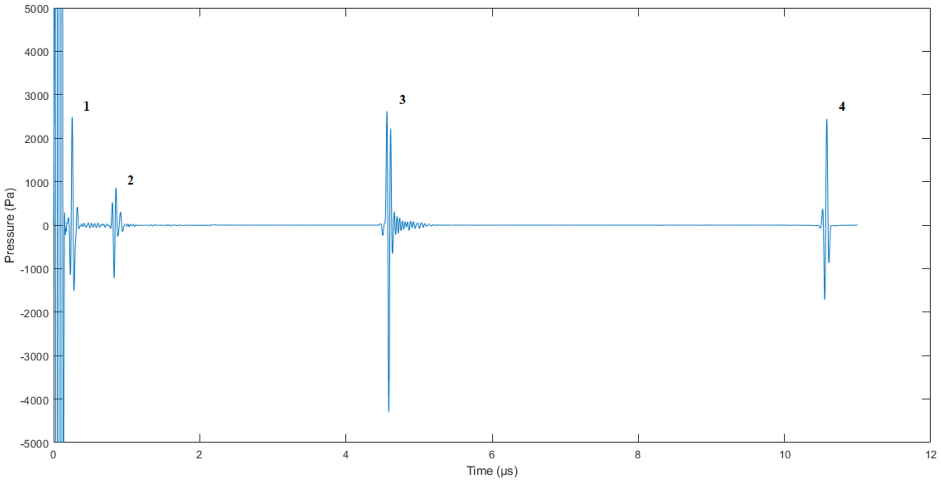

Figure 4.6. Simulated signal with constrained grid size. The echoes reflected in the eye interfaces are: 1) water/cornea, 2) cornea/aqueous humor, 3) aqueous humor/lens, 4) lens/vitreous humor.

4.3. Resolution Analysis

To obtain a more realistic representation of the microscopic cataract structures for 2D and 3D simulations, a higher resolution is required. Therefore, the matrix of figure 4.5 was altered to present different pixel sizes and therefore determine the maximum resolution that can be simulated, considering the computational resources available. Table 4.5 shows the obtained results.

With optimized GPU code it is possible to simulate a 2D matrix with a pixel size of approximately 0.64 μm, 19 times smaller than the one used in Petrella et al. (2021). However, since with 3D simulations the required computational resources increase exponentially, the minimum pixel size for 3D simulations should be addressed.

Table 4.5. Computational time of the 2D simulations using matrices with different pixel sizes.

Pixel size (µm)	`Nx`	`Ny`	Execution time (GPU) (s)
12.00	320	768	3.06
8.00	432	1080	6.59
6.00	640	1536	23.49
3.00	1280	3072	174.95
1.50	2560	6144	1726.69
1.00	3840	9216	4657.15
0.76	5120	12288	14123.45
0.68	5760	13824	19232.13
0.64	6080	14592	28447.94

4.4. 3D Eye Matrix

The goal is to generate a 3D matrix to run 3D simulations and compare the simulated signals with the ones resulting from the 2D simulations in the same conditions. The 3D simulations should be a better approximation to reality, however, the computational resources and time are significantly higher than 2D simulations.

The 3D matrix was constructed with the same characteristics as the 2D matrix, using specific k-Wave functions. A cut through the sagittal plane of the generated 3D matrix corresponds to the matrix illustrated in figure 4.5.

A 3D matrix with a pixel size of 12 µm and dimensions of 320 voxels height, 768 voxels wide, and 320 voxels deep (3.80 mm height, 9.20 mm wide, and 3.80 mm deep) was generated. However, a matrix with these dimensions required more memory than the available computational resources. Therefore, the pixel size was increased to 24 µm, corresponding to 160 voxels in height, 384 voxels wide, and 160 voxels deep.

Simulations using 2D and 3D eye matrices with pixel/voxel size of 24 µm were performed using a simulated time of 15 µs. The simulated 2D and 3D signals are presented in figures 4.7 and 4.8, respectively.

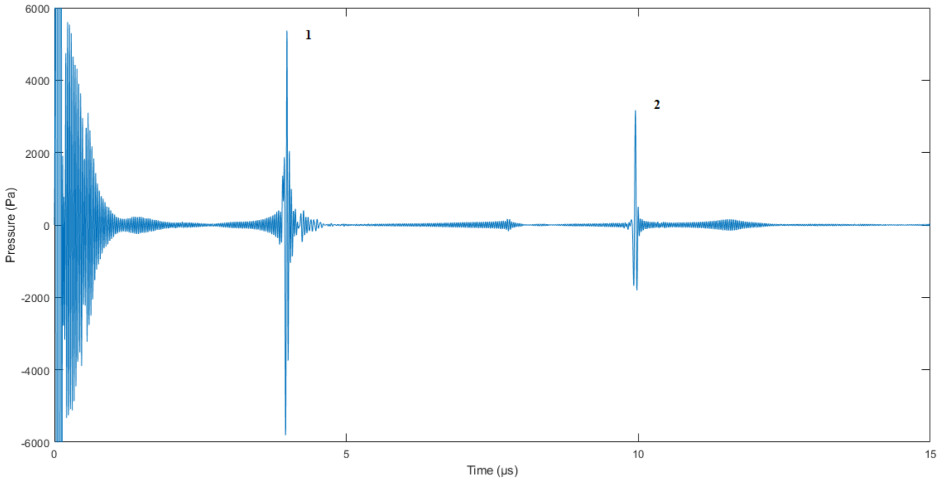

Figure 4.7. Simulation signal obtained with the 2D eye matrix with a resolution of 24 µm. 1) Echo from the anterior lens interface, 2) echo from the posterior lens interface.

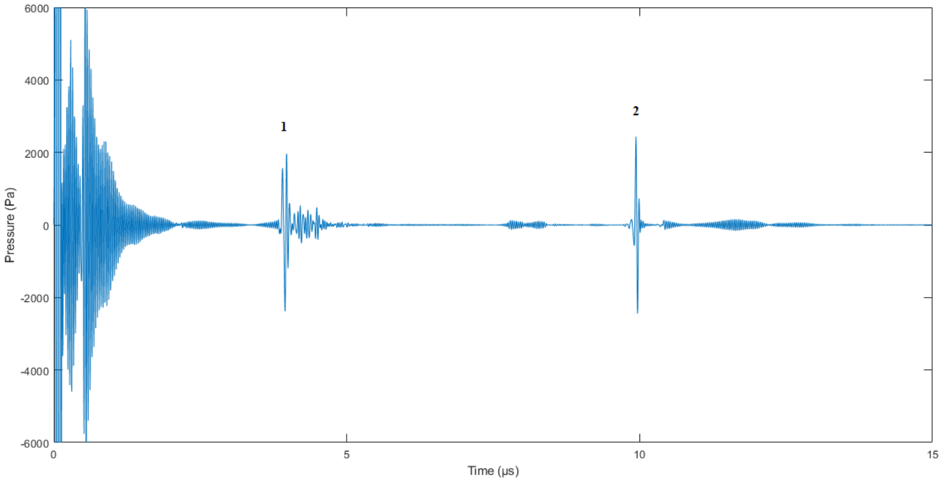

Figure 4.8. Simulated signal obtained with the 3D eye matrix with a resolution of 24 µm. 1) Echo from the anterior lens interface, 2) echo from the posterior lens interface.

The echoes from the lens interfaces are the high amplitude echoes present in the simulated signals (echoes 1 and 2 in figures 4.7 and 4.8). The smaller echoes observed before echoes 1 and 2 correspond to multiple reflections in the cornea interfaces.

The simulated signals were compared, using four features adapted from Caixinha et al. (2016b), to evaluate the differences in the echoes between the anterior and posterior lens interfaces:

- Maximum absolute amplitude of the signal;
- Maximum signal excursion (i.e. peak-to-peak amplitude);

- Maximum duration (Δt) of an excursion of the absolute amplitude above the threshold 80%;
- Maximum duration (Δt) of an excursion of the absolute amplitude above the threshold 10%.

The results are presented in tables 4.6 and 4.7.

Table 4.6. Results for the simulation with a 2D matrix with a resolution of 24 µm.

2D signal	Max amplitude (Pa)	Max excursion (Pa)	Δt 10% (µs)	Δt 80% (µs)	Execution time (s)
Anterior echo	5.81×10^3	1.12×10^4	0.220	0.050	1.21
Posterior echo	3.17×10^3	4.98×10^3	0.120	0.046	

Table 4.7. Results for the simulation with a 3D matrix with a resolution of 24 µm.

3D signal	Max amplitude (Pa)	Max excursion (Pa)	Δt 10% (µs)	Δt 80% (µs)	Execution time (s)
Anterior echo	2.38×10^3	4.34×10^3	0.669	0.063	101.59
Posterior echo	2.44×10^3	4.88×10^3	0.130	0.045	

These results showed considerable differences between the 2D and 3D simulated signals regarding the echo amplitudes and pulse durations. The next step was to investigate the influence of the curvature of the probe and the eye interfaces in the 2D and 3D simulations, to depict the cause of the observed differences.

4.4.1. Influence of the Curvature of the Probe and Interfaces

To determine the cause of the differences encountered in the last section, the effect of the interfaces curvatures in the reflected waves was investigated using three approaches on which these curvatures are modified. The matrix resolution, the characteristics of the ophthalmologic probe, the excitation pulse and the acoustic properties are as in previous simulations, except for the radius of curvature since this is the characteristic under study.

4.4.1.1. Plane Source/Sensor and Interfaces

The first test consists of the simulation of a plane source/sensor and two plane interfaces in the positions of the anterior and posterior lens interfaces, that delimit the region with the same characteristics as the lens. The remaining two regions have the acoustic properties of water.

Figure 4.9. Plane matrix with the probe profile, and plane anterior and posterior lens interfaces.

The matrix in figure 4.9 was simulated in 2D and 3D. In 2D, the probe is represented by a straight line, while in 3D it is a disc. The simulation results are presented in figures 4.10 and 4.11 and tables 4.8 and 4.9.

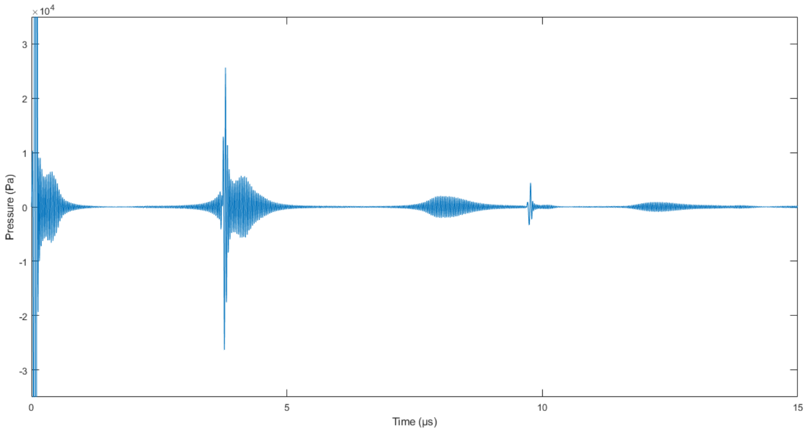

Figure 4.10. Simulation signal obtained with the 2D matrix with plane interfaces and source/sensor.

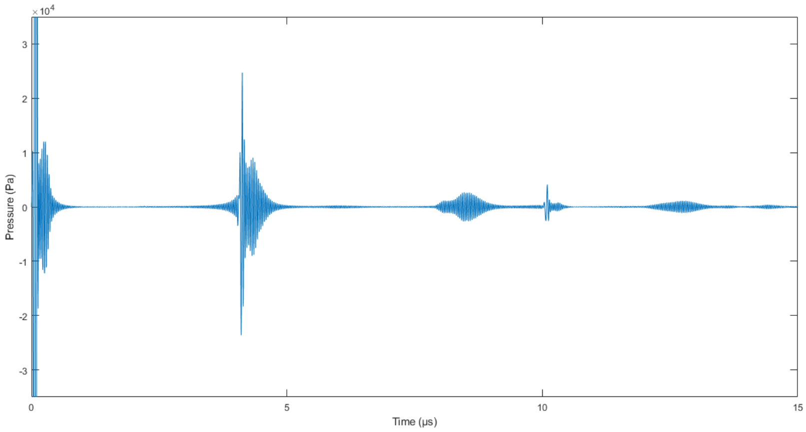

Figure 4.11. Simulation signal obtained with the 3D matrix with plane interfaces and source/sensor.

Table 4.8. Results for the simulation with a 2D matrix with plane interfaces and source/sensor.

2D signal	Max amplitude (Pa)	Max excursion (Pa)	Δt 10% (µs)	Δt 80% (µs)	Execution time (s)
Anterior echo	2.63×10^4	5.20×10^4	0.707	0.053	1.36
Posterior echo	4.43×10^3	7.78×10^3	0.133	0.045	

Table 4.9. Results for the simulation with a 3D matrix with plane interfaces and source/sensor.

3D signal	Max amplitude (Pa)	Max excursion (Pa)	Δt 10% (µs)	Δt 80% (µs)	Execution time (s)
Anterior echo	2.47×10^4	4.83×10^4	0.556	0.056	100.2
Posterior echo	4.11×10^3	6.69×10^3	0.370	0.050	

These results show a similarity between the two signals, although the 3D signal show slightly smaller amplitudes compared to the 2D signal.

4.4.1.2. Plane Interfaces and Curved Source/ Sensor

In this second test, the probe profile is defined according to its initial characteristics, but the lens interfaces are kept plane (figure 4.12). The simulation results are presented in figures 4.13 and 4.14 and tables 4.10 and 4.11.

Figure 4.12. Matrix with the curve profile of the probe and plane anterior and posterior interfaces.

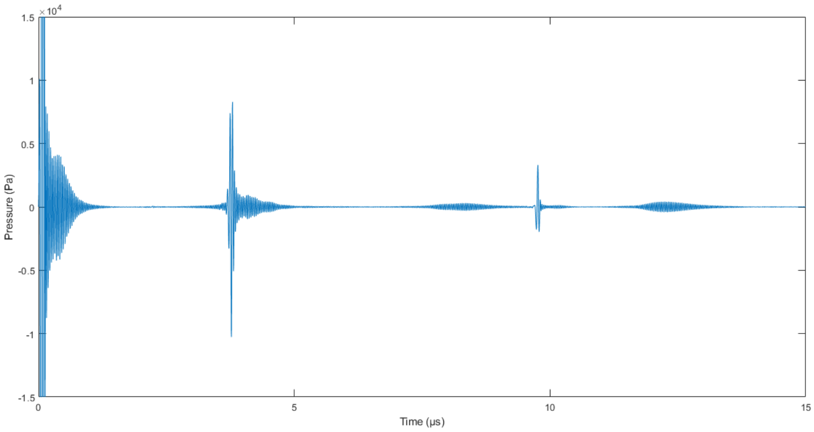

Figure 4.13. Simulation signal obtained with the 2D matrix with plane interfaces and curved source/sensor.

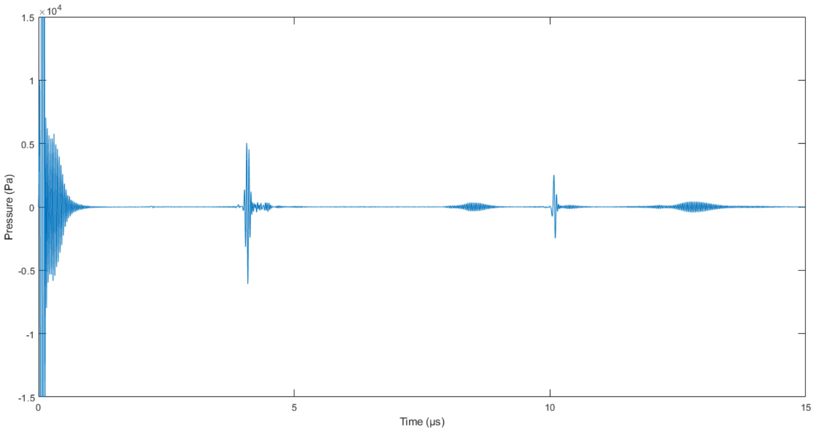

Figure 4.14. Simulation signal obtained with the 3D matrix with plane interfaces and curved source/sensor.

Table 4.10. Results for the simulation with a 2D matrix with plane interfaces and curved source/sensor.

2D signal	Max amplitude (Pa)	Max excursion (Pa)	Δt 10% (μs)	Δt 80% (μs)	Execution time (s)
Anterior echo	1.03×10^{4}	1.86×10^{4}	0.236	0.047	1.21
Posterior echo	3.31×10^{3}	5.27×10^{3}	0.120	0.045	

Table 4.11. Results for the simulation with a 3D matrix with plane interfaces and curved source/sensor.

3D signal	Max amplitude (Pa)	Max excursion (Pa)	Δt 10% (μs)	Δt 80% (μs)	Execution time (s)
Anterior echo	6.07×10^{3}	1.11×10^{4}	0.158	0.051	100.1
Posterior echo	2.53×10^{3}	5.02×10^{3}	0.179	0.060	

The results show a moderated difference between the 2D and 3D simulations when compared to the previous test, although these differences are still acceptable.

4.4.1.3. Curved Probe and Interfaces

The last simulation includes the same probe and lens profile as described in section 4.2, but in this matrix only the lens interfaces are represented (without the remaining eye structures).

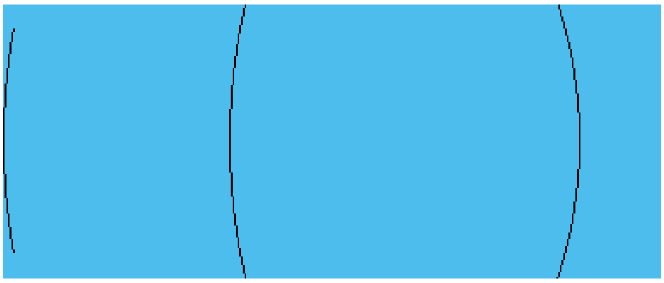

Figure 4.15. Matrix with anterior and posterior lens interfaces and the probe profile.

The simulation matrix is illustrated in figure 4.15, and the results are presented in figures 4.16 and 4.17 and tables 4.12 and 4.13.

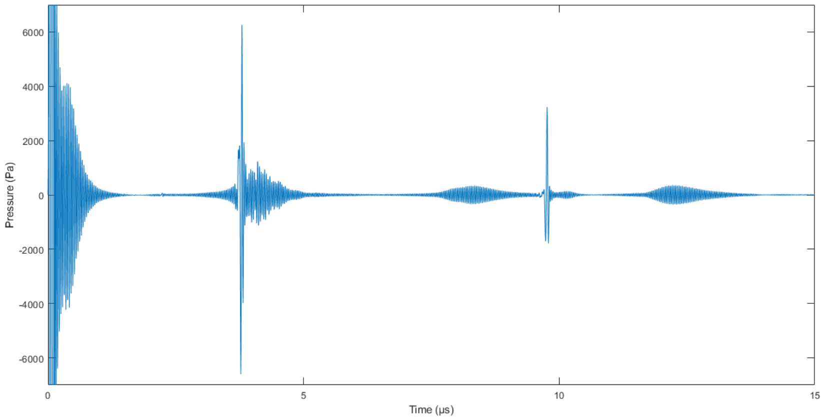

Figure 4.16. Simulation signal obtained with the 2D matrix with curved interfaces and source/sensor.

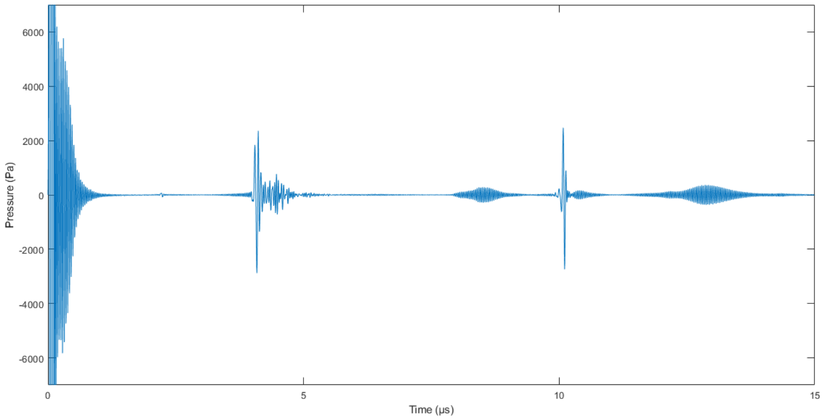

Figure 4.17. Simulation signal obtained with the 3D matrix with curved interfaces and source/sensor.

Table 4.12. Results for the simulation with a 2D matrix with curved interfaces and source/sensor.

2D signal	Max amplitude (Pa)	Max excursion (Pa)	Δt 10% (μs)	Δt 80% (μs)	Execution time (s)
Anterior echo	6.60×10^3	1.29×10^4	0.626	0.049	1.18
Posterior echo	3.23×10^3	5.01×10^3	0.109	0.040	

Table 4.13. Results for the simulation with a 3D matrix with curved interfaces and source/sensor.

3D signal	Max amplitude (Pa)	Max excursion (Pa)	Δt 10% (μs)	Δt 80% (μs)	Execution time (s)
Anterior echo	2.88×10^3	5.24×10^3	0.275	0.049	100.2
Posterior echo	2.74×10^3	5.21×10^3	0.130	0.045	

This last simulated matrix is closer to the original eye model. The 3D simulation results present significative differences when compared to the previous 3D simulations using plane interfaces, as well as with the corresponding 2D simulation result. These differences corroborate the influence of the curvatures of the probe and interfaces in the resulting A-scans, particularly noticeable in the 3D case. Since the 3D matrix is a more accurate approximation to reality, the 3D simulation should be adopted, and its result compared with real signals.

4.5. Simulation Step by Step

To represent the incipient cataract as micrometrical structures, a small pixel size is required. However, a decrease in pixel size causes a rise in memory and computational time, which is particularly substantial in the case of 3D simulation. It was investigated the possibility of performing the simulation in three phases. The proposal is to implement the simulation inside the lens with a smaller pixel size to be able for representing the structures related to cataract with a resolution of a few micrometers, while the rest of the matrix may remain with a higher pixel size.

1. First simulation phase: propagation from source to anterior lens interface. In this first simulation, the probe will act as source and sensor (yellow line in figure 4.18), but additional sensor points are placed in the anterior lens interface (red line in figure 4.18), to record the pressure that arrives at the lens. The information from this last sensor is stored in a variable to be used in the next stage.

2. Second simulation phase: propagation inside the lens. In this stage, the source and the sensor points are placed in the anterior lens interface (red line in figure 4.18). The variable containing the pressure recorded in the previous simulation is used as the source input for this step. The simulated time was designed to include the simulation of the waves propagating through the whole lens and a few pixels of the vitreous humor, to record the total reflection in the posterior lens interface. The result of the simulation is a variable containing the information of the echo from the posterior lens interface, which is stored to use in the final phase.

3. Third simulation phase: propagation from the lens again to the probe (sensor). The pressure obtained in the last phase is the input signal of a source placed in the anterior lens interface (red line in figure 4.18). In this final stage, the anterior lens interface is the source, and the sensor is placed in the probe (yellow line in figure 4.18).

After these phases, the simulated signal is the result of the combination of the pressure signals collected by the probe: the information regarding the cornea and the aqueous humor is given in the first stage, as the rest is given in the final stage. The 3-phases simulation was performed using a uniform pixel size of 12 µm (figure 4.19). The result must then be similar to that obtained with a conventional (1-phase) simulation (figure 4.6) using the same resolution.

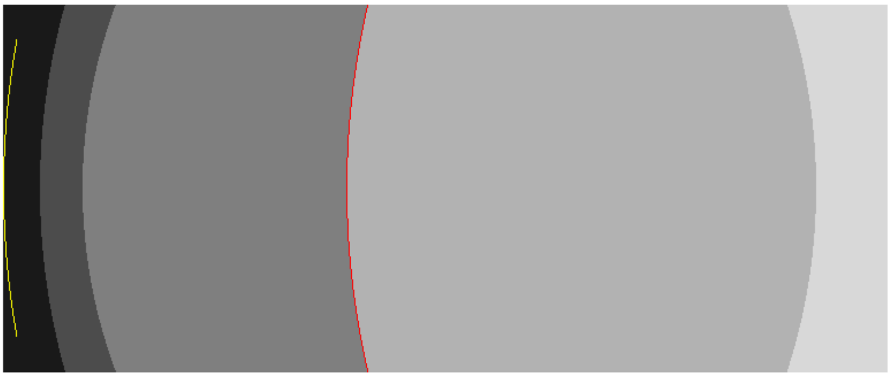

Figure 4.18. Matrix with source and sensor positioned on the probe (yellow) and the anterior lens interface (red).

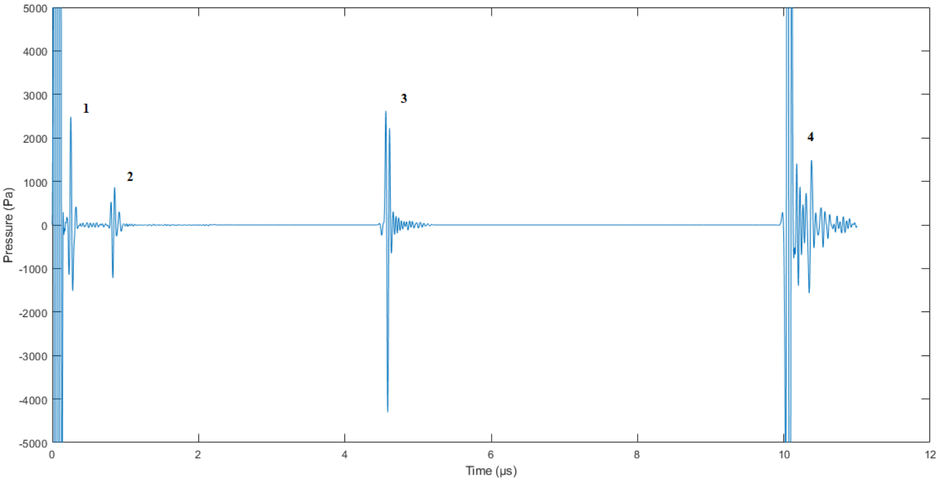

Figure 4.19. Reconstruction of the simulated signal resulting from the three phases of simulation. The echoes reflected in the eye interfaces are: 1) water/cornea, 2) cornea/aqueous humor, 3) aqueous humor/lens, 4) lens/vitreous humor.

After the comparison between the signals in figures 4.6 and 4.19, it is evidenced that the echo from the posterior lens interface in the 3-phases simulation has a higher amplitude than the corresponding in conventional simulation and does not occur at the same time. This may be due to interferences in the sensor in the second phase of the simulation.

Attempting to solve this problem, another approach was considered, where the sensor in the first simulation phase is positioned in the aqueous humor (red line in figure 4.20), instead of the anterior lens interface. Therefore, for the second stage of the simulation, a matrix containing the total lens and some pixels from the aqueous and vitreous humor was created. Every other aspect of the simulation remained the same as described before. In this case, the reconstruction is represented in figure 4.21.

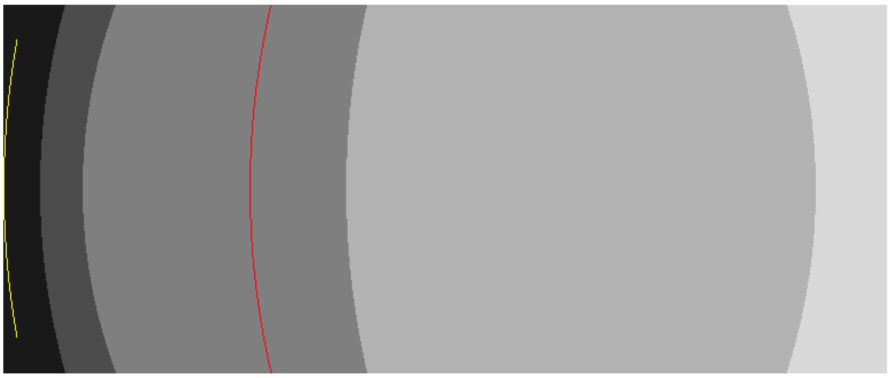

Figure 4.20. Matrix with source and sensor placed on the probe (yellow) and the aqueous humor (red).

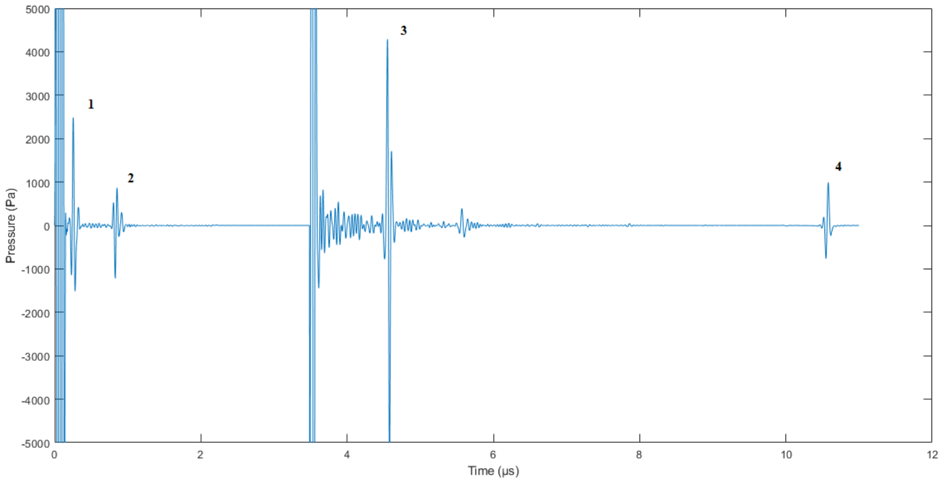

Figure 4.21. Reconstruction of the simulated signal resulting from the three stages of simulation, where the simulation was interrupted in the aqueous humor. The echoes reflected in the eye interfaces are: 1) water/ cornea, 2) cornea/ aqueous humor, 3) aqueous humor/ lens, 4) lens/ vitreous humor.

This result does not coincide with the signal in figure 4.6, and it is possible to conclude that this approach is not a successful way to perform simulations. The differences observed between figures 4.6 and 4.21 may be justified by multiple reflections between the sensor and the anterior lens interface that generate the interferences inside the lens observed in figure 4.21 and the reduction in the amplitude of the echo from the posterior lens interface.

After these two experiments, it is possible to conclude that the simulation in stages is not viable once it is not possible to avoid the interference generated by the multiple reflections in the anterior lens interface caused by the proximity of the sensor. Therefore, there should be determined a resolution that enables the simulation of the complete 3D matrix.

4.6. Improved Resolution

Meanwhile, a new GPU board NVIDIA GeForce RTX 3090 with a memory of 24 GB became available and allowed to conduct further tests for resolution improvement. The medium consisted of homogeneous matrices with the acoustic properties of water and with the minimum required dimensions described in section 4.2. It was also considered that the number of grid points results in a small prime factor. The results are presented in table 4.14.

Table 4.14. Computational time of the simulation of homogeneous 3D matrices, using GPU.

Pixel size (µm)	Nx	Ny	Nz	Execution time (s)
12	320	768	320	255.2
10	384	864	384	510.13
9	384	972	384	659.73
8	432	1080	432	1374.46

The matrix with a pixel size of 8 µm has 3.50 mm height, 8.60 mm wide and 3.50 mm deep, and took approximately 23 minutes to run. Smaller pixel sizes were not investigated due to the limitations of memory of the GPU board.

It was important to depict the microstructures related to cataract that will be simulated in the future, to verify if the attained resolution is suitable for its representation.

The characterization of cortical cataract (the most common type of cataract) includes two types of structures: Multilamellar bodies (MLBs) and Obazawa shades, consisting of radial and circular opacities. The typical dimensions of these structures are presented in table 4.15 (Vrensen and Willekens, 1990; Michael et al., 2008; Michael and Bron, 2011).

Table 4.15. Dimensions of the microstructures that compose the cortical cataract.

Structure	Minimum dimensions	Maximum dimensions
Multilamellar Bodies (MLBs)	Circles with a diameter of 8 µm	Circles with a diameter of 20 µm
Radial shades	Triangles with 192 µm base and 384 µm height	Triangles with 192 µm base and 435 µm height
Circular shades	Rectangles with 240 µm wide and 50 µm height	Rectangles with 500 µm wide and 50 µm height

Looking at the dimensions of the cataract structures for the developed model, the suggested resolution of 8 µm is suitable for the objective of this work and, therefore, it was the pixel size adopted. The correspondent matrix is represented in figure 4.22.

Figure 4.22. Central slide of the 3D eye matrix with a pixel size of 8 µm. Components: water (black), cornea (blue), aqueous humor (green), lens (orange), and vitreous humor (red).

Once the new resolution was established for the 3D simulation, the simulation was performed, and the simulated A-scan is represented in figure 4.23.

Since there are only a few pixels of water before the cornea in the matrix (figure 4.22), the echo of the interface water/cornea is not completely visible in these signals. However, the main goal is to evaluate the region corresponding to the lens.

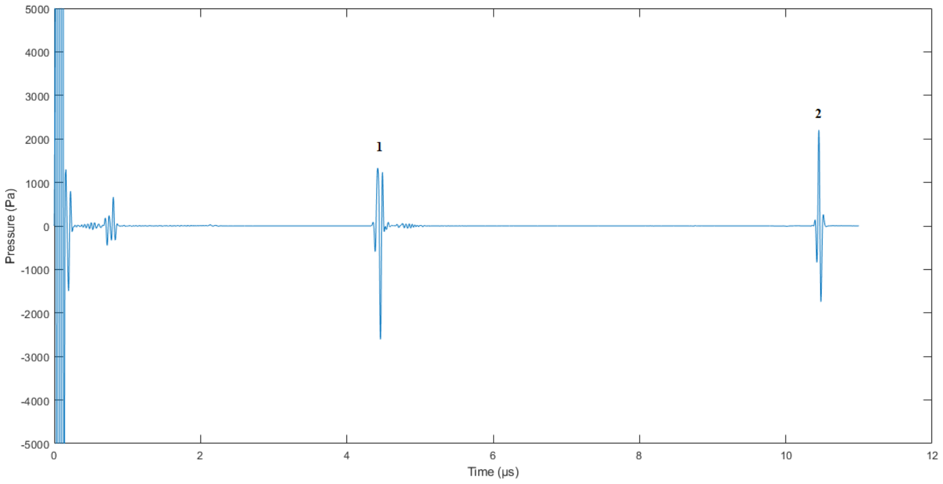

Figure 4.23. Simulation signal obtained with the 3D eye matrix with a resolution of 8 μm. 1) Echo from the anterior interface of the lens, 2) echo from the posterior interface of the lens.

4.6.1. Structures Inside the Lens

To evaluate if a small structure inside the lens would be detected at the chosen resolution (8 μm), three tests were carried out, in which some small structures were included in the eye matrix. Then, 3D simulations were performed. To these structures were attributed the acoustic properties of nuclear severe cataract according to Petrella et al (2021): velocity 1785 m/s, density 1200 kg/m^3 and attenuation coefficient 5.20 dB/cm MHz. The simulated time was 11 μs.

4.6.1.1. Single Structure with an Edge of 16 μm

The first matrix included a single cube with an edge of 2 grid points, placed in the midpoint of the lens. The central slice of the 3D matrix is presented in figure 4.24 and the resulting signals from the 3D simulation are shown in figure 4.25.

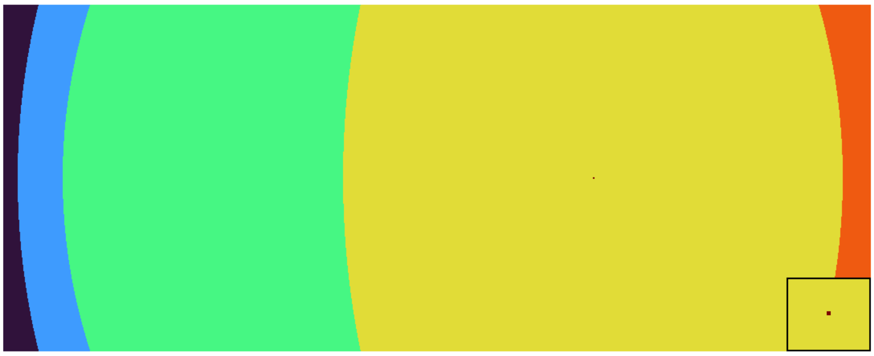

Figure 4.24. Eye matrix with a structure with an edge of 16 μm placed in the midpoint of the lens. In the bottom right corner there is a zoom of the structure (red dot).

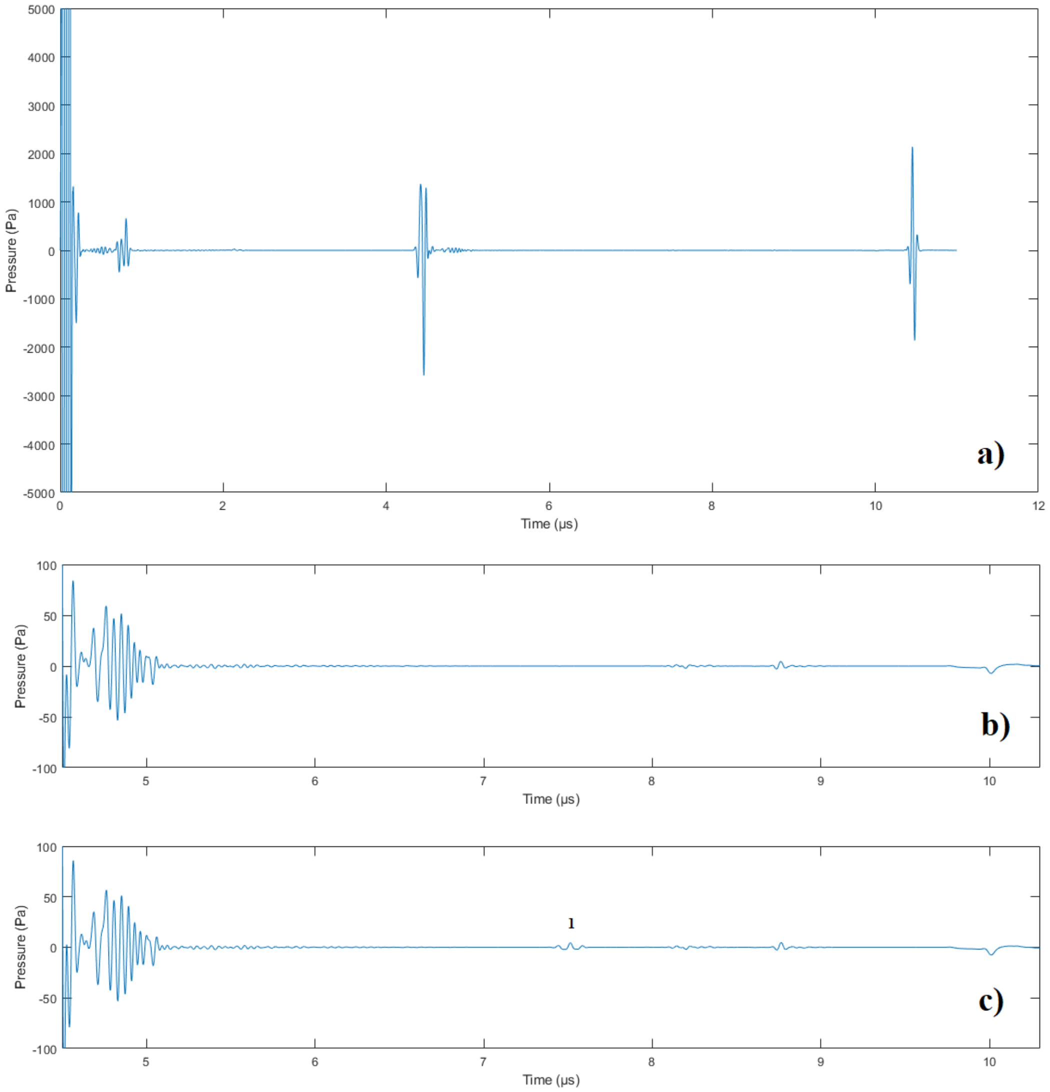

Figure 4.25. 3D simulated signal using an eye matrix resolution of 8 µm, with a structure in the middle of the lens, with 2 voxels side: a) complete 3D simulated signal, b) and c) zoom of the simulated signal corresponding to the lens thickness without (b) and with (c) the structure inside the lens. The scattering caused by this small structure is identified in the figure c) by the number 1.

Looking at the 3D simulated signal in figure 4.25, it is possible to observe that the scattering caused by the structure presents a substantially reduced amplitude when compared with the echo from the lens interfaces.

4.6.1.2. Structure with an edge of 80 µm

To explore the signal generated from a larger structure, the second simulation included a cube with an edge of 10 grid points, corresponding to an 80 µm side, represented in figure 4.26. The corresponding 3D simulated signals are shown in figure 4.27.

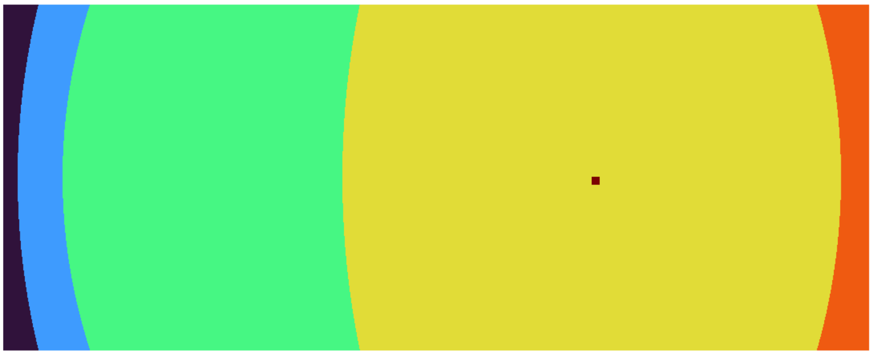

Figure 4.26. Eye matrix with a structure with a side of 80 µm placed in the middle of the lens (red).

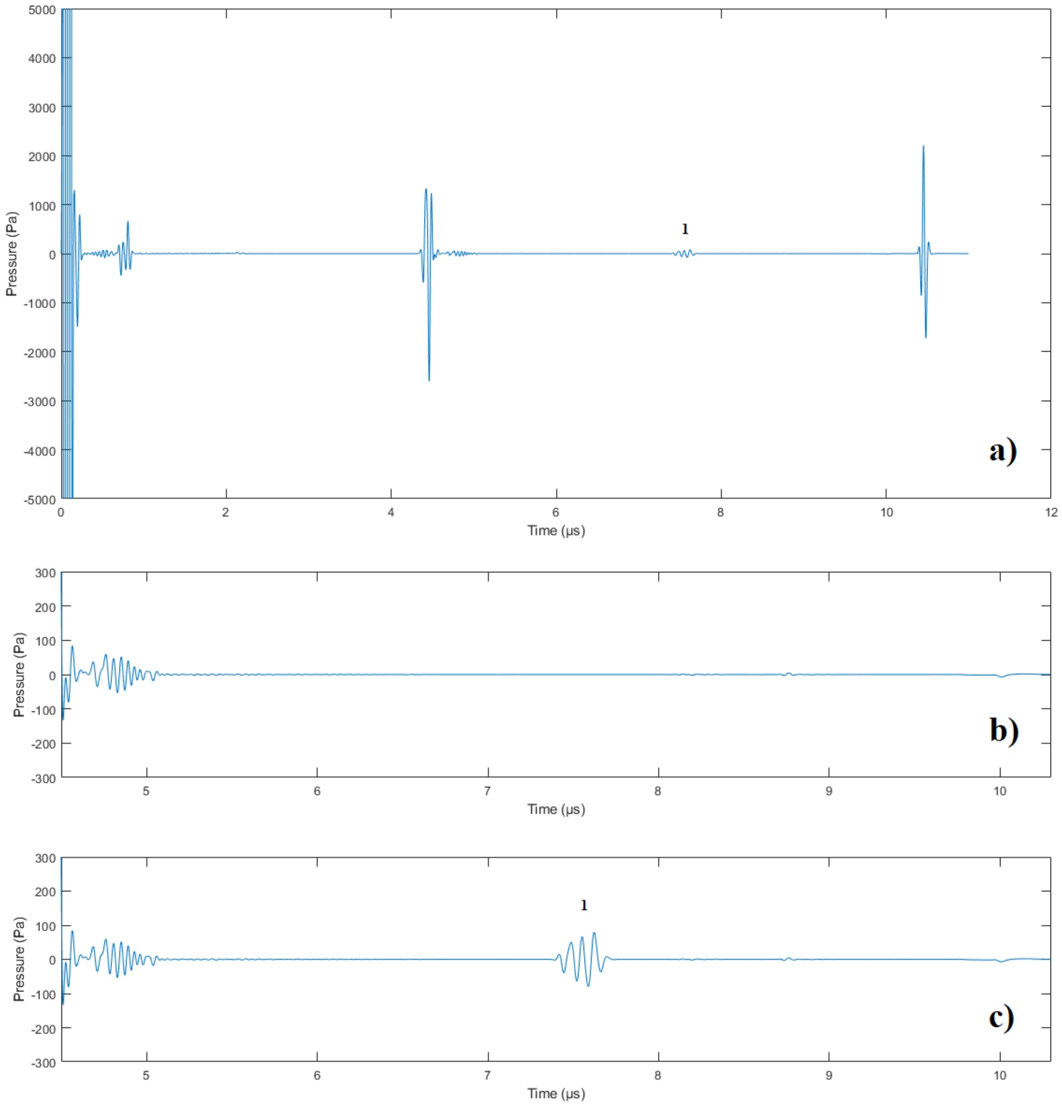

Figure 4.27. 3D simulated signal with a matrix resolution of 8 µm, with a structure in the middle of the lens, with 10 voxels side: a) complete 3D simulated signal, b) and c) zoom of the simulated signal corresponding to the lens thickness without (b) and with (c) the structure inside the lens. 1) scattering caused by the structure.

From the simulated signals, it is possible to verify that in the 3D signal the amplitude of the echo from the structure remains considerably lower than the amplitude of the echo from the anterior interface of the lens, despite being better evidenced than the smaller structure in 4.6.1.1. The relation between the maximum absolute amplitudes of the reflections in the anterior lens interface and the structure is approximately 33.

4.6.1.3. Multiple Structures with an Edge of 16 µm

The last simulation was performed using a matrix in which the anterior region contains several small structures with an edge of 16 µm randomly distributed in the anterior half of the lens. The corresponding 2D matrix is represented in figure 4.28. The simulated A-scan is represented in figure 4.29.

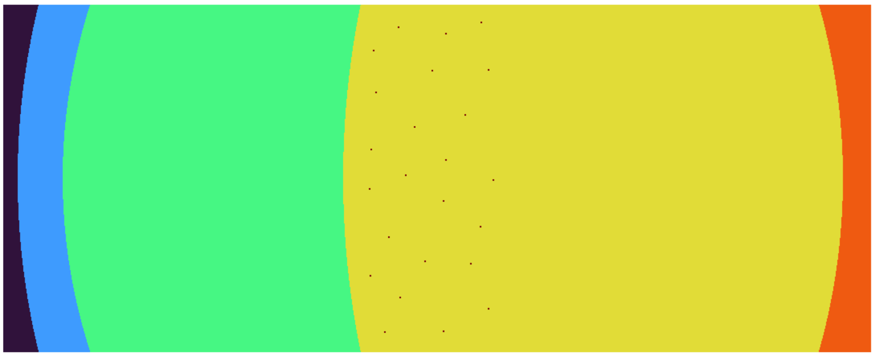

Figure 4.28. Eye matrix with multiple structures with 16 µm side in the anterior region of the lens (red dots).

From this last test, it is possible to see that, similarly to the first case where a single structure with an edge of 16 µm was placed inside the lens, in the 3D simulation the scattering caused by the structures inside the lens has a small amplitude when compared to the echo from the lens interfaces and it is detected while comparing figures 4.29b and 4.29c, representing the A-scans obtained using a matrix without any structure inside the lens and using the 3D matrix equivalent to the one in figure 4.28.

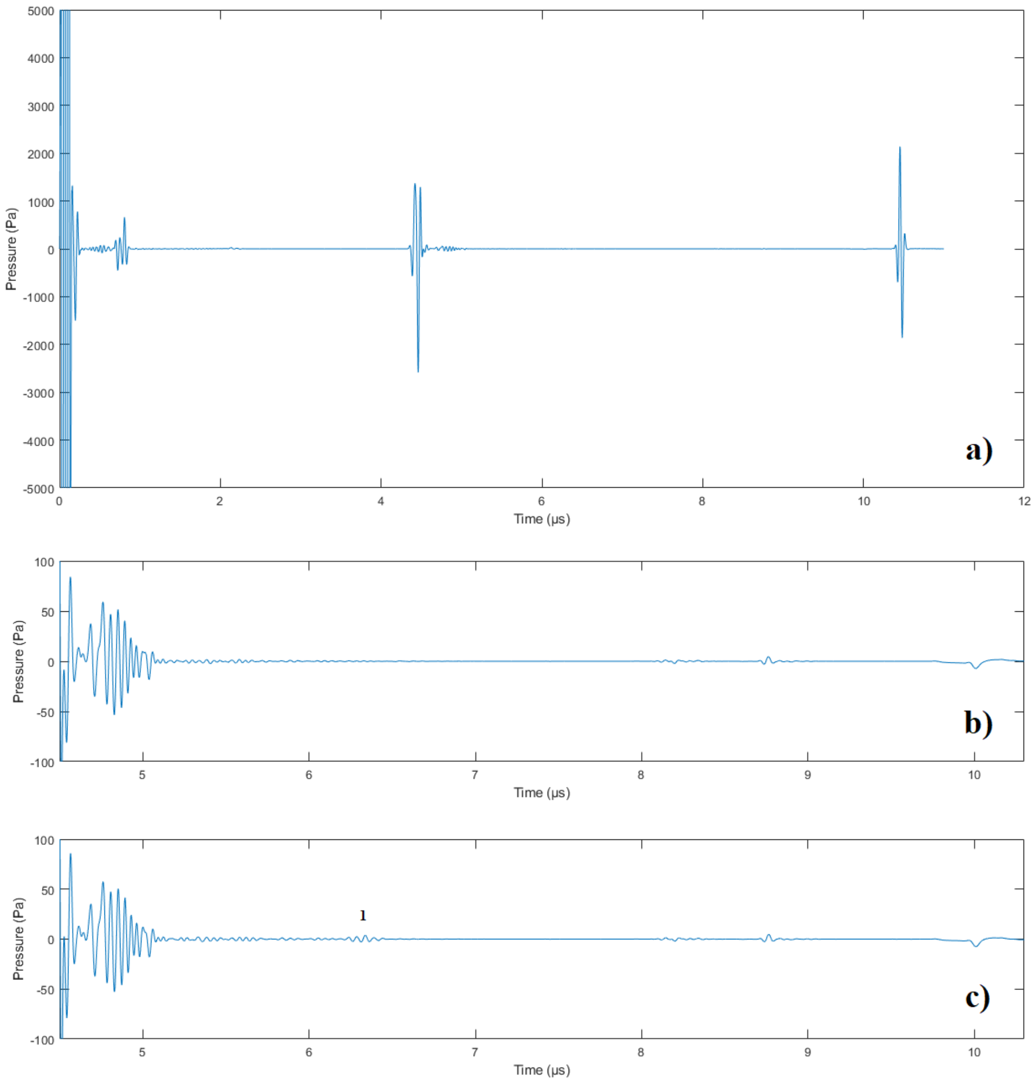

Figure 4.29. 3D simulated signal with a matrix resolution of 8 µm, with several structures in the anterior part of the lens, each with 2 voxels side: a) complete 3D simulated signal, b) and c) zoom of the simulated signal corresponding to the lens thickness without (b) and with (c) the structures inside the lens. 1) scattering caused by the structures.

4.6.2. Comparison with Real Signals

To address the fidelity of 3D simulations, the simulated signals were compared with real signals previously acquired with the ESUS system. All the acquired signals are from healthy eyes and consist of a mean of 10 A-scans to improve the signal-to-noise ratio.

Here, it was measured the total excursion. For all the real signals the ratio anterior/posterior excursion was close to 1 (table 4.16), as it was observed for the 3D simulated signal of figure 4.23, and diverging from the 2D simulated signal represented in figure 4.6, for which the ratio is closer to 2. An example of one real signal is presented in figure 4.30.

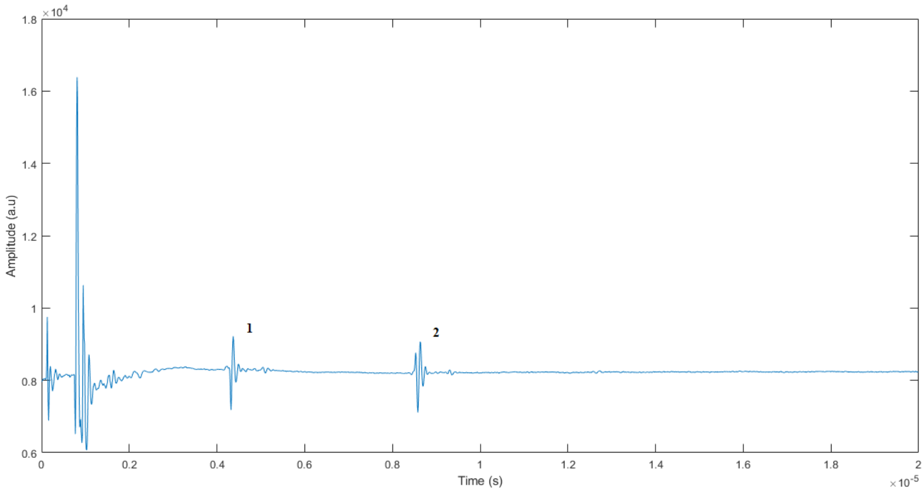

Figure 4.30. Example of a real signal from a healthy eye acquired with ESUS. 1) Anterior lens interface, 2) posterior lens interface.

Table 4.16. Excursions of the echoes of the lens interfaces from seven real signals, acquired with ESUS.

Signal	1	2	3	4	5	6	7
Anterior echo excursion (a.u)	2034.18	802.18	2035.36	833.73	1096.27	1829.37	414.82
Posterior echo excursion (a.u)	1952.64	1074.37	1304.19	814.54	1366.00	2439.55	1624.00
Excursion ratio (anterior/posterior)	1.04	0.75	1.56	1.02	0.80	0.75	0.25

Although the real signals were affected by several factors regarding the ESUS acquisition system, the operator and the diverse eye characteristics, the excursion ratios are similar to those obtained through 3D simulations.

4.7. Simulation Results

This chapter included the results of 2D and 3D simulations of ultrasonic waves propagating through the eye. To minimize the computational resources, the eye matrix was reduced to a region of interest defined as the zone between the beginning of the cornea and the end of the lens, and the central part of the eye, delimited by the diameter of the focused ultrasonic probe (3.2 mm). The simulation with this matrix presented similar results to simulations with the whole matrix. The results of 2D and 3D simulations presented considerable differences regarding the amplitudes and pulse duration of the echoes from the lens interfaces. Then, the resolution was improved to enable the 3D simulations considering the dimensions of microscopical structures that characterize the cataract. The adopted resolution was 8 µm. When comparing the simulated signals with real signals acquired with ESUS, the 3D simulated signal presented the closest amplitude relation to the real signals, as would be expected since 3D constitutes a more accurate approximation to the real human eye, as 2D simulation constitutes an acceptable approximation. Therefore, considering the obtained results, 3D simulations should be implemented, although it requires more computational resources, making simulations impracticable when using personal computers. To address the future simulation of cataract structures, this chapter also included the simulation of microscopical structures inside the lens. The scattering caused by these small structures, with dimensions between 16 and 80 µm, was identified in 3D simulated signals.

5. Model of the Probe

In this chapter, the characterization of the ophthalmologic probe in terms of its impulse response is addressed to obtain a model of the complete system. The methods and materials are presented, including the experimental setup, and the implementation of different methods is discussed. Finally, the method that leads to the best results is used to obtain a simulation of the complete system.

5.1. Materials and Methods

Since the ophthalmologic probe operates in pulse-echo mode, the only signals that can be acquired are the electrical excitation signal that the generator sends to the probe, and the electrical signal generated by the probe after the acoustic wave has traveled through the medium. As it was previously referred to, there are two transfer functions to estimate when modeling the ophthalmologic probe: the electric-to-acoustic and the acoustic-to-electric transfer functions. Given these circumstances and considering the conclusions from Fa et al. (2008), it was proposed the model of the global transfer function (electric-to-electric). The two individual transfer functions would then be calculated, assuming they are reciprocal.

To model the global frequency response of the ultrasonic probe, the echo signal from a controlled experiment must be considered. Therefore, a reflector surface at a known distance in water is used. The sensor must be at a distance from the reflector approximately equal to its focal length. It is assumed that the reflected signal is only affected by attenuation and delay.

The distance between the probe and a reflecting interface (d) is experimentally calculated using the time-of-flight method (equation 5.1). Knowing the sound speed in the coupling medium (v), the distance is determined after the measure of the time interval (Δt) between pulse emission and the arrival of the echo reflected in the interface.

$$d = \frac{v \, \Delta t}{2} \tag{5.1}$$

5.1.1. Experimental Setup

To acquire the referred electrical signals several measurements were performed using the A-scan 20 MHz ophthalmologic probe (Appendix A) (figure 5.1), which was vertically coupled to a micro positioning system. The probe and a plane reflector were immersed in an acrylic container filled with distilled water. There were used two different signal generators: a broadband pulser/receiver (Panametrics, 5800) and an arbitrary function generator (Tektronix, AFG 3101). When the pulser/receiver is used the ultrasonic reflected signal is collected, amplified, and filtered by the pulser/receiver. Then, it is displayed on an oscilloscope (Tektronix, TDS 1002B) and saved for further processing. When the arbitrary function generator is used the output signal is directly connected to the oscilloscope. The experimental setup when using the pulser/receiver is shown in figure 5.2.

Figure 5.1. A-scan 20 MHz ophthalmologic probe.

Figure 5.2. Experimental setup: 1) oscilloscope, 2) pulser/receiver, 3) micro positioning system, 4) acrylic container.

A third experimental setup used the ESUS acquisition system, described in chapter 3, which is composed of the same ophthalmologic probe, the xSCAN module responsible for the electric excitation of the probe and signal acquisition, and a computer where the signals were displayed. All the signal processing was performed using MATLAB.

5.1.2. Transfer Function Modeling

In the case of a probe operating in pulse-echo mode, the electric-to-electric transfer function in the frequency domain is given by equation 5.2, where all the elements are represented by their transfer function. X is the excitation signal applied to the probe and Y is the received echo. C_1 and C_2 represent the electric cables and connectors, H_1 and H_2 correspond to the electric-to-acoustic and acoustic-to-electric conversions on the transducer, respectively. W_1 and W_2 represent the coupling medium, R is the reflection coefficient of the plane reflector, and O corresponds to the oscilloscope:

$$Y(s) \ = \ X(s)C_1(s)H_1(s)W_1(s)R(s)W_2(s)H_2(s)C_2(s)O(s) \tag{5.2}$$

The influence of the cables, connectors, and oscilloscope was not considered. The propagation through the coupling medium (which is water in this case) and the reflection in the plane reflector were approximated to a delay t_d, with transfer function $e^{-t_d s}$ (Fa et al, 2018).

Considering that the electric-to-acoustic and the acoustic-to-electric conversion properties of the transducer are reciprocal, the partial transfer functions, H_1 and H_2, are equal and the equation that describes the system becomes:

$$Y(s) \ = \ X(s)e^{-t_d s}H_1(s)H_2(s) \ = \ X(s)e^{-t_d s}H_1^2(s) \tag{5.3}$$

Therefore, it is possible to write $H_1(s) = H_2(s) = \ H(s)$. The modulus of the global transfer function ($|H_{tot}|$) was determined with equation 5.4, considering that $|e^{-t_d s}| = 1$.

$$|H_{tot}| = |H^2(s)| \ = \ \left|\frac{Y(s)}{X(s)}\right| \tag{5.4}$$

The inverse Fourier transform of H_{tot} returns the global impulse response, h_{tot}, characterizing the electric-to-electric conversion. The electric-to-acoustic and acoustic-to-electric transfer function (H), is calculated as the square root of H_{tot} and the impulse response that characterizes this conversion (h) is determined through the inverse transform of H. Considering the convolution theorem, the relation presented in equation 5.5 should verify.

$$h_{tot}[n] \ = \ h[n] * h[n] \tag{5.5}$$

After H is obtained, it can be modeled in the frequency domain as a ratio of polynomials (equation 5.6).

$$H_{model}(s) = \frac{Num(s)}{Den(s)} \tag{5.6}$$

Where $Num(s)$ and $Den(s)$ are the numerator and the denominator polynomials, respectively. The roots of the numerator polynomial (a_k) are called the zeros of $H_{model}(s)$ and the roots of the denominator (b_k) are referred to as the poles of $H_{model}(s)$.

Therefore, equation 5.6 can be written in terms of its zeros and poles (equation 5.7) (Oppenheim and Willsky, 1996; Haykin and Veen, 2002).

$$H_{model}(s) = G\,\frac{\prod_{k=1}^{P}(s + a_k)}{\prod_{k=1}^{Q}(s + b_k)} \tag{5.7}$$

Where G is the gain factor and P and Q represent the orders of the numerator and the denominator polynomials, respectively.

5.1.3. Impulse Response by Optimization

To model the probe, $h[n]$ can be estimated directly from equation 5.5 considering the discrete convolution. Therefore, an approach based on a function included in the MATLAB Optimization Toolbox was considered. The function `fsolve` is used to solve a system of nonlinear equations. This function returns the solution of a problem specified by $F(x) = 0$. If the solution does not exist, the function returns the minimum *x* value that approximates the solution to zero, turning the problem into a minimization problem.

In this case the goal is to determine the impulse response that, once convolved with itself, returns the global impulse response obtained using the measured signals. This problem can be described as: $h[n] * h[n] = h_{tot}[n]$. Since this is an optimization problem, it is described as:

$$h^{*}[n] = argmin_{h[n]}\{(h[n] * h[n] - h_{tot}[n])\} \tag{5.8}$$

Where $h^{*}[n]$ is the optimal impulse response. The `fsolve` MATLAB function takes as arguments the function describing the optimization problem to solve (`fun`), the starting point (`x0`), and the optimization options to consider when solving the problem (`options`), which include the possibility to use a defined Jacobian for the function to be optimized and display the output at each iteration.

```
h = fsolve(fun,x0,options).
```

Therefore, the function used by `fsolve` is $F = h[n] * h[n] - h_{tot}[n]$. After several iterations, the result is the impulse response ($h[n]$) that characterizes the electric-to-acoustic and acoustic-to-electric conversions in the ultrasonic probe.

5.2. Probe Focal Length and Central Frequency

Considering the experimental setup described in section 5.1.1 using the pulser/receiver, the focal length of the probe was calculated with equation 5.1. The time interval (Δt) was measured with the oscilloscope. The constant sound speed in water is 1494 m/s (Petrella et al, 2021) and the measured Δt is equal to 12.9 µs. Therefore, the focal distance was estimated as d = 9.6 mm.

To confirm that the probe was correctly positioned, the position of the probe was changed around the estimated value for the focal point and its peak amplitude was measured, as it is represented in figure 5.3.

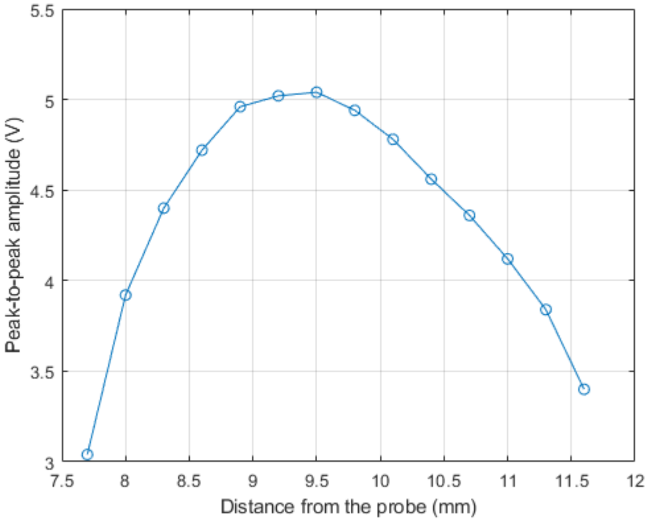

Figure 5.3. Maximum peak-to-peak amplitude as a function of the distance between the probe and the reflector.

For central frequency determination, the arbitrary function generator was used to generate a sinusoidal burst with a certain frequency and number of sinusoidal oscillations. The peak amplitude was fixed to 10 V, and 1 and 2 sinusoidal cycles were considered. The echo peak-to-peak amplitude was measured as a function of the frequency, which was within the range of 14-26 MHz. The results are presented in figure 5.4.

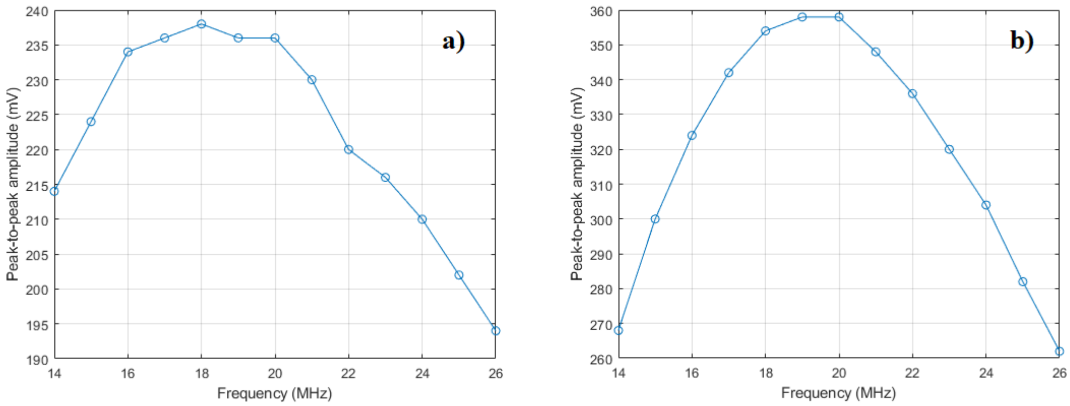

Figure 5.4. Peak-to-peak amplitude as a function of frequency, considering an excitation burst with 10 V of amplitude and 1 (a) and 2 (b) cycles.

Considering the selected range, the probe responds with higher amplitude to frequencies around 20 MHz, which agrees with the central frequency of the manufacturer datasheet (Appendix A).

5.3. Measurements

5.3.1. Arbitrary Function Generator

The arbitrary function generator was used to provide the probe excitation with a sinusoidal signal with a frequency of 20 MHz, 3 cycles, and 10 V. The acquired signals are represented in figures 5.5 a) and 5.6 a), as well as the corresponding frequency spectrums (5.5 b) and 5.6 b)). The frequency spectrums were determined using the `fft` MATLAB function, which implements the Fast Fourier Transform (FFT) algorithm.

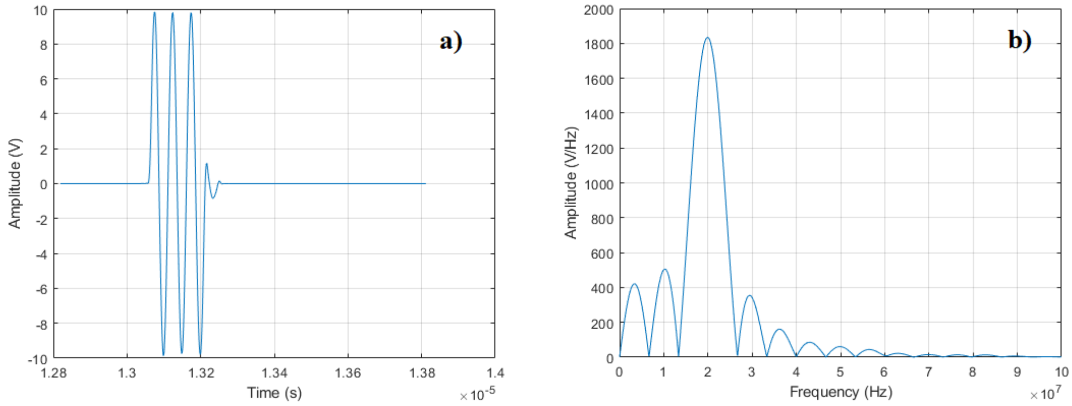

Figure 5.5. Excitation signal (a), and the corresponding frequency spectrum (b).

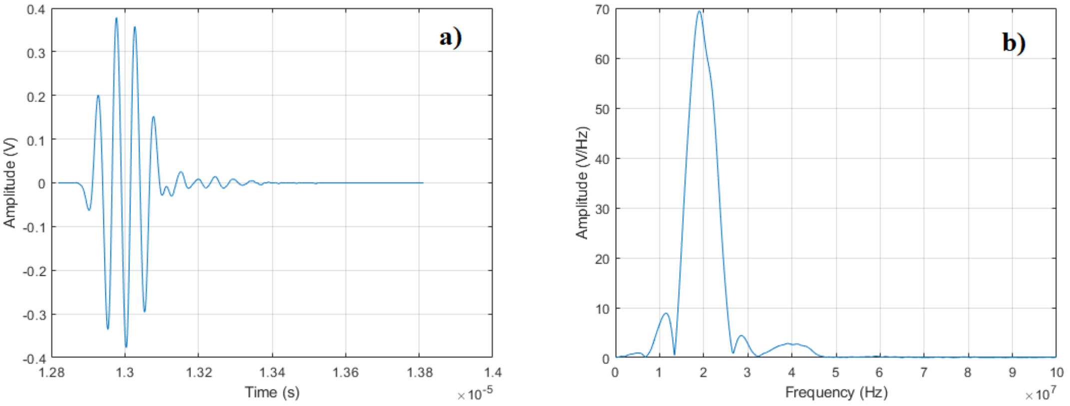

Figure 5.6. Echo signal received by the probe (a), and the corresponding frequency spectrum (b).

5.3.2. Pulser/Receiver

Using the pulser/receiver to provide the electric excitation to the ultrasonic probe, the electric excitation signal and the corresponding frequency spectrum were obtained, and are presented in figure 5.7. The excitation signal (figure 5.7 a)) was acquired using an x10 oscilloscope probe, which was previously calibrated.

After the ultrasound wave propagates through the medium, the electrical signal was acquired and its FFT was determined in MATLAB. The echo signal and its corresponding frequency spectrum are represented in figure 5.8.

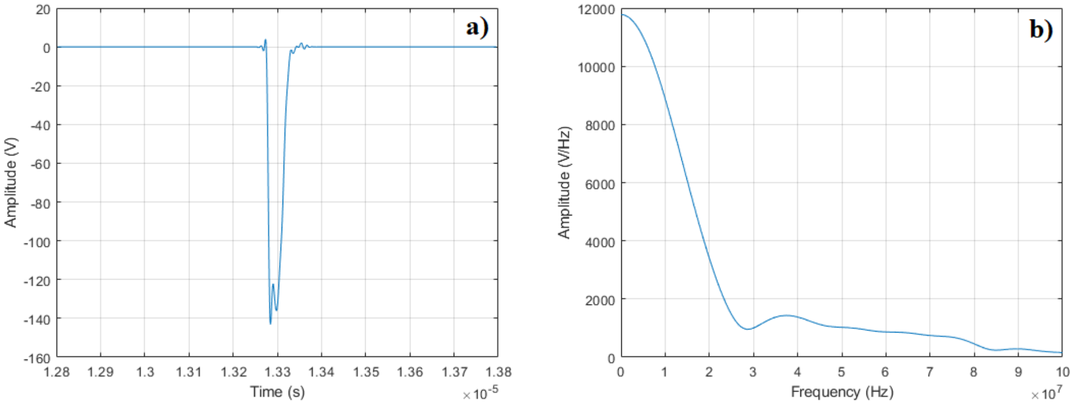

Figure 5.7. Electric excitation signal from pulser/receiver output (a) and the respective frequency spectrum (b).

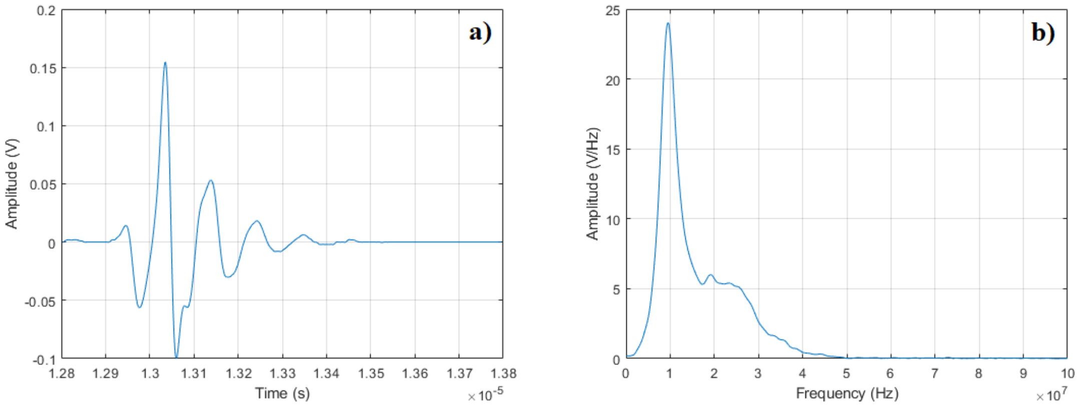

Figure 5.8. Echo signal obtained with the pulser/receiver after propagation in the medium (a) and the corresponding frequency spectrum (b).

5.3.3. ESUS

The ESUS system was used to acquire the electric excitation signal generated by the xSCAN module and sent to the probe, and the received electrical signal that arrives again at the xSCAN after propagating in the medium. The excitation signal and its respective frequency spectrum are represented in figure 5.9.

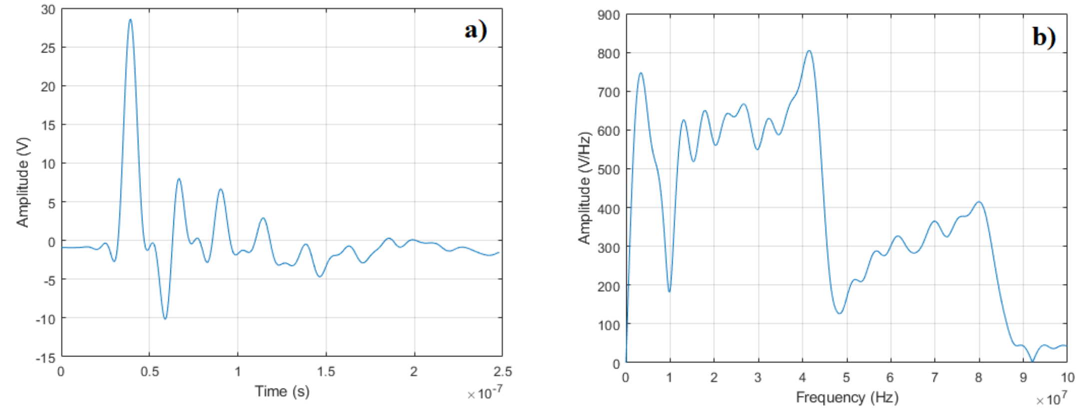

Figure 5.9. Excitation signal obtained with the ESUS acquisition system (a) and the respective frequency spectrum (b).

After the propagation and reflection in the plane reflector, the electric signal received by the xSCAN module, and the corresponding frequency spectrum are represented in figure 5.10.

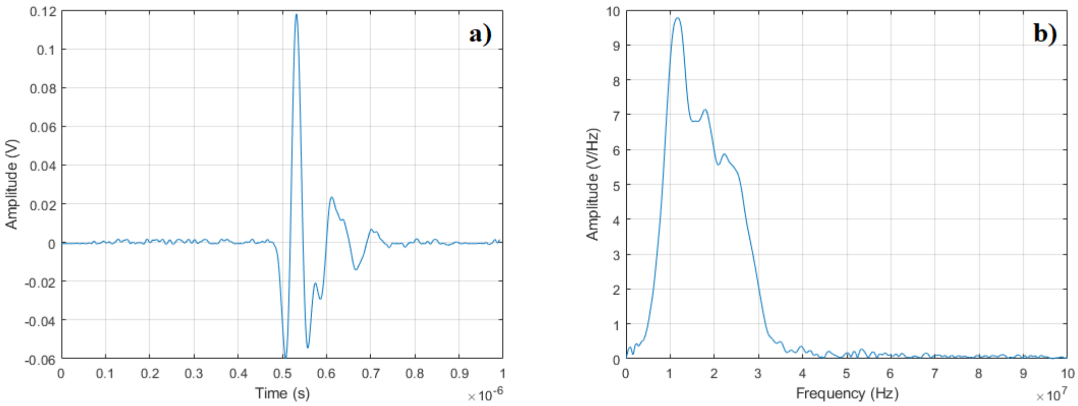

Figure 5.10. Echo signal acquired with the ESUS (a) and the corresponding frequency spectrum (b).

5.4. Modeling of the Probe

5.4.1. Gamma-Tone Model

The received echo obtained using the arbitrary function generator as an excitation signal was modeled with the gamma-tone approach, using the expression in equation 3.7.

The gain (c), the system order (n), the decay temporal coefficient (β), the center frequency (ω_0), and the phase (ϕ) were calculated using MATLAB. To determine the value of the parameters, the envelope of $y_g(t)$ ($r(t)$) is determined using the Hilbert transform. The mean (μ) and the mode (t_m) of $r(t)$ are obtained. Then, parameters n and β are calculated using the following expressions:

$$t_m = \frac{n-1}{\beta}, \mu = \frac{n}{\beta} \tag{5.9}$$

The parameter c is calculated from the maximum value of the envelope $r(t_m) = c\, {t_m}^{n-1} e^{-\beta t_m}$, using expression in equation 5.10.

$$c = r(t_m) \left(\frac{e\,\beta}{n-1}\right)^{n-1} \tag{5.10}$$

Finally, the FT of $y_g(t)$ is obtained and used to determine the parameters ω_0 and ϕ, corresponding to the frequency and phase for which the module of the FT has its maximum value.

The resulting parameters were:

$$c = 5.123 \times 10^{14}, n = 2.995, \beta = 2.818 \times 10^{7}, f_0 = 1.907 \times 10^{7}\ Hz, \phi = 4.160\ rad.$$

The representation of the acquired echo signal, the modeled gamma-tone signal, and the envelope of the gamma-tone are represented in figure 5.11.

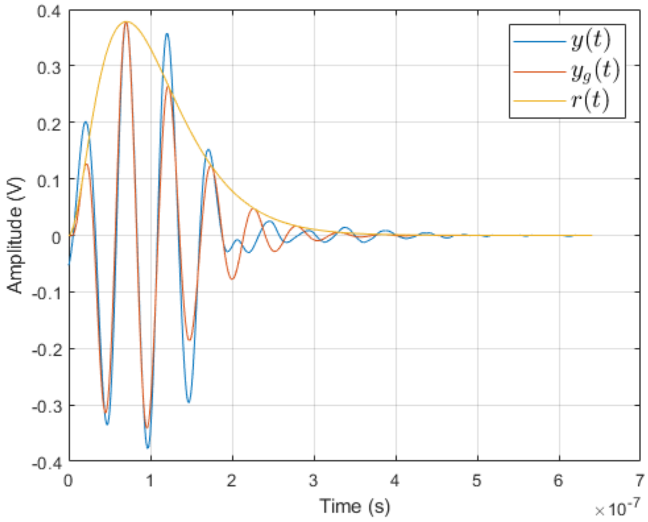

Figure 5.11. Representation of the measured echo signal ($y(t)$), the corresponding gamma-tone signal ($y_g(t)$), and the envelope of the gamma signal ($r(t)$).

The obtained parameters enable the modeling of the received echo signal. However, the excitation pulse also influences the probe response. It is possible to observe in figure 5.5b that the frequency response of the excitation signal is centered around the frequency range of the probe (20 MHz). Therefore, the signal to be modeled is not the received echo but instead the total impulse response of the probe (h_{tot}). The total impulse response (figure 5.12) was obtained with the inverse FT of the global transfer function, which was calculated with equation 5.4. The total impulse response however cannot be modeled as a gamma-tone in this case since its shape does not show similarities with a gamma function. Other approaches are explored in the next section.

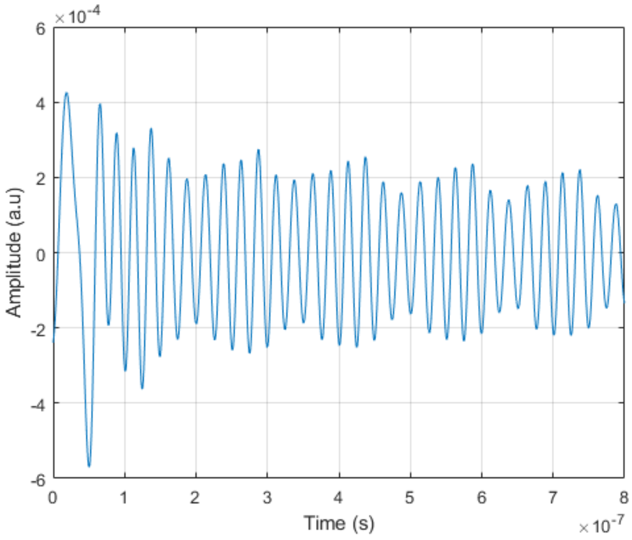

Figure 5.12. Impulse response of the probe obtained with the acquired signal using an arbitrary function generator.

5.4.2. Partial Transfer Function (*H*) Modeling

Considering the calculated frequency spectrums from the excitation signal and the received echo from section 5.3.2, the module of the global transfer function corresponding to the complete system ($|H_{tot}|$) was determined using equation 5.4 and represented in figure 5.13.

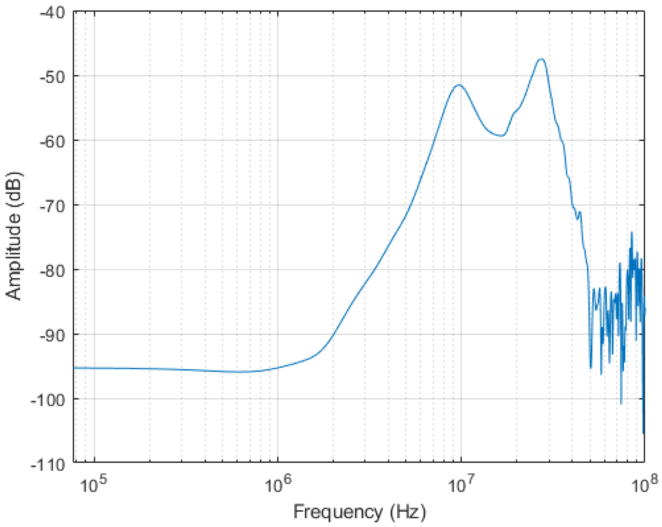

Figure 5.13. Magnitude of the global frequency response of the probe ($|H_{tot}|$).

To verify the hypothesis in equation 5.5, $h_{tot}[n]$ and the convolution $h[n] * h[n]$ were calculated and represented in figure 5.14.

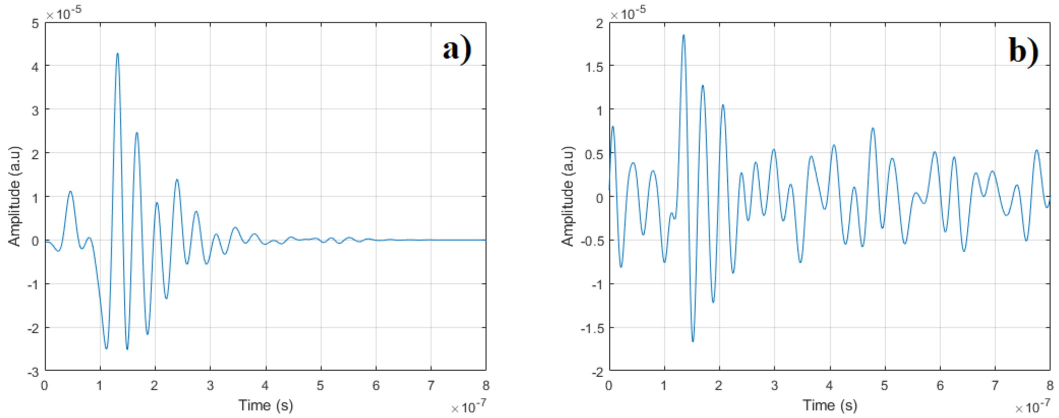

Figure 5.14. Global impulse response $h_{tot}[n]$ (a) and convolution of the impulse response with itself ($h[n] * h[n]$) (b).

To compare the two functions represented in figure 5.14, the coefficient of determination (R^2), a statistical measure that tells how well the model fits the measured data, was obtained using the `fitlm` MATLAB function: R^2 = 0.390. It is possible to observe that these functions are not equivalent, meaning that either the electric-to-acoustic and acoustic-to-electric transfer functions are not reciprocal, opposite to that suggested, or the coupling medium does not introduce only a delay but instead has a more complex influence on the system response. Therefore, the estimated model of the probe should be an approximation.

The model was estimated starting with the module of *H*, represented in figure 5.15.

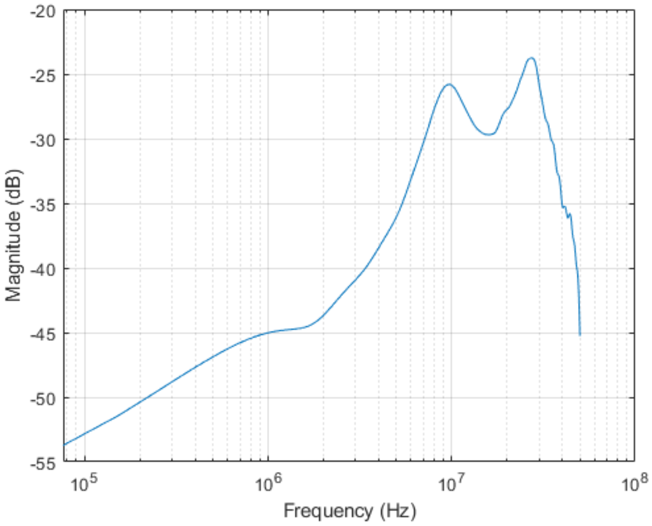

Figure 5.15. Module of the electric-to-acoustic and acoustic-to-electric frequency response of the probe (*H*), corresponding to the electric-to-acoustic transfer function.

The *H* model was estimated as a rational function in the *s* domain, with zeros at frequencies 2 MHz (ω_1) and 20 MHz (ω_2), since for these frequencies the gain rises at a rate of 20 dB/decade (figure 5.15). Another zero was added at frequency 50 MHz (ω_3) to impose a decrease in gain at the rate of -20 dB/decade. The model also includes two pairs of complex poles at frequencies 9.6 MHz (ω_4) and 28 MHz (ω_5), where the two peaks occur, imposing a decrease in gain at a rate of -40 dB/decade (figure 5.15). The model of the electric-to-acoustic transfer function is given by equation 5.11, where G is the gain factor, for which the estimated value is equal to 1.012×10^6.

$$H_{model}(s) = G \, \frac{(s+\omega_1)(s+\omega_2)(s+\omega_3)}{(s^2 + d\omega_4 s \ + \ \omega_4^2)\,(s^2 + d\omega_5 s \ + \ \omega_5^2)} \tag{5.11}$$

The comparison between the estimated model (H_{model}) and the measurement (*H*) is presented in figure 5.16.

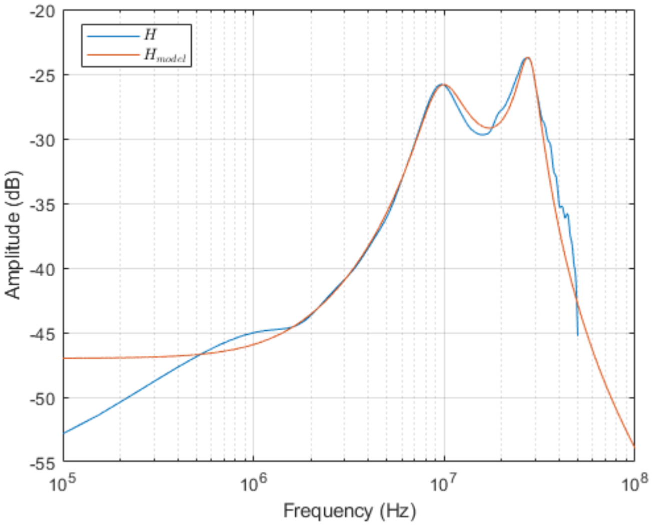

Figure 5.16. Comparison between the modules of the transfer function determined by the model (H_{model}) and the partial frequency response of the probe (*H*).

The estimated model appears to be similar to the result obtained with the experimental measurements. The impulse response given by the model that characterizes the electric-to-acoustic (and the acoustic-to-electric) signal conversion of the probe (h_{model}) was determined and represented in figure 5.17.

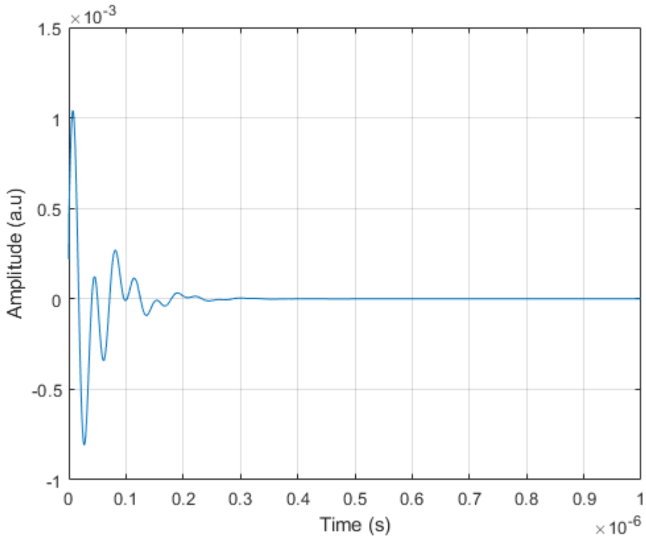

Figure 5.17. Impulse response that characterizes the electric-to-acoustic signal conversion of the probe (h_{model}), as a result of the estimated model.

To verify the viability of this solution, the acquired received echo signal (figure 5.8 a)) and the echo obtained with the model were compared, calculated with equation 5.12, was determined and are represented in figure 5.18.

$$y[n] \; = \; (h_{model}[n] * h_{model}[n]) \; * \; x[n] \tag{5.12}$$

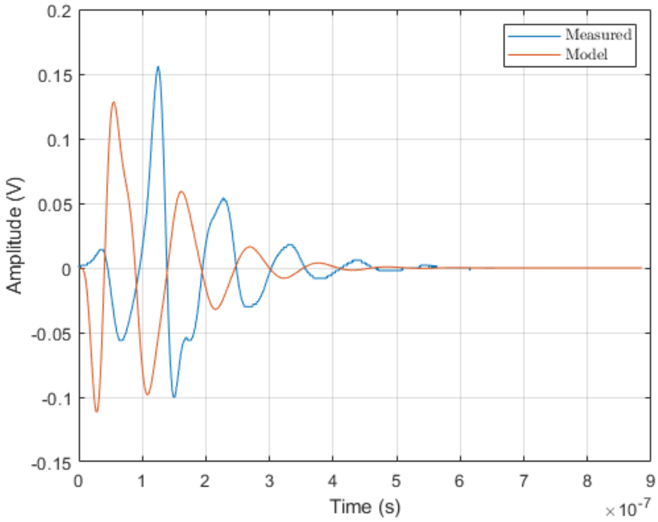

Figure 5.18. Comparison between the echo signal measured using the pulser/receiver and the modeled echo signal using the estimated impulse response.

This result shows that the estimated model is not the optimal approximation, since the two echo signals are not coincident and the obtained coefficient of determination was $R^2 = 0.445$. Another approach is explored in the next section to obtain a closer approximation for the electric-to-acoustic and acoustic-to-electric signal conversion in the probe.

5.4.3. Impulse Response Modeling with Pulser/Receiver Measurements

The `fsolve` MATLAB function was implemented using the acquired signals from the measurements with the pulser/receiver (section 5.3.2), and after several iterations, it returned the impulse response (h_{model}) represented in figure 5.19.

Once the optimal solution was obtained, its frequency response was calculated with the FFT and compared to the frequency response obtained directly from the measurements observing that the solution is similar to the experimental results, especially considering that the two poles at 9.6 MHz and 28 MHz are well defined (figure 5.20).

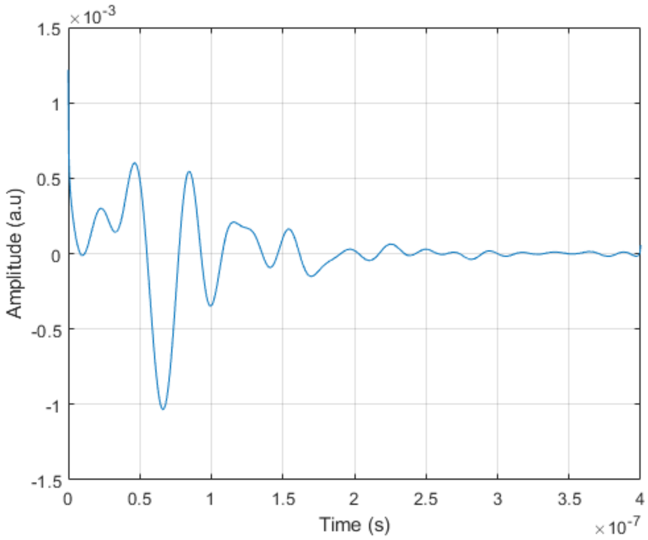

Figure 5.19. Impulse response $h_{model}[n]$ returned by `fsolve`.

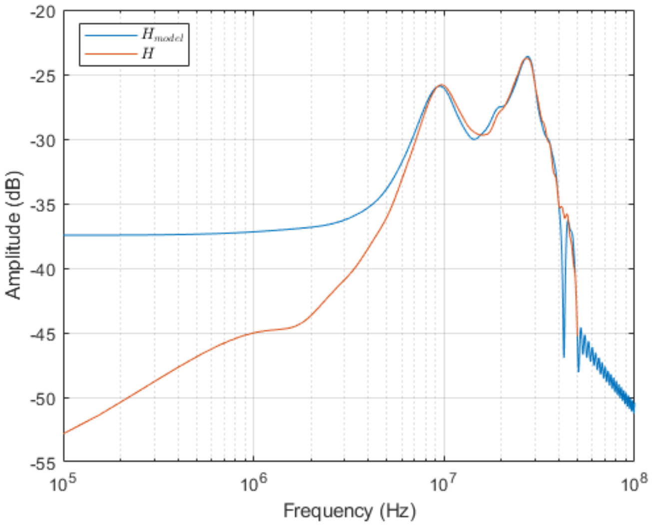

Figure 5.20. Comparison between the modules of the electric-to-acoustic transfer function given by the solution of the optimization problem (H_{model}) and the partial frequency response of the probe determined with the measured signals (H).

Considering that the convolution of the impulse response with itself is equivalent to the total impulse response (equation 5.5), the convolution of the global impulse response with the excitation signal returns the received echo signal that should be similar to the measured signal (figure 5.8 a)). The comparison between the optimized solution and the measured signal is represented in figure 5.21. This is an acceptable solution, with a better outcome than the previous model (section 5.4.2), since the coefficient of determination is closer to unity: R^2 = 0.975.

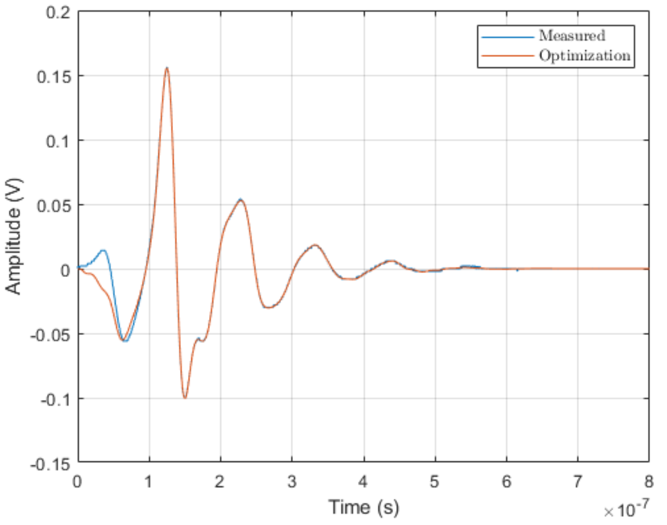

Figure 5.21. Comparison between the echo signal measured with the pulser/receiver and the modeled echo signal using the optimization technique.

5.4.4. Impulse Response Modeling with ESUS Measurements

The module of the global frequency response of the probe ($|H_{tot}|$) is calculated using the convolution property (equation 5.4), and the measured signals presented in section 5.3.3, and the result is shown in figure 5.22.

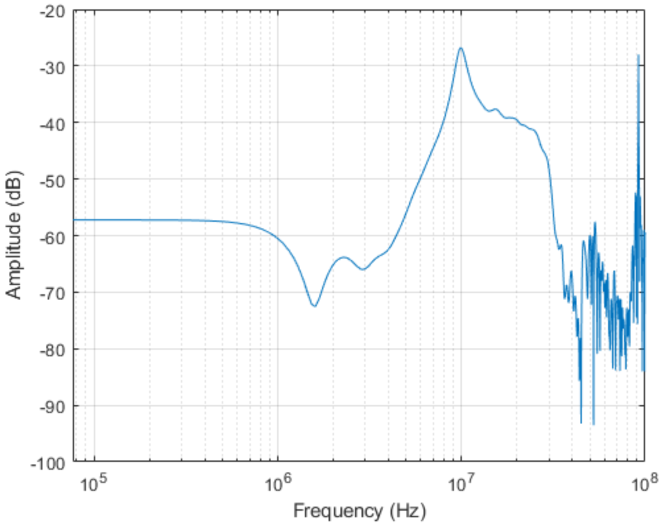

Figure 5.22. Module of the global frequency response of the probe ($|H_{tot}|$).

Since in the previous case the `fsolve` function returned the best approximation for the impulse response of the probe, the same function is applied to the signals acquired with ESUS. The resulting impulse response (h_{model}) is presented in figure 5.23.

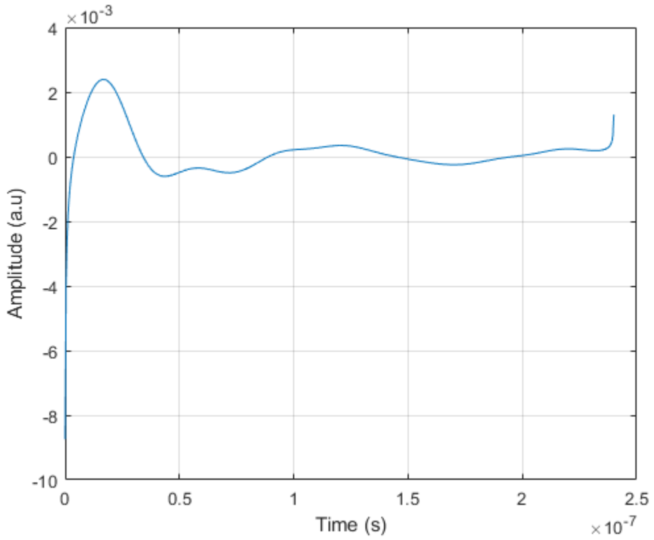

Figure 5.23. Impulse response resulting from the optimization problem using signals acquired with ESUS.

The frequency spectrum (H_{model}) is determined by the FFT of the obtained impulse response and compared with H. This comparison is presented in figure 5.24.

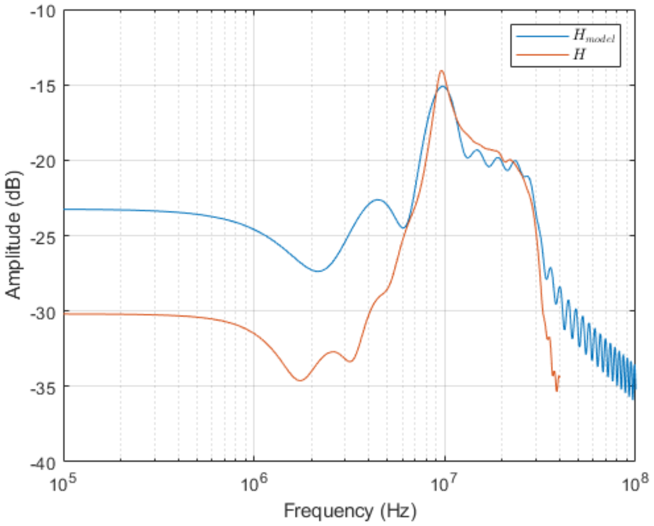

Figure 5.24. Comparison between the modules of the electric-to-acoustic transfer function given by the solution of the optimization problem (H_{model}) and the partial frequency response of the probe determined with the measured signals (H).

To verify the validity of the result, the echo signal was obtained and compared with the measured one (figure 5.10 a)). The modeled echo signal is determined with equation 5.12, using the excitation signal (figure 5.9 a)) and the impulse response returned by `fsolve` (figure 5.23). The comparison between the echoes is shown in figure 5.25 and quantified with the coefficient of determination: R^2 = 0.910.

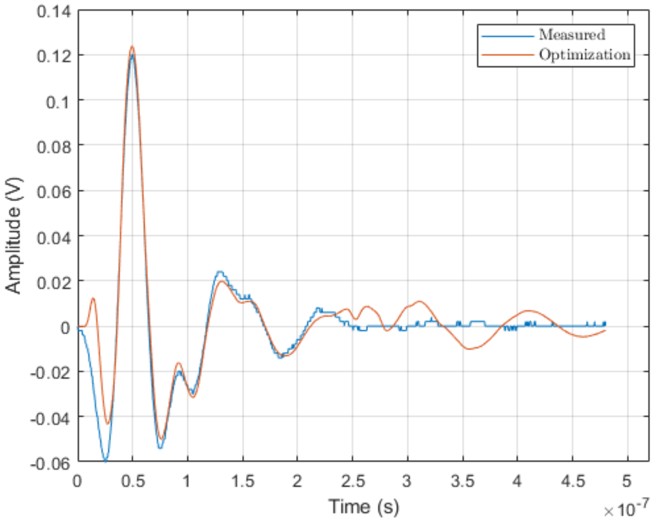

Figure 5.25. Comparison between the echo signal measured with the ESUS and the modeled echo signal using the optimization technique.

Looking at figure 5.25 and the determined R^2 it is possible to affirm that this is an acceptable result.

5.5. Modeling of the Complete System

5.5.1. Model with Pulser/Receiver Data

Since the result from section 5.4.3 represented the optimal solution for the problem, the next step is to use the obtained model of the probe in the simulation, to obtain signals closer to the real acquired signals from human eyes. Therefore, it is necessary to determine the acoustic signal that the probe sends to the medium. The convolution of the impulse response (figure 5.19) with the excitation signal (figure 5.7 a)) returns the intended pressure signal, represented in figure 5.26.

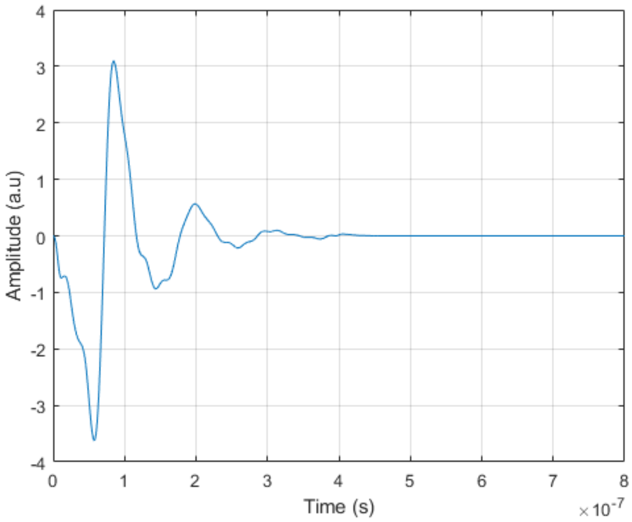

Figure 5.26. Pressure signal send by the probe to the medium.

This signal was used as the acoustic input signal emitted by the source in the simulation performed with the adopted 3D eye matrix with a resolution of 8 µm which central slice is illustrated in figure 4.22.

The result of the simulation is a pressure signal resulting from the propagation of the ultrasound wave through the eye. Using the same impulse response that also characterizes the acoustic-to-electric signal conversion, the acoustic simulated signal is then convolved with the impulse response to obtain the electric simulated signal, which can be compared with the real acquired signals. It is important to refer that the cornea flattening caused by the probe contact in the real signal acquisition was not represented in the simulation. The result of the simulation is an electric signal, represented in figure 5.27.

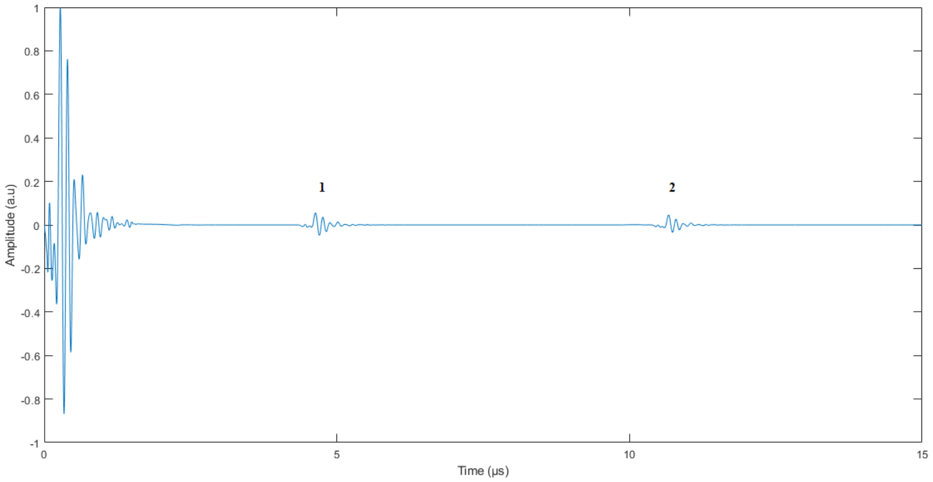

Figure 5.27. Electric simulated signal obtained with the determined acoustic input signal and after the propagation in the eye matrix. 1) anterior lens interface, 2) posterior lens interface.

The electric simulated signal is substantially different from the acoustic results presented in the last chapter. Only the echoes corresponding to the lens interfaces are observed, which are identified with numbers 1 and 2 in figure 5.27.

5.5.2. Model with ESUS Data

The acoustic signal sent by the probe to the medium is determined by the convolution of the impulse response (figure 5.23) and the electric signal that excites the probe (figure 5.9 a)).

The resulting pressure signal, shown in figure 5.28, was used as the input signal for a simulation with the same eye matrix and with the same characteristics of the medium, source, and sensor as in the previous simulation.

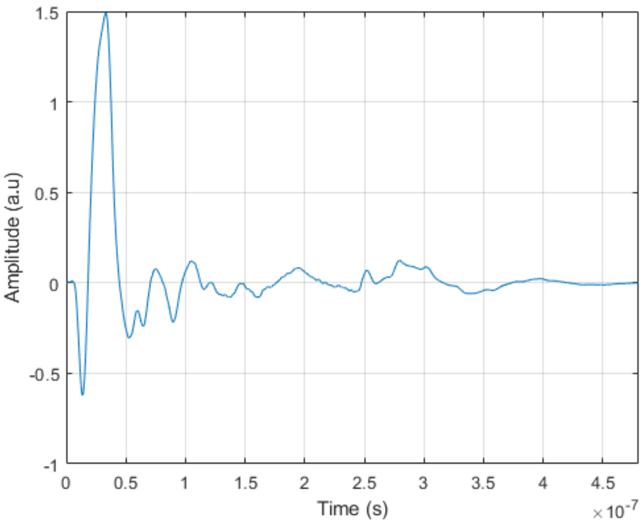

Figure 5.28. Pressure signal send by the probe to the medium.

The output is a pressure signal received by the probe after the ultrasound wave propagates through the medium. The conversion to an electric signal is done by the convolution of the acoustic simulated signal with the impulse response (h_{model}). The electric simulated signal is shown in figure 5.29.

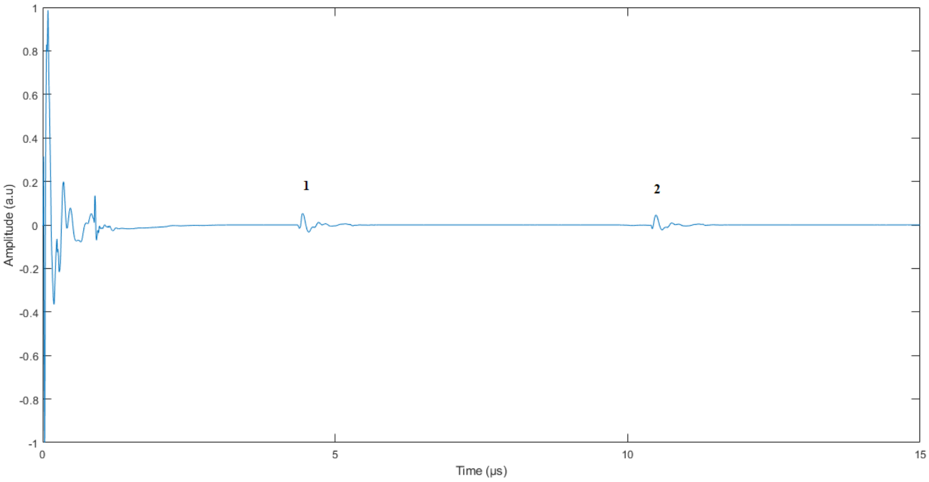

Figure 5.29. Electric simulated signal obtained with the determined acoustic input signal and after the propagation in an eye matrix. 1) anterior lens interface, 2) posterior lens interface

Just like it was observed for the electric simulated signal obtained with measurements using the pulser/receiver device, the echoes from the lens interfaces are the only echoes detected, and identified in figure 5.29 with numbers 1 and 2.

5.6. Comparison Between Simulated and Real Signals

The next step is the comparison of these simulation results with real signals acquired with ESUS, to investigate the similarities between them. To do that, the frequency spectrums of the echoes from the lens interfaces were determined.

The spectrums of the echoes from the anterior and posterior lens interfaces obtained with data acquired with the pulser/receiver device are represented in figure 5.30.

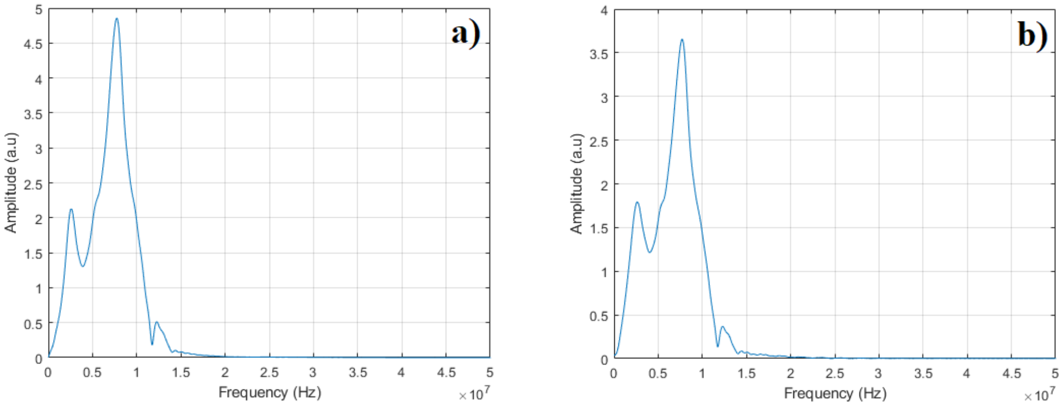

Figure 5.30. Spectrum of the part of the electric simulated signal corresponding to the echo from the anterior (a) and posterior (b) lens interfaces obtained with the model using the pulser/receiver.

The frequency spectrums of the echoes from the anterior and posterior lens interfaces obtained with data acquired with ESUS are represented in figure 5.31.

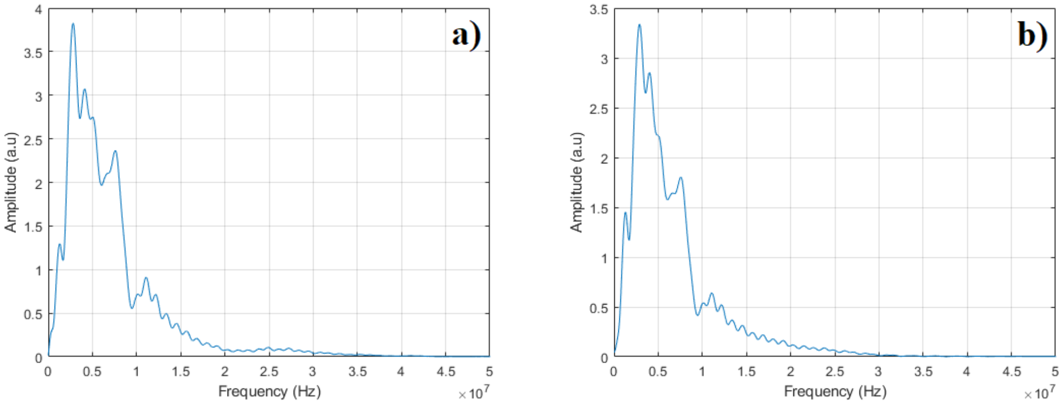

Figure 5.31. Spectrum of the part of the electric simulated signal corresponding to the echo from the anterior (a) and posterior (b) lens interfaces obtained with the model using ESUS.

The results from the two simulated signals are similar (figures 5.30 and 5.31). The frequency spectrums were also obtained for a real signal from a healthy eye, acquired with ESUS. The signal is presented in figure 5.32, and the frequency spectrums for the anterior and posterior lens interfaces are represented in figure 5.33.

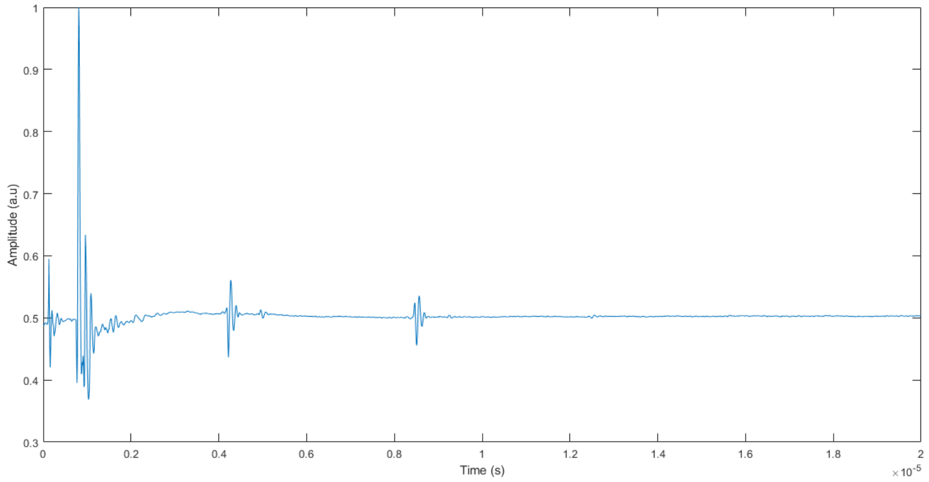

Figure 5.32. Real signal from a healthy eye acquired using ESUS.

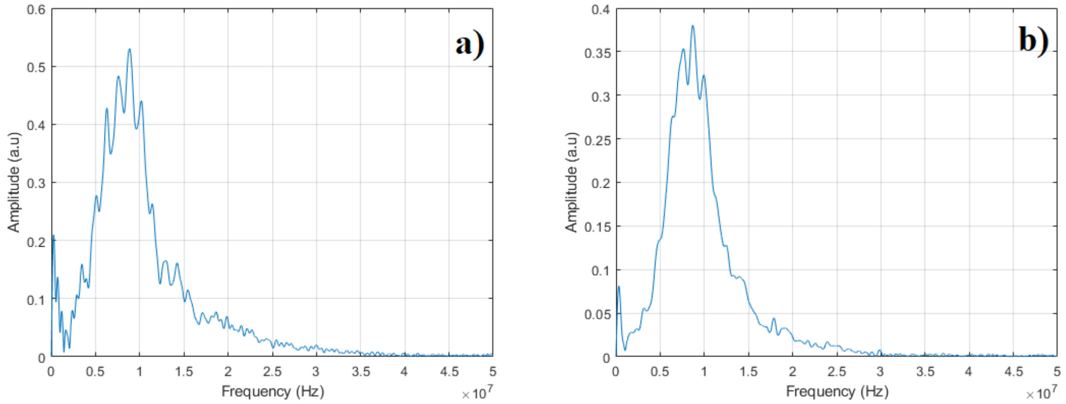

Figure 5.33. Spectrum of the part of the real signal corresponding to the echo from the anterior (a) and posterior (b) lens interfaces.

To conclude the study and to better compare the obtained results, the frequency spectrums obtained for the acoustic simulated signal in figure 4.23, determined without the influence of the probe, are presented below (figure 5.34). The simulated signal is the result of the simulation of an excitation pulse generated with the `toneburst` MATLAB function with the characteristics described in the previous chapter (Chapter 4) through the 3D eye matrix for which the central slice is illustrated in figure 4.22.

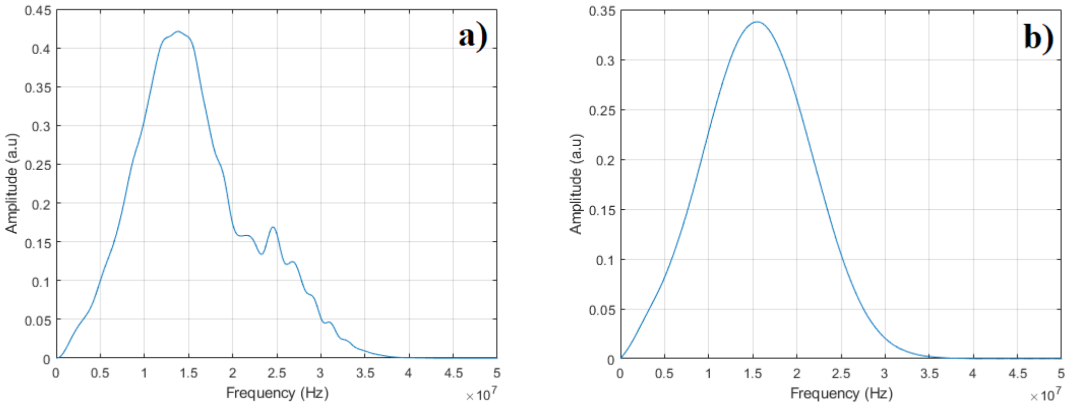

Figure 5.34. Spectrum of the part of the acoustic simulated signal corresponding to the echo from the anterior (a) and posterior (b) lens interfaces.

The comparison between the real and the simulated signals obtained for the complete system suggests that the estimated model using the `fsolve` MATLAB function returns satisfactory results, confirmed by the similarity between the frequency spectrums, with special emphasis on the result using the data acquired with ESUS, returning the best model as expected, since the equipment was the same used to acquire the real signals. If the probe response is not considered, the acoustic model presents a very different result (figures 4.23 and 5.34).

6. Conclusions and Future Work

In this study, it was implemented a model of the complete system for cataract detection including both, a model of ultrasonic waves propagation through the eye in 3D with a resolution of 8 µm, and the electrical/mechanical conversion in the ultrasonic probe in terms of its impulse response.

The present work demonstrated that 3D simulations return results closer to the real acquired signals. Therefore, the 3D model should be adopted in future works, namely the generation of a big dataset for training cataract classification algorithms associated with the ESUS. The remaining differences between real *in-vivo* human eyes signals and the simulated ones may result from diverse factors such as inaccuracies in the assumed acoustic properties and some limitations in the k-Wave algorithms.

The development of a model for the electric-to-acoustic and acoustic-to-electrical signal conversion within the ophthalmologic probe was implemented in terms of its impulse response. The model was used to simulate the complete system and the result resembles real signals acquired with the ESUS.

Future works will include the simulation of signals with diverse types and severities of cataract, to be used for features extraction, and automatic classification algorithms development. In this sense, computational models (eye matrices) for diverse cataract types and severities, and aleatory distribution of cataractous structures should be implemented. The simulated signals are noiseless, which differs from real situations. In future works when creating a dataset, a white noise component will be considered.

Overall, this project presents an acceptable solution for modeling the complete ESUS system that will be used to generate simulated signals from cataractous eyes in good agreement with real signals acquired with the clinical prototype.

Bibliography

Abell, R.G., Kerr, N.M., Howie, A.R., Kamal, M.A.A.M., Allen, P.L., Vote, B.J. (2014). Effect of femtosecond laser–assisted cataract surgery on the corneal endothelium. *J Cataract Refract Surg.*, 40(11): 1777-1783.

Abramowitz, M., Stegun, I. A. (1964). *Handbook of Mathematical Functions with Formulas, Graphs, and Mathematical Tables*. U. S. Department of Commerce, U. S.A.

American Academy of Ophthalmology. (2021). *What are Cataracts?*. Assessed on: april, 2022, available at: https://www.aao.org/eye-health/diseases/what-are-cataracts.

Beebe, D. C., Holekamp, N. M., Shui, Y. (2010). Oxidative Damage and the Prevention of Age-Related Cataracts. *Ophthalmic Research*, 44: 155-165.

Caixinha, M., Jesus, D. A., Velte, E., Santos, M. J., Santos, J. B. (2014). Using Ultrasound Backscattering Signals and Nakagami Statistical Distribution to Assess Regional Cataract Hardness. *IEEE Trans. Biomed. Eng.*, 61(12): 2921–2929.

Caixinha, M., Santos, M., Santos, J. (2016). Automatic Cataract Hardness Classification Ex Vivo by Ultrasound Techniques. *Ultrasound Med. Biol.*, 42(4): 989–998.

Caixinha, M., Amaro, J., Santos, M., Perdigão, F., Gomes, M., Santos, J. (2016). In-Vivo Automatic Nuclear Cataract Detection and Classification in an Animal Model by Ultrasounds. *IEEE Trans. Biomed. Eng.*, 63(11): 2326–2335.

Chylack LT, Wolfe JK, Singer DM, Leske MC, Bullimore MA, Bailey IL, Friend J, McCarthy D, Wu SY. (1993). The Lens Opacities Classification System III. The Longitudinal Study of Cataract Study Group. *Arch Ophthalmol.*, 111: 831–6.

Darling, A. M. (1991). *Properties and implementation of the gammatone filter: a tutorial*. University College London, Department of Phonetics and Linguistics. 43-61.

Davison J.A, Chylack, L.T. (2003). Clinical application of the lens opacities classification system III in the performance of phacoemulsification. *J Cataract Refract Surg.*, 29: 138–145.

Ecroyd, H., Craver, J.A. (2009). Crystallin proteins and amyloid fibrils. *Cell. Mol. Life Sci.*, 66(1): 62-81.

Eurostat. (2019). *Cataract surgery: how countries compare*. Assessed on: july, 2022, available at: https://ec.europa.eu/eurostat/web/products-eurostat-news/-/DDN-20190108-1.

Fa, L., Mou, J., Fa, Y., Zhou, X., Zang, Y., Liang, M., Ding, P., Tang, S., Yang, H., Zhang, Q., Wang, M., Li, G., Zhao, M. (2018). On Transient Response of Piezoelectric Transducers. *Frontiers in Physics*, 6(123): 1-12.

Fine, H., Packer, M., Hoffman, R.S. (2002). New phacoemulsification technologies. *J Cataract Refract Surg*., 28: 1054-1060.

Graw, J. (2003). The genetic and molecular basis of congenital eye defects. *Nat Rev Genet*., 4(11): 876:888.

Gross, H., Blechinger, F. and Achtner, B. (2008). Handbook of Optical Systems. Vol 4. Ch.36. John Wiley & Sons, Ltd. Weinheim, Germany.

Haykin, S., Veen, B. V. (2002). *Signals and Systems*. Second edition. John Wiley & Sons. New York.

Hoskins, P., Martin, K., Thrush, A. (2010). *Diagnostics ultrasound: Physics and Equipment*. Second edition, Cambridge University Press, Cambridge.

Huang, C. C., Ameri, H., DeBoer, C., Rowley, A. P., Xu, X., Sun, L., Wang, S., Humayun, M. S., Shung, K. K. (2007). Evaluation of Lens Hardness in Cataract Surgery using High-Frequency Ultrasonic Parameters in Vitro. *Ultrasound Med. Biol*., 33(10): 1609–1616.

Huang, C. C., Zhou, Q., Ameri, H., Wu, D., Sun, L., Wang, S., Humayun, M. S., Shung, K. K. (2007). Determining the Acoustic Properties of the Lens Using a High-Frequency Ultrasonic Needle Transducer. *Ultrasound Med. Biol*., 33(12): 1971–1977.

Irsch, K., Guyton, D.L. (2009). Anatomy of Eyes. In: Li, S.Z., Jain, A. (eds) Encyclopedia of Biometrics. Springer, Boston, MA.

Krautkramer, J., Krautkramer, H. (2002). Ultrasonic Testing of Materials. Fourth edition. Springer Berlin, Heidelberg.

Lopes, M. (2020). *Development of a System for Cataract Evaluation Using Ultrasound Signals*. Dissertation submitted for the Degree of Master in Biomedical Engineering, Universidade Nova de Lisboa, Lisboa. 94 pp.

Martínez, M. B., Moyano, D. B., González-Lezcano, R.A. (2021). Phacoemulsification: Proposals for Improvement in Its Application. *Healthcare*, 9(11), 1603.

Michael, R., Barraquer, R.I., Willekens, B., van Marle, J. and Vrensen, G.F.J.M. (2008). Morphology of age-related cuneiform cortical cataracts: The case for mechanical stress. *Vision Res*., 48(4): 626-34.

Michael, R., Bron, A. J. (2011). The ageing lens and cataract: a model of normal and pathological ageing. *Phil. Trans. R. Soc. B*, 366, 1278-1292.

Narayana, P. A., Ophir, J. (1983). On the Frequency Dependence of Attenuation in Normal and Fatty Liver. *IEEE Transactions on Sonics and Ultrasonics*, 30(6): 379-383.

Oppenheim, A. V., Willsky, A. S. (1996). *Signals and Systems*. Second edition. Prentice-Hall. New Jersey.

Packer, M., Fishkind, W.J., Fine, H., Seibel, B.S., Hoffman, R.S. (2005). The physics of phaco: A review. J Cataract Refract Surg., 31: 424-431.

Petrella, L., Fernandes, P., Santos, M., Caixinha, M., Nunes, S., Pinto, C., Morgado, M., Santos, J., Perdigão, F., Gomes., M. (2020). Safety Assessment of an A-Scan Ultrasonic System for Ophthalmic Use. *J Ultrasound Med*, 9999: 1–8.

Petrella, L., Perdigão, F., Caixinha, M., Santos, M., Lopes, M., Gomes, M., Santos, J. (2021). A-scan ultrasound in ophthalmology: A simulation tool. *Medical Engineering & Physics*, 97: 18-24.

Pinto, C. (2019). *Desenvolvimento de Um Sistema de Classificação e Visualização de Cataratas em Humanos*. Dissertação para a obtenção do grau de Mestre em Engenharia Eletrotécnica e de Computadores, Universidade de Coimbra, Coimbra. 87 pp.

Queirós, L., Redondo, P., França, M. *et al*. (2021). Implementing ICHOM standard set for cataract surgery at IPO-Porto (Portugal): clinical outcomes, quality of life and costs. *BMC Ophthalmol*, 21 (119): 1-10.

Rocha, K. M. and Krueger, R. K. (2008). Ophthalmic biometry. *Ultrasound Clin*, 3(2): 195–200.

Riordan-Eva, P and Cunningham, E.T. (2011). *Vaughan and Asbury's General Ophthalmology*. 18th Edition. McGraw Hill. London.

Santos, J. B. (1994). *Controlo de Materiais por Ultrassons: A espetroscopia Ultrassonora na Caracterização e Classificação de Defeitos em Materiais*. Dissertação para a obtenção do grau de Doutor em Ciências da Engenharia, na Área de Engenharia Eletrotécnica, na Especialidade de Materiais e Campos Eletromagnéticos. Universidade de Coimbra, Coimbra. 174 pp.

Schirru, M. (2017). Development of an Ultrasonic Sensing Technique to Measure Lubricant Viscosity in Engine Journal Bearing In-Situ. Springer International Publishing. Gewerbestrasse.

Silverman, R.H. (2016). Focused ultrasound in ophthalmology. *Clinical Ophthalmology*, 10: 1865-1875.

Tole, N. M. (2005). *Basic Physics of Ultrasonographic Imaging*. World Health Organization, Geneva.

Treeby, B., Cox, B. and Jaros, J. (2016). *k-Wave - A MATLAB Toolbox for the Time Domain Simulation of Acoustic Wave Fields*. Assessed on: jun, 2022, available at: http://www.k-wave.org/manual/k-wave_user_manual_1.1.pdf.

Vrensen, G, e B Willekens. (1990). Biomicroscopy and scanning electron microscopy of early opacities in the aging human lens. *Investigative Ophthalmology & Visual Science*, 31(8): 1582-1591.

Wang, W., Yan, W., Fotis, K., Prasad, N. M., Lansingh, V. C., Taylor, H. R., Finger, R. P., Facciolo, D., He, M. (2016). Cataract surgical rate and socioeconomics: a global study. *Invest Ophthalmol Vis Sci*, 57(14): 5872-5881.

World Health Organization (WHO). (2019). World report on vision. Geneva. CC BY-NC-SA 3.0 IGO.

Zaki, W.M.D.W., Mutalib, H.A., Ramlan, L.A., Hussain, A., Mustapha, A. (2022). Towards a Connected Mobile Cataract Screening System: A Future Approach. *J. Imaging*, 8(2), 41: 1-19.

Zhou, Q., Lam, K.H., Zheng, H., Qiu, W., Shung, K.K. (2014). Piezoelectric single crystal ultrasonic transducers for biomedical applications. *Progress in Materials Science*, 66: 87-111.

Appendix A – Datasheet of the 20 MHz A-scan Probe

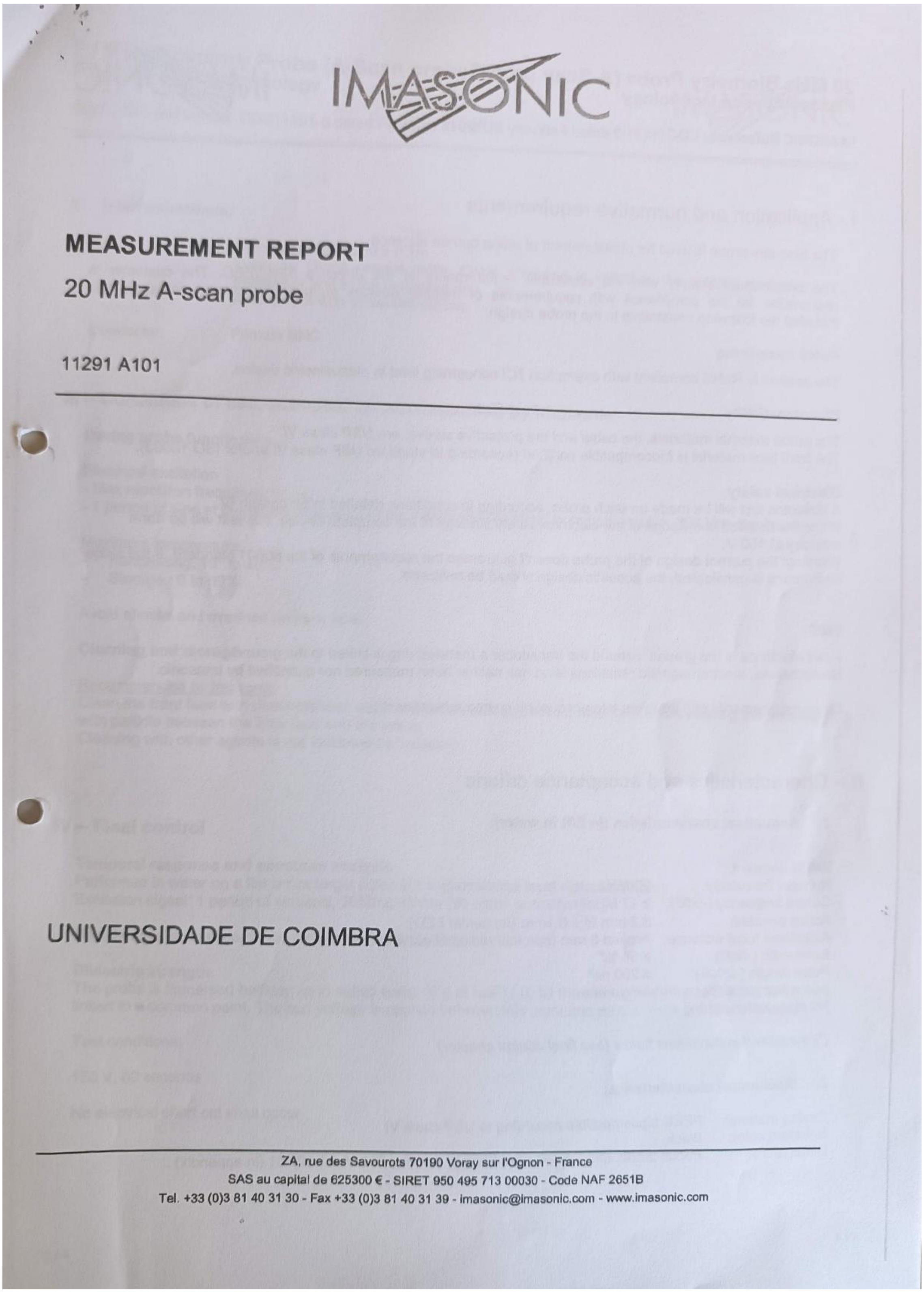

IMASONIC

MEASUREMENT REPORT

20 MHz A-scan probe

11291 A101

UNIVERSIDADE DE COIMBRA

ZA, rue des Savourots 70190 Voray sur l'Ognon - France
SAS au capital de 625300 € - SIRET 950 495 713 00030 - Code NAF 2651B
Tel. +33 (0)3 81 40 31 30 - Fax +33 (0)3 81 40 31 39 - imasonic@imasonic.com - www.imasonic.com

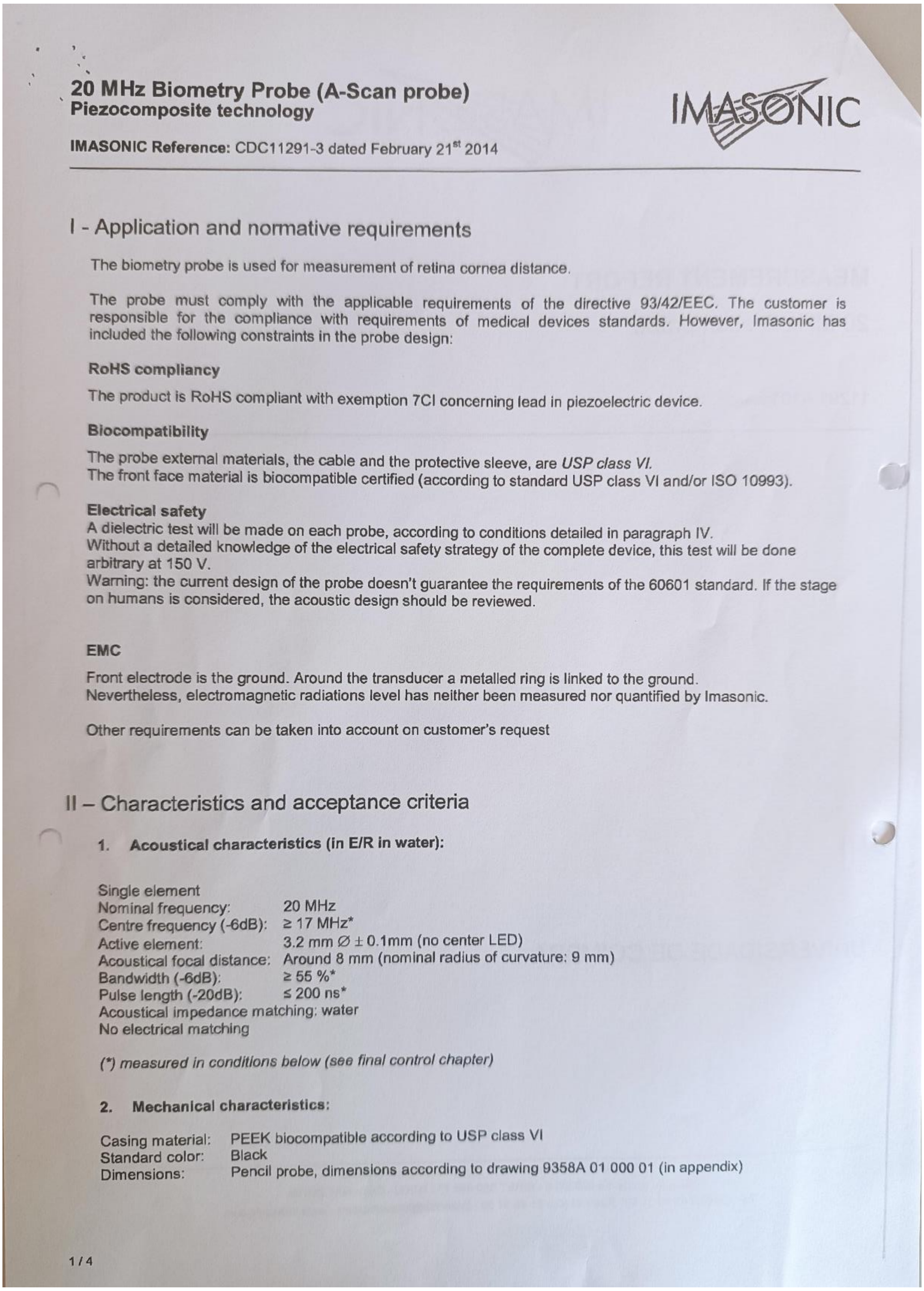

20 MHz Biometry Probe (A-Scan probe)
Piezocomposite technology

IMASONIC Reference: CDC11291-3 dated February 21st 2014

I - Application and normative requirements

The biometry probe is used for measurement of retina cornea distance.

The probe must comply with the applicable requirements of the directive 93/42/EEC. The customer is responsible for the compliance with requirements of medical devices standards. However, Imasonic has included the following constraints in the probe design:

RoHS compliancy

The product is RoHS compliant with exemption 7CI concerning lead in piezoelectric device.

Biocompatibility

The probe external materials, the cable and the protective sleeve, are *USP class VI.*
The front face material is biocompatible certified (according to standard USP class VI and/or ISO 10993).

Electrical safety
A dielectric test will be made on each probe, according to conditions detailed in paragraph IV.
Without a detailed knowledge of the electrical safety strategy of the complete device, this test will be done arbitrary at 150 V.
Warning: the current design of the probe doesn't guarantee the requirements of the 60601 standard. If the stage on humans is considered, the acoustic design should be reviewed.

EMC

Front electrode is the ground. Around the transducer a metalled ring is linked to the ground.
Nevertheless, electromagnetic radiations level has neither been measured nor quantified by Imasonic.

Other requirements can be taken into account on customer's request

II – Characteristics and acceptance criteria

1. Acoustical characteristics (in E/R in water):

Single element
Nominal frequency: 20 MHz
Centre frequency (-6dB): ≥ 17 MHz*
Active element: 3.2 mm Ø ± 0.1mm (no center LED)
Acoustical focal distance: Around 8 mm (nominal radius of curvature: 9 mm)
Bandwidth (-6dB): ≥ 55 %*
Pulse length (-20dB): ≤ 200 ns*
Acoustical impedance matching: water
No electrical matching

(*) measured in conditions below (see final control chapter)

2. Mechanical characteristics:

Casing material: PEEK biocompatible according to USP class VI
Standard color: Black
Dimensions: Pencil probe, dimensions according to drawing 9358A 01 000 01 (in appendix)

1 / 4

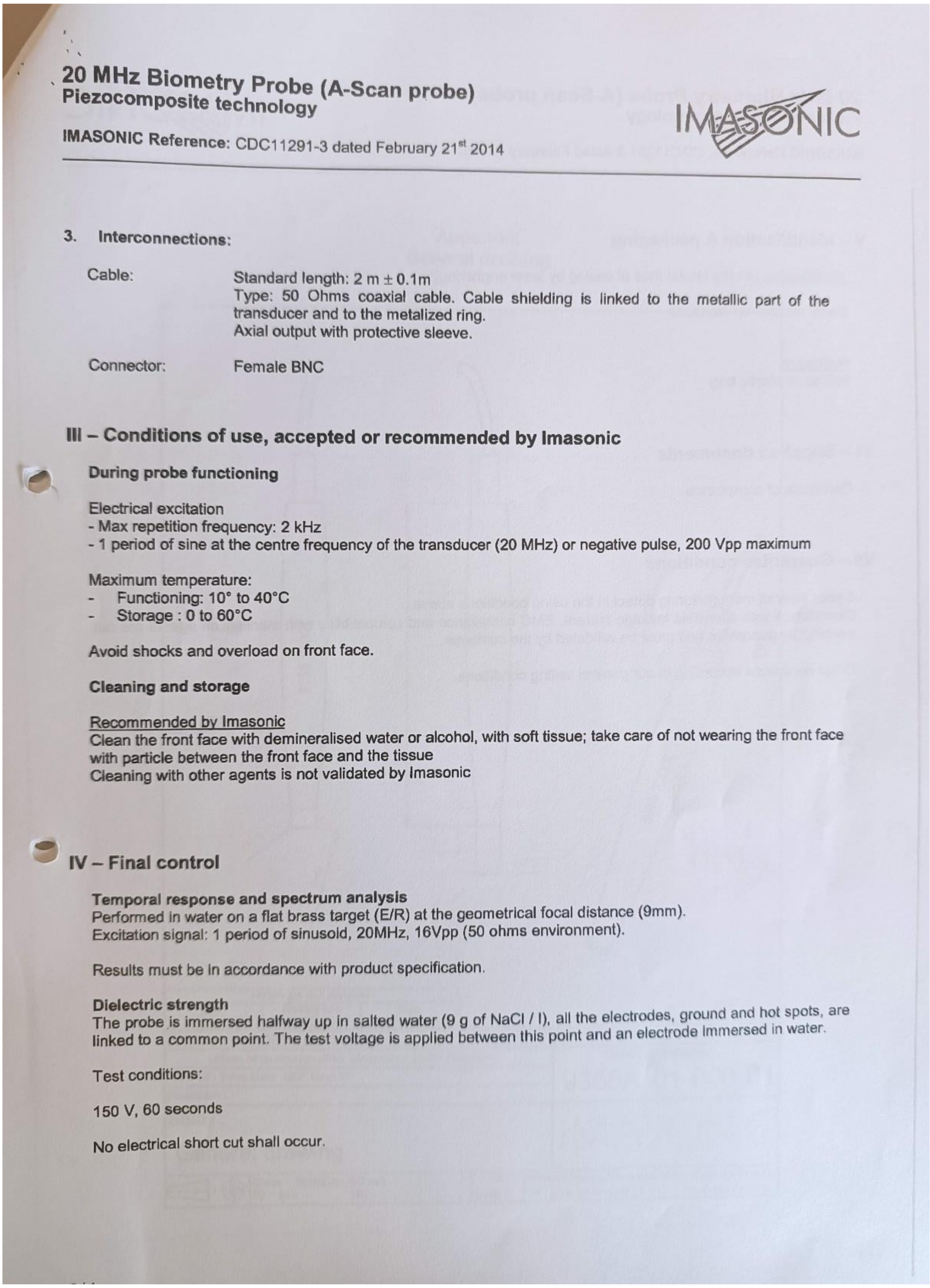

20 MHz Biometry Probe (A-Scan probe)
Piezocomposite technology

IMASONIC Reference: CDC11291-3 dated February 21st 2014

IMASONIC

---

3. Interconnections:

Cable:	Standard length: 2 m ± 0.1m Type: 50 Ohms coaxial cable. Cable shielding is linked to the metallic part of the transducer and to the metalized ring. Axial output with protective sleeve.
Connector:	Female BNC

III – Conditions of use, accepted or recommended by Imasonic

During probe functioning

Electrical excitation
- Max repetition frequency: 2 kHz
- 1 period of sine at the centre frequency of the transducer (20 MHz) or negative pulse, 200 Vpp maximum

Maximum temperature:
- Functioning: 10° to 40°C
- Storage : 0 to 60°C

Avoid shocks and overload on front face.

Cleaning and storage

Recommended by Imasonic
Clean the front face with demineralised water or alcohol, with soft tissue; take care of not wearing the front face with particle between the front face and the tissue
Cleaning with other agents is not validated by Imasonic

IV – Final control

Temporal response and spectrum analysis
Performed in water on a flat brass target (E/R) at the geometrical focal distance (9mm).
Excitation signal: 1 period of sinusoid, 20MHz, 16Vpp (50 ohms environment).

Results must be in accordance with product specification.

Dielectric strength
The probe is immersed halfway up in salted water (9 g of NaCl / l), all the electrodes, ground and hot spots, are linked to a common point. The test voltage is applied between this point and an electrode immersed in water.

Test conditions:

150 V, 60 seconds

No electrical short cut shall occur.

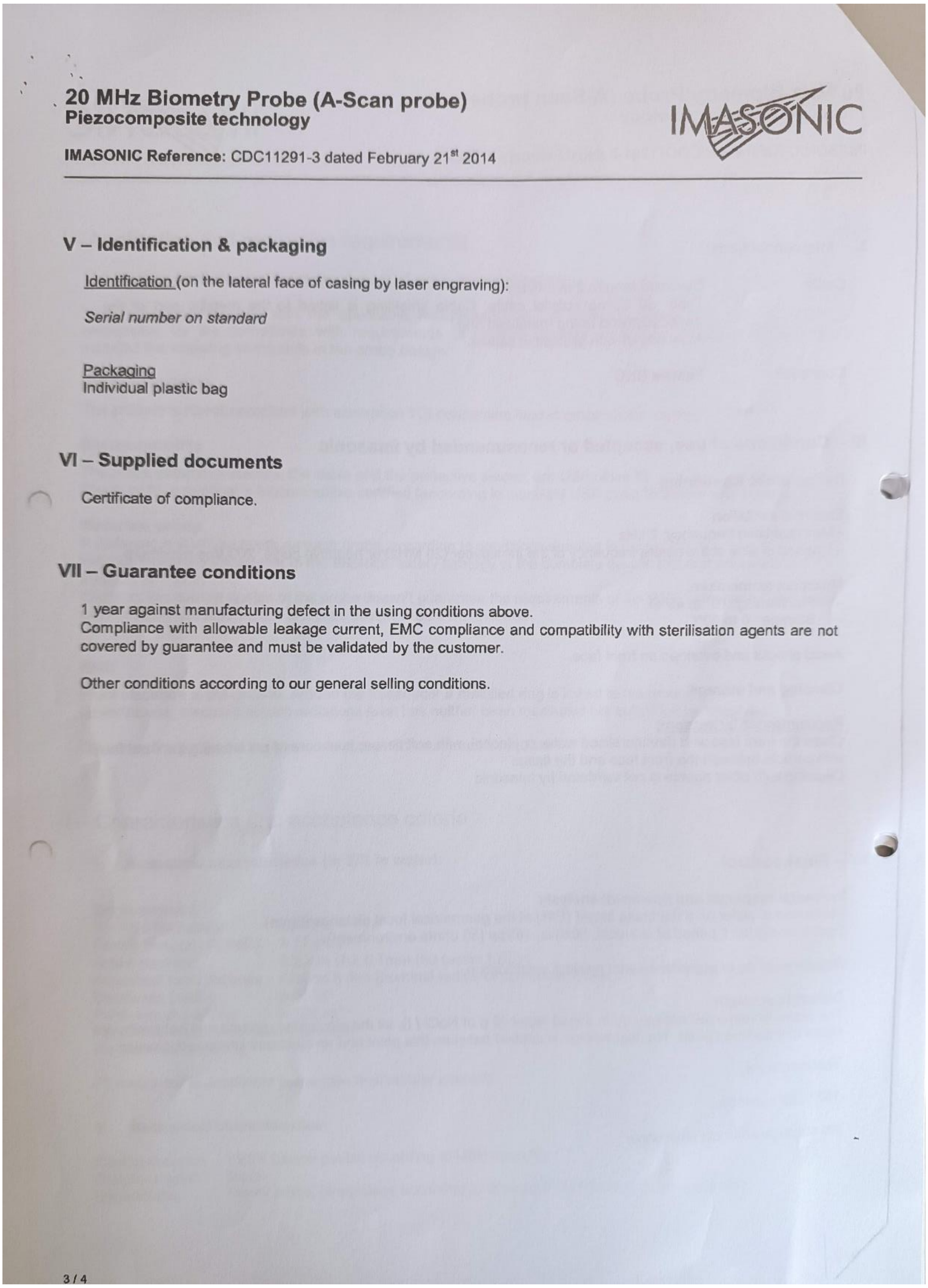

20 MHz Biometry Probe (A-Scan probe)
Piezocomposite technology

IMASONIC Reference: CDC11291-3 dated February 21st 2014

V – Identification & packaging

Identification (on the lateral face of casing by laser engraving):

Serial number on standard

Packaging
Individual plastic bag

VI – Supplied documents

Certificate of compliance.

VII – Guarantee conditions

1 year against manufacturing defect in the using conditions above.
Compliance with allowable leakage current, EMC compliance and compatibility with sterilisation agents are not covered by guarantee and must be validated by the customer.

Other conditions according to our general selling conditions.

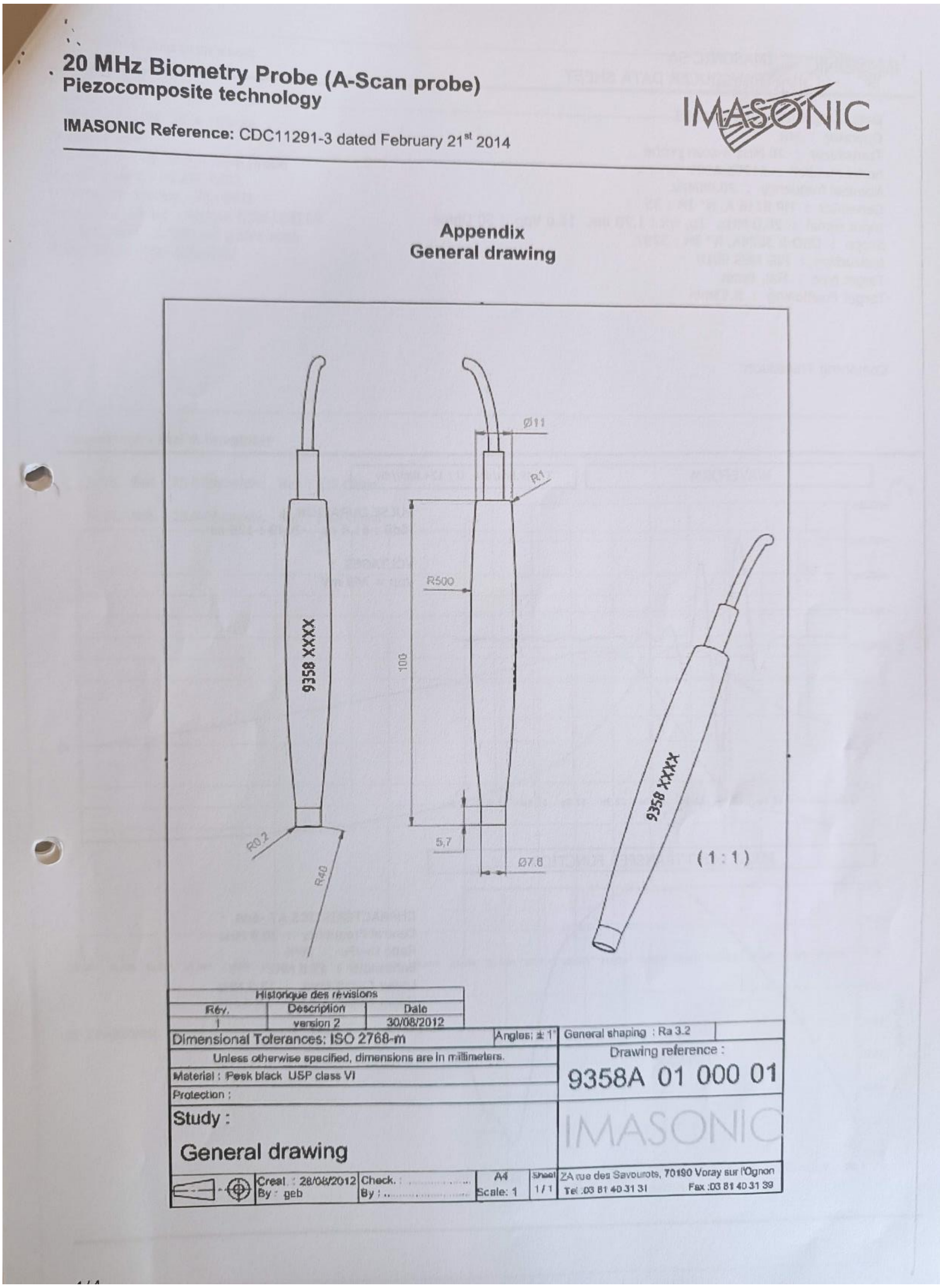

20 MHz Biometry Probe (A-Scan probe)
Piezocomposite technology

IMASONIC Reference: CDC11291-3 dated February 21st 2014

Appendix
General drawing

Historique des révisions		
Rév.	Description	Date
1	version 2	30/08/2012

Dimensional Tolerances: ISO 2768-m
Angles: ± 1°
General shaping : Ra 3.2
Unless otherwise specified, dimensions are in millimeters.
Material : Peek black USP class VI
Protection :
Drawing reference :
9358A 01 000 01
Study :
General drawing
IMASONIC
Creat. : 28/08/2012
By : geb
Check. : ....
By : ....
A4
Scale: 1
Sheet 1 / 1
ZA rue des Savourots, 70190 Voray sur l'Ognon
Tel :03 81 40 31 31
Fax :03 81 40 31 39

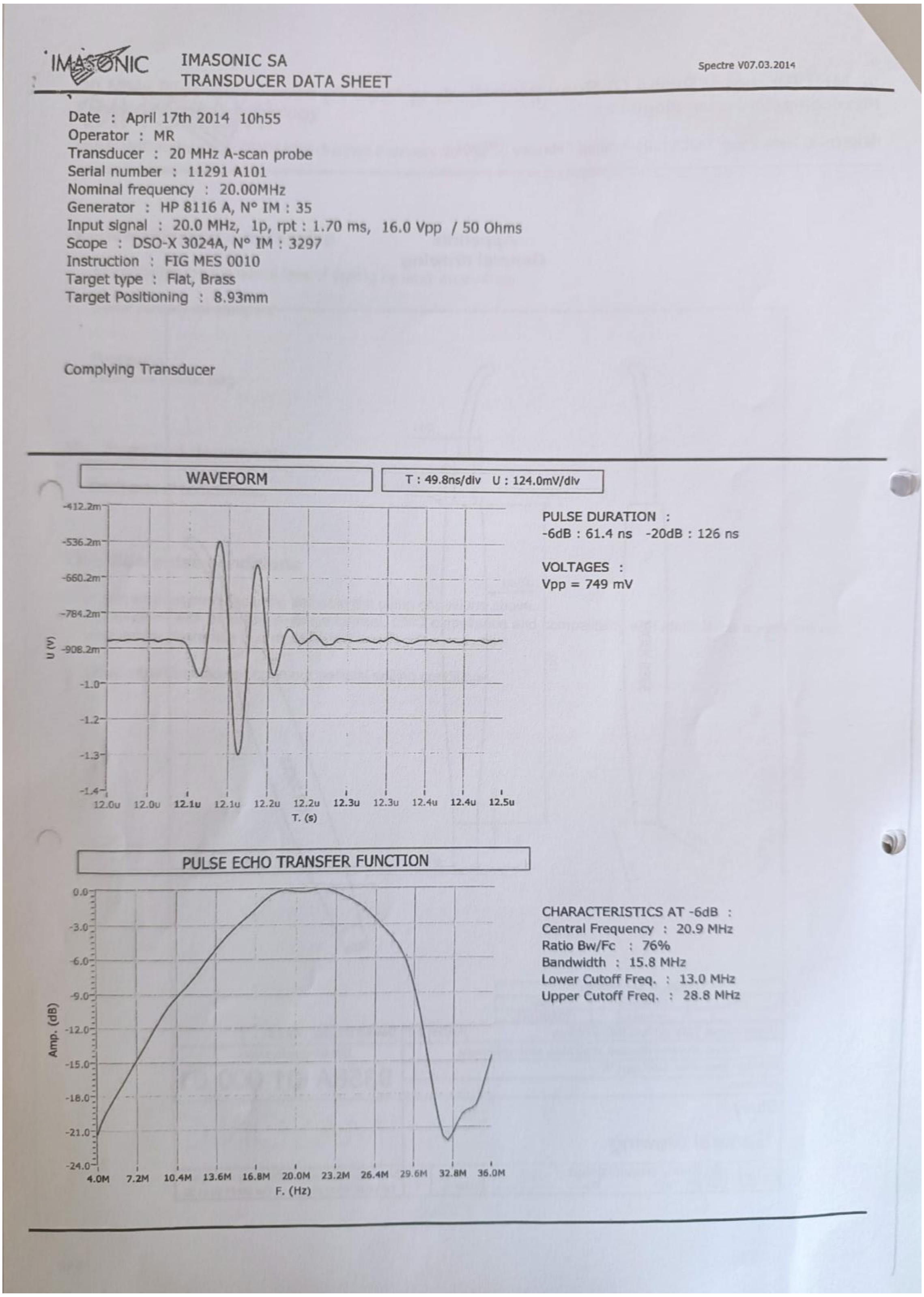

IMASONIC SA
TRANSDUCER DATA SHEET

Spectre V07.03.2014

Date : April 17th 2014 10h55
Operator : MR
Transducer : 20 MHz A-scan probe
Serial number : 11291 A101
Nominal frequency : 20.00MHz
Generator : HP 8116 A, N° IM : 35
Input signal : 20.0 MHz, 1p, rpt : 1.70 ms, 16.0 Vpp / 50 Ohms
Scope : DSO-X 3024A, N° IM : 3297
Instruction : FIG MES 0010
Target type : Flat, Brass
Target Positioning : 8.93mm

Complying Transducer

T : 49.8ns/div U : 124.0mV/div

PULSE DURATION :
-6dB : 61.4 ns -20dB : 126 ns

VOLTAGES :
Vpp = 749 mV

CHARACTERISTICS AT -6dB :
Central Frequency : 20.9 MHz
Ratio Bw/Fc : 76%
Bandwidth : 15.8 MHz
Lower Cutoff Freq. : 13.0 MHz
Upper Cutoff Freq. : 28.8 MHz

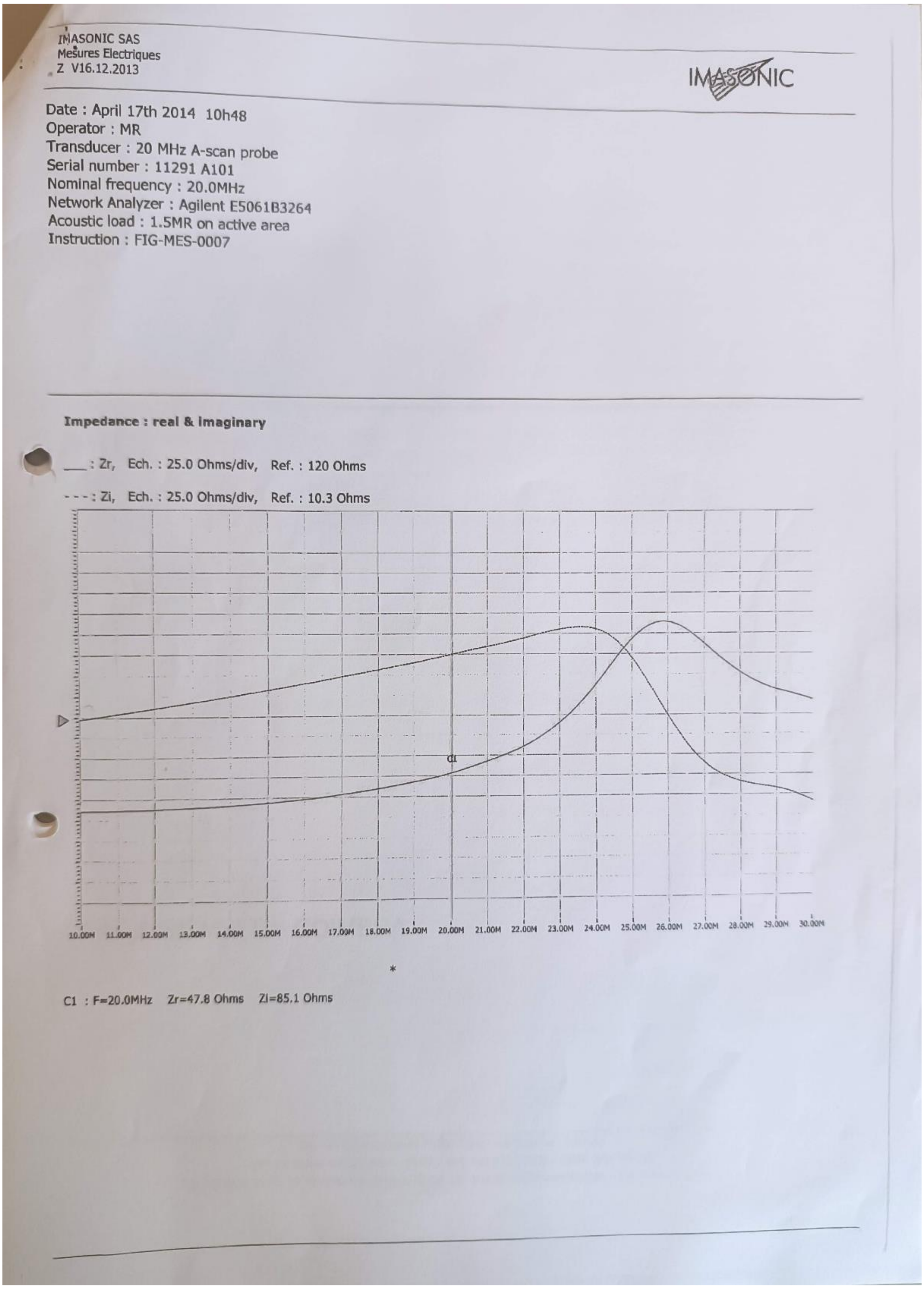

IMASONIC SAS
Mesures Electriques
Z V16.12.2013

Date : April 17th 2014 10h48
Operator : MR
Transducer : 20 MHz A-scan probe
Serial number : 11291 A101
Nominal frequency : 20.0MHz
Network Analyzer : Agilent E5061B3264
Acoustic load : 1.5MR on active area
Instruction : FIG-MES-0007

Impedance : real & imaginary

___ : Zr, Ech. : 25.0 Ohms/div, Ref. : 120 Ohms

- - - : Zi, Ech. : 25.0 Ohms/div, Ref. : 10.3 Ohms

C1 : F=20.0MHz Zr=47.8 Ohms Zi=85.1 Ohms